

Zhiguo Deng

GPS Meteorology with Single Frequency Receivers

Scientific Technical Report STR12/09

Imprint

HELMHOLTZ CENTRE POTSDAM
**GFZ GERMAN RESEARCH CENTRE
FOR GEOSCIENCES**

Telegrafenberg
D-14473 Potsdam

Printed in Potsdam, Germany
June 2012

ISSN 1610-0956

DOI: 10.2312/GFZ.b103-12099
URN: urn:nbn:de:kobv:b103-12099

This work is published in the GFZ series
Scientific Technical Report (STR)
and electronically available at GFZ website
www.gfz-potsdam.de > News > GFZ Publications

Zhiguo Deng

GPS Meteorology with Single Frequency Receivers

Referent: Prof. Dr.-Ing. Steffen Schön

Korreferenten: Prof. Dr. phil. nat. Markus Rothacher (ETH Zürich)
Prof. Dr.-Ing. Uwe Sörgel

Gutachter: Dr. Jens Wickert (GFZ)

Tag der mündlichen Prüfung: 6.3.2012

Hannover 2012

Scientific Technical Report STR12/09

Referent: Prof. Dr.-Ing. Steffen Schön
Korreferenten: Prof. Dr. phil. nat. Markus Rothacher (ETH
Zürich)
Prof. Dr.-Ing. Uwe Sörgel
Gutachter: Dr. Jens Wickert (GFZ)

Tag der mündlichen Prüfung: 6.3.2012

Abstract

Atmospheric water vapor plays a significant role in atmospheric convection and in the development of clouds and precipitation. As one of the key parameters for modern weather prediction, the atmospheric water vapor has high temporal and spatial variability. The lack of observations of the atmospheric water vapors in space and time limits the accuracy of short-term weather forecasts. Therefore, the spatial and temporal resolution of the atmospheric water vapor observations needs to be improved. Using the Global Positioning System (GPS) in meteorology provides a unique opportunity for this need. Radio signals emitted by the GPS satellites are bent and delayed depending on the temperature, pressure and water vapor. Based on the tropospheric delay, the water vapor distribution within the troposphere can be determined. However, to detect the water vapor distribution with a resolution of kilometer scale in horizontal and sub-kilometer scale in vertical direction, the existing GPS networks must be densified. Due to economic reasons, this densification is recommended with single frequency (SF) receivers. For normal dual-frequency (DF) GPS receivers the observations of the second frequency L2 can be used to eliminate the ionospheric delay by forming a linear combination with the observations of the first frequency L1. In the SF data processing a different ionospheric delay handling is required.

In this thesis it is shown that the epoch-differenced ionospheric delay correction is sufficient for estimating the tropospheric delay, e.g., the Zenith Total Delay (ZTD), from SF GPS data. Based on this result, the Satellite-specific Epoch-differenced Ionospheric Delay model (SEID) was developed. In the SEID model the ionospheric corrections for SF data are generated from the observations of surrounding reference stations equipped with DF receivers. With the derived ionospheric corrections and the SF data, pseudo L2 data are generated, which can be processed using existing GPS processing software packages without any changes.

In order to evaluate the performance of the SEID model, 24 simulated densification scenarios with different reference station densities and varying numbers of reference stations were defined and investigated. The validations showed very promising results: for densification scenarios with mean distances of the SF station to reference stations below 80 km, the ZTD accuracy of the SF receivers is comparable with those of the DF receivers. The study shows that the ZTD reliability of the SF data is improved with decreased reference station distance and increased number of reference stations.

The approach is validated with data from a very dense GPS network with mixed SF and DF receivers in Germany. The ZTDs derived from the SF and DF data were compared. Their differences in Root Mean Square (RMS) are about 3 mm which is negligible compared to the differences due to processing with various state-of-the-art software packages of about 7 mm.

To assess the possibility of densifying an existing GPS network with low-cost SF GPS receivers, an evaluation study was carried out. Observations from 258 German DF GPS stations are treated as observations from SF GPS stations, i.e., only L1 GPS observations are used. ZTD, Slant Total Delay (STD) and Slant Water Vapor (SWV) products, derived from the SF data using the SEID model, are validated using tropospheric products derived from DF data, a Water Vapor Radiometer (WVR) and European Centre for Medium-Range Weather Forecasts (ECMWF) analyses. The three

validation studies show that the ZTD, STD and SWV products obtained from SF data are almost of the same high-quality as those from the DF data. Compared to the tropospheric products from the DF data the ZTD from the SF data have an accuracy of 3 mm in RMS, and the relative accuracy of SF STDs is almost constant for all elevation angles and equals $\sim 0.18\%$, which is not degrading with decreasing elevation angles. The SWV between GPS and WVR agree equally well; the standard deviation increases almost linearly from $1.3 \text{ kg}\cdot\text{m}^{-2}$ near the zenith to about $2 \text{ kg}\cdot\text{m}^{-2}$ at 20° elevation. The quality of the tropospheric products derived from SF data is fully adequate for atmosphere sounding. The easy implementation and the accuracy of the SEID model can speed up the densification of existing networks with SF receivers.

Keywords: *Global Positioning System, GPS meteorology, ionospheric delay model, low-cost single frequency receiver*

Zusammenfassung

Der atmosphärische Wasserdampf spielt eine bedeutende Rolle für das Wettergeschehen und speziell für die Entwicklung von Wolken und Niederschlag. Als einer der wichtigsten Parameter für die moderne Wettervorhersage hat der atmosphärische Wasserdampf hohe zeitliche und räumliche Variabilität und Beobachtungen mit entsprechend hoher Auflösung sind erforderlich, um kurzfristige Wetterprognosen mit ausreichender Genauigkeit zu erstellen. Eine Möglichkeit derartige Beobachtungen bereitzustellen besteht in der Nutzung von Daten des Global Positioning Systems (GPS). Die GPS-Signale werden auf ihrem Weg vom GPS-Satelliten zum Empfänger auf Erde durch die Atmosphäre verändert. Dieser atmosphärische Einfluss muss bei der Positionierung berücksichtigt werden, kann jedoch auch zur Atmosphärensondierung genutzt werden. Die troposphärische Laufzeitverzögerung liefert speziell Informationen zum Wasserdampfgehalt der unteren Atmosphäre. Aus einer hinreichend großen Zahl von GPS-Beobachtungen kann prinzipiell die räumliche Verteilung des Wasserdampfes bestimmt werden. Um jedoch Feuchtefelder mit horizontalen Auflösungen von einigen Kilometern bestimmen zu können, ist eine Verdichtung der bestehenden GPS-Netze notwendig. Aus Kostengründen empfiehlt es sich, die bestehenden geodätischen Netze mit Einfrequenz-Empfängern (SF) zu verdichten. Die notwendigen Ionosphären-Korrekturen können mit Hilfe der L2-Daten der umliegenden Zweifrequenz-Empfänger (DF) durchgeführt werden.

Ein Ziel dieser Arbeit ist es, zu zeigen, dass die Daten von SF-Empfängern, die von einem Netz aus DF-Empfängern umgeben sind, mit sehr großer Genauigkeit prozessiert werden können. Hierzu wurde das SEID (Satelliten-spezifische Epochen-Differenz) Verfahren entwickelt, das die zeitlichen Differenzen in den ionosphärischen Verzögerungen der umgebenden DF-Empfänger nutzt, um ein synthetisches L2-Signal für die SF-Empfänger zu generieren. Zusammen mit den beobachteten L1-Daten stehen damit formal für jeden SF-Empfänger dieselben Informationen zur Verfügung, wie sie DF-Empfänger liefern. Diese Datensätze können genauso wie DF-Daten von bestehender GPS-Auswertesoftware verarbeitet werden. Dieses Verfahren kann z.B. die troposphärischen Laufzeitverzögerungen in Zenit Richtung (ZTD – Zenith Total Delay) mit hoher Genauigkeit bestimmen werden.

Um die Genauigkeit des SEID-Modells abzuschätzen, wurden verschiedene Studien durchgeführt. Prinzipiell nimmt die Genauigkeit ab, je weniger Referenzstationen in der Nähe des SF-Empfängers liegen und je weiter diese entfernt sind. Deshalb wurden Szenarien mit einer unterschiedlichen Anzahl von Referenzstationen in unterschiedlichen Entfernungen analysiert. Die Ergebnisse fallen sehr positiv aus: für Szenarien bei denen die mittleren Entfernungen zwischen den SF-Stationen und den Referenzstationen unter etwa 80 km liegen, ist die Genauigkeit der ZTD Beobachtungen vergleichbar mit DF-Beobachtungen. Diese Studie zeigt auch, dass die ZTD Genauigkeit der SF-Daten besser wird, je geringer die Distanz zu den Referenzstationen ist und je mehr Referenzstationen verfügbar sind.

Darüber hinaus wurden die ebenfalls geschätzten Slant Total Delays (STDs) mit den Beobachtungen eines Wasserdampf-Radiometers (WVR) und den Analysen eines numerischen Wettermodells (ECMWF) verglichen. Das Wettermodell stellt alle Informationen bereit, um die STDs für die etwa 260 verfügbaren deutschen Stationen zu

berechnen. Diese STDs wurden sowohl mit den hochgenauen DF-Produkten als auch mit den SF-Produkten, die mit Hilfe der SEID-Methode abgeleitet wurden, verglichen. Es zeigt sich, dass die relative Genauigkeit der SF STDs für alle Elevationswinkel nahezu konstant ist und einer Standardabweichung von etwa 0,18% entspricht.

Wasserdampf-Radiometer können den integrierten Wasserdampf entlang beliebiger Sichtachsen bestimmen (SWV – Slant Water Vapour). Um diesen mit den STDs aus der GPS-Prozessierung vergleichen zu können, muss der hydrostatische Anteil des STDs abgespalten und der sich daraus ergebende Slant Wet Delay (SWD) in den SWV umgerechnet werden. Entsprechende SWV-Vergleiche wurden für eine GPS-Station, die mit einem WVR ausgestattet ist, durchgeführt. Ähnlich wie beim ECMWF-Vergleich nimmt die Standardabweichung mit abnehmender Elevation zu: Sie steigt fast linear von $1,3 \text{ kg}\cdot\text{m}^{-2}$ nahe dem Zenit bis auf etwa $2 \text{ kg}\cdot\text{m}^{-2}$ bei einer Elevation von 20° .

Alle drei Validierungsstudien zeigen, dass die ZTD, STD und SIWV Produkte, die aus SF-Daten gewonnen wurden, nahezu die gleiche hohe Qualität haben wie die entsprechenden DF-Produkte. SF-Empfänger können damit uneingeschränkt zur Atmosphärensondierung eingesetzt werden. Die einfache Implementierung und hohe Genauigkeit des SEID-Modells legt die Verdichtung bestehender geodätischer Netze mit preiswerten SF-Empfängern nahe und kann zu einer verstärkten Nutzung der GPS-Atmosphärensondierung beitragen.

Schlagwörter: *Global Positioning System, GPS Meteorologie, ionosphärische Verzögerung Model, low-cost Ein-Frequenz GPS Empfänger*

Contents

1	Introduction.....	1
2	GPS meteorology.....	6
2.1	Introduction to GPS	6
2.2	GPS observation equations	10
2.2.1	Linear combinations of observations	10
2.2.2	Differencing of observations.....	12
2.3	Precise Point Positioning (PPP).....	13
2.4	Overview on EPOS software	15
2.4.1	Data pre-processing	17
2.4.2	Near-real-time orbit and clock products	18
2.4.3	Tropospheric product generation	20
2.5	Description of the IGS data used	22
2.6	Introduction to GPS meteorology and summary of recent results.....	24
2.6.1	Ground-based GPS meteorology	24
2.6.2	Space-based GPS radio occultation	28
2.7	The SAPOS network and densification with single frequency GPS receivers	29
3	Single frequency GPS receivers selection	31
3.1	Overview on single frequency GPS receivers and hardware selection	31
3.1.1	Single frequency GPS receivers	31
3.1.2	NovAtel (SMART-V1 antenna)	32
4	Precise processing of GPS single frequency data.....	39
4.1	Correction of ionospheric refraction for single frequency positioning.....	39
4.2	The SEID algorithm.....	44
4.2.1	Detailed description of the developed ionosphere correction method (SEID).....	46
4.2.2	Interpolation error study	52
4.2.3	Densification study	60
4.3	Observation of MSTID with dL_4	68
4.3.1	Estimating the parameters of MSTID.....	68
4.3.2	Comparison with TEC-DEIN	73

4.3.3	Interpolation error under MSTID.....	75
5	Single frequency GPS analysis results and validations.....	81
5.1	LUAMI single frequency analysis results.....	81
5.1.1	LUAMI and the related GPS network.....	81
5.1.2	Coordinate results from single frequency data.....	86
5.1.3	ZTD and IWV results.....	87
5.1.4	GPS Tomography for LUAMI.....	90
5.1.5	Long-term stability of single frequency data.....	92
5.2	Densification of the German GPS network.....	96
5.2.1	Comparison of tropospheric products from assumed SF and real DF stations.....	97
5.2.2	Validation with the ECMWF model using ray-tracing.....	102
5.2.3	Slant integrated water vapor from GPS and water vapor radiometers.....	105
6	Conclusions and outlook.....	109
	References.....	111

List of Abbreviations

AC	Analysis Center
Adv	German State Surveying Agencies
AGNES	Automated GNSS Network for Switzerland
ARNS	Aeronautical Radio Navigation Services
BfS	Federal Office of Radiation Protection
BKG	Federal Agency for Cartography & Geodesy, Germany
C/A	Coarse/Acquisition code
C/N ₀	Carrier-to-Noise power ratio
CHAMP	CHAllenging Minisatellite Payload
CODE	Centre of Orbit Determination in Europe
COPS	Convective and Orographically-induced Precipitation Study
COSMO	German weather model
DF	Double Frequency
DLR	German Aerospace Center
DOY	Day Of Year
DWD	German Weather Service
ECEF	Earth-centered Earth Fixed
ECMWF	European Centre for Medium-Range Weather Forecasts
E-GVAP	EIG EUMETNET GNSS water Vapour Programme
EIG EUMETNET	Economic Interesting Grouping European Meteorological Services Network
EPN	EUREF Permanent Network
EPOS	Earth Parameter and Orbit System Software
EUREF	EUropean REference network
GASP	GPS Atmosphere Sounding Project
GFZ	Helmholtz-Zentrum Potsdam Deutsches GeoForschungsZentrum
GIS	Geographic Information System
GMF	Global Mapping Function
GNSS	Global Navigation Satellite System
GOP	Geodetic Observatory Pecny, Czech Republic
GPS	Global Positioning System
GPT	Global Pressure & Temperature model
GRACE	Gravity Recovery and Climate Experiment
GRAF	German GPS reference network
HATPRO	Hemisphere-scanning Humidity and Temperature Profiler
IES	Institute of Engineering, Surveying and Space Geodesy, Univ. of Nottingham, UK
IGE	Instituto Geografico National, Spain
IGR	IGS Rapid orbit
IGS	International GPS Service
IGS	IGS final orbit
IGU	IGS Ultra-rapid orbit
IPP	Ionospheric Pierce Point
IRE	Met Éireann, Rep. Ireland
ITRF	International Terrestrial Reference Frame
IWV	Integrated Water Vapor
JPL	Jet Propulsion Lab
KNMI	Royal Meteorological Inst. of the Netherlands
LEO	Low Earth Orbit
LIDAR	Light Detection And Ranging

LPT	SwissTopo
LUAMI	Lindenberg Upper-Air Method Inter-comparison
MET	Meteorology
METO	Metoffice UK
MSTID	Medium-Scale Traveling Ionospheric Disturbance
NASA	National Aeronautics and Space Administration
NAVSTAR	NAVigation Satellite Timing And Ranging
NGAA	Chalmers Technical University and Swedish Meteorological and Hydrological Inst
NRT	Near-Real-Time
NWP	Numerical Weather Prediction
ODL	Gamma dose rate (in Germany: Gamma-Ortsdosisleistung)
PCO	Phase Center Offset
PCV	Phase Center Variation
PPP	Precise Point Positioning
PRN	Pseudo-Random Noise
PWU	Phase Wind Up
RINEX	Receiver Independent Exchange Format
RMS	Root Mean Square
RO	Radio Occultation
ROB	Royal Observatory of Belgium
RTIGSA	Real-Time IGS Archive
RTK	Real-Time Kinematics
SAPOS	Satellite Positioning Service of the German State Survey
SDD	Slant Dry Delay
SEID	Satellite-specific Epoch-differenced Ionospheric Delay model
SF	Single Frequency
SGN	Institut Geographique National, France
SHD	Slant Hydrostatic Delay
SINEX	Solution (Software/technique) INdependent Exchange
SNR	Signal to Noise Ratio
SP3	IGS Standard Product 3
STD	Slant Total Delay
SWD	Slant Wet Delay
TEC	Total Electron Content
TECU	Total Electron Content Unit
TID	Traveling Ionospheric Disturbance
UPD	Un-calibrated Phase Delays
UPS	Uninterruptible Power Supply
UTC	Coordinated Universal Time
VRS	Virtual Reference Station
VTEC	Vertical Total Electron Content
WVR	Water Vapor Radiometer
ZHD	Zenith Hydrostatic Delay
ZTD	Zenith Total Delay
ZWD	Zenith Wet Delay

1 Introduction

Water vapor in the atmosphere

Surrounding our planet Earth the atmosphere is a layer of gases, which are retained by the Earth's gravity. The atmosphere has very important functions to protect life on the Earth by:

- absorbing ultraviolet solar radiation,
- warming the surface through heat retention, and
- reducing temperature extremes between day and night.

The atmosphere can be divided into four main layers. These layers are mainly determined by whether temperature increases or decrease with altitude. From highest to lowest, these layers are: thermosphere, mesosphere, stratosphere and troposphere (Figure 1.1).

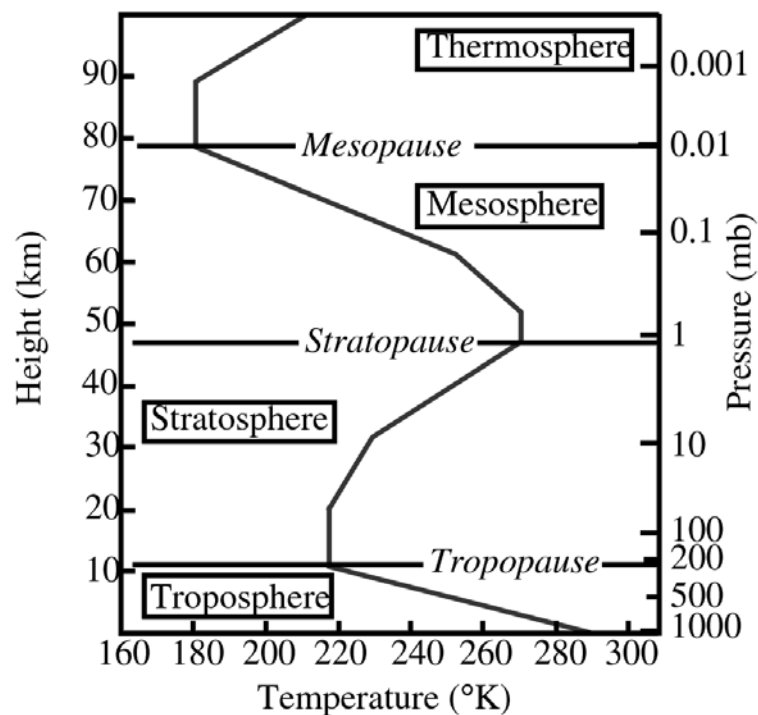


Figure 1.1: Layers of the atmosphere (<http://www.atmos.washington.edu> 2011).

Under typical atmospheric conditions, water vapor is continuously generated by evaporation and removed by condensation. Water vapor is lighter than air and triggers convection currents that can lead to clouds. As normal constituent of the atmosphere, water vapor resides mostly in the troposphere. In liquid or solid phase water is easily observed like clouds, fog, raindrops, snow etc; but in the gas phase water is invisible to the eye. About 50% water vapor is contained within the boundary layer, i.e., a layer up to about 1.5 km above sea level. Only less than 5-6% of the water vapor is above 5 km, and less than 1% is in the stratosphere (Seidel, 2002). As one of the major constituents of the atmosphere water vapor is most variable.

In atmospheric processes water vapor plays an important role and acts over a wide range of temporal and spatial scales, from global climate to micrometeorology, which impacts the global climate in two ways. In the Earth's hydrological cycle water vapor transfers energy in the atmosphere, forming and propagating weather (Hidore, 1972). In addition, it is the dominant greenhouse gas in the atmosphere (Cess, 2005). It allows the short wavelength radiation of the Sun to pass through the atmosphere, but traps the long wavelength radiation emitted by the Earth's surface. This trapped radiation causes the temperatures to increase.

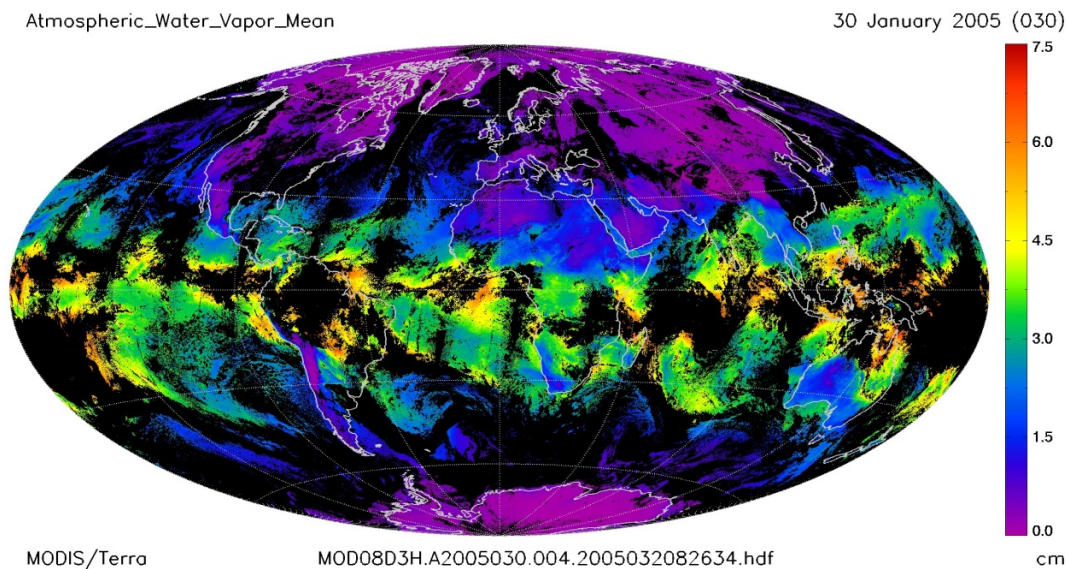


Figure 1.2: Global distribution of mean integrated water vapor on January 30, 2005 (<http://modis-atmos.gsfc.nasa.gov>).

The water vapor shows great spatial and temporal variability on local, regional, and global scale. **Figure 1.2** shows the global distribution of the water vapor. Since warm air can absorb more water vapor the amount of water vapor is larger in the equatorial than in polar areas.

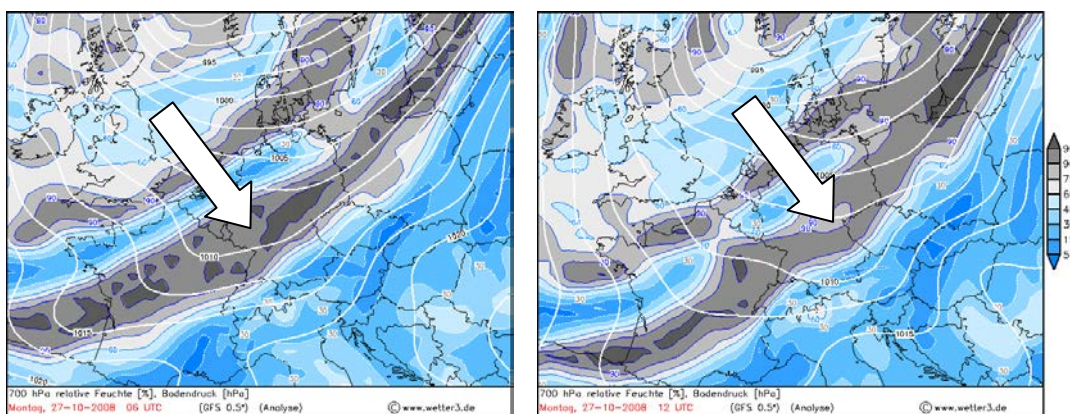


Figure 1.3: Distribution of relative humidity above Germany at 6 UTC and 12 UTC on 27 October 2008 (www.wetter3.de 2008).

In **Figure 1.3** a weather front moved over Europe southeastwards, and the water vapor changed within the 6 hours. The white arrows show the direction of the front movement; the humidity was highly variable in the atmosphere between 6 UTC and 12 UTC. The limitations in temporal and spatial humidity observation coverage often lead to

problems in numerical weather prediction, especially for short-term forecasts (Haase et al., 2003). The verification of humidity simulations in operational weather forecasts and climate modeling is also difficult because of the lack of data with high temporal and spatial resolution.

Observation techniques

To routinely measure the water vapor, atmospheric scientists employ three main techniques (Bevis et al., 1992):

- Radiosondes,
- Ground-based remote sensing,
- Space-based remote sensing.

Radiosondes are balloon-borne instruments, which can provide vertical profiles of water vapor, temperature and pressure up to an altitude of approximately 30 km. In many countries radiosonde networks have been set up as the most important part of upper air observing systems. But high costs of launching radiosondes limit the spatial and temporal resolution of the observations. Generally radiosondes are launched every 12 or 24 hours. Limitations of water vapor data from the radiosondes are major sources of errors in short-term forecasts of precipitation (Rocken et al., 1993).

Ground-based radiometry measures the background radiation emitted by atmospheric constituents. A water vapor radiometer (WVR) measures the intensity of the water vapor spectral line centered at 22,235 GHz, which can be converted into line-of-sight integrated water vapor (IWV). The WVR can provide high temporal resolution. However the WVR has also limitations. During heavy rainfall or observation close to the Sun the WVR cannot measure the sky brightness temperature. Furthermore it is also expensive. Hence only a few of these instruments are used today (Pacione et al., 2001).

Downward-looking WVRs are also found on board of satellites to measure microwave emissions from the atmosphere and the Earth's surface. The application of downward-looking WVRs is greatly affected by the complications of the background surface brightness temperature and the results are limited to cloud-free conditions (Bevis et al., 1992). Otherwise satellite-based radiometry provides good spatial but poor temporal resolution.

The space-based GPS radio occultation was developed in the last decade. The amount of bending in the path of radio signal transmitted from a GPS satellite to a Low-Earth-Orbit (LEO) satellite receiver is measured. The atmospheric parameters such as refractivity, temperature and pressure can be retrieved as a function of height. It has been shown that the GPS radio occultation measurements from the CHAMP experiment produce accurate profiles of atmospheric refractivity with high vertical resolution (Wickert et al., 2001). The GPS occultation technique has also disadvantages: firstly, because only the measurements from the GPS satellites near the plane of the LEO satellite orbit and near the horizon are used, they are not continuous; and the location of a disturbance along the propagation path is not known to better than ~200 km accuracy.

In the past several years there has been considerable international interest in measuring water vapor with ground-based GPS techniques. In 1992, Bevis et al. showed the possibility of using GPS to determine atmospheric water vapor. The signals emitted from GPS satellites propagate through the atmosphere, and experience a signal delay

due to the refractivity in the troposphere. The delay of the signals between a satellite and a ground receiver is dependent on the refractive index of the atmosphere. The delay can be used for water vapor estimation. This technique is known as GPS meteorology, which is currently an active research area. Compared to conventional water vapor observing systems the GPS/MET has several advantages (Gutman et al., 2004):

- High temporal resolution: IWV retrieved from GPS has a temporal resolution of 30 seconds to hours with all weather operability and is not affected by clouds.
- Low-cost equipment: at present a standard geodetic quality dual-frequency GPS receivers costs \$us 10k ~ 20k. As compared to WVR or radiosonde, the GPS receiver is more cost effective.
- Antenna of the GPS receiver is stabile, after it is calibrated once there is no necessity for external calibration for long periods. There is possibility of unattended operation with high reliability.

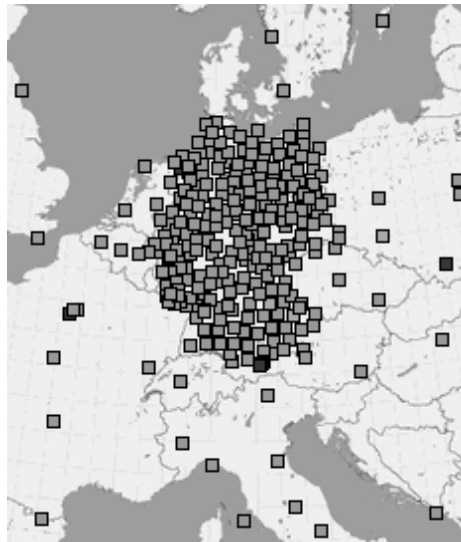


Figure 1.4: About 310 GPS stations operationally processed by GFZ (<http://egvap.dmi.dk>, March 16, 2011); for each hour about 1200 ZTD and IWV parameters are available.

Several European weather services improve their operational weather forecasts by assimilating near real-time Zenith Total Delay (ZTD) observations provided by different GNSS analysis centers. As one of the Analysis Centers of EGVAP¹ the Helmholtz-Zentrum Potsdam, Deutsches GeoForschungsZentrum (GFZ) is running an operational determination of the tropospheric ZTD and Slant Total Delays (STD) for the German network (**Figure 1.4**) in near real-time (~1 h delay) with a ZTD accuracy of 6 to 13 mm (Gendt et al., 2004).

However, recent studies show that for many meteorological applications, such as short-term numerical forecasting and the reconstruction of the spatio-temporal distribution of the tropospheric water vapor, GPS-derived tropospheric information of higher spatial and temporal resolution is required. Therefore, the existing regional GPS networks must be densified accordingly down to several kilometers of station separation in an ideal case (Bender et al., 2010; Braun et al., 1999; Yan et al., 2009). Due to economic reasons,

¹ Centers of Economic Interesting Grouping European Meteorological Services Network (EIG EUMETNET) GNSS water Vapour Programme

the densification should be realized with inexpensive single frequency (SF) GPS receivers.

In Germany the Federal Office of Radiation Protection (BfS) operates a nationwide gamma dose rate (ODL) monitoring network, which can directly monitor accidents leading to high radioactivity concentrations. The ODL network consists of about 1,800 stations which have been distributed over Germany in a raster of about 20×20 km (**Figure 1.5** left). Each station consists of a measuring probe mounted on a standpipe outside, preferably on a flat grass ground (**Figure 1.5** right) and a data logger with access to telephone mainline and a 230V power supply. The ODL network is an example for an existing large infrastructure, which potentially could be used for the densification of the existing GPS network in Germany. The low-cost GPS antenna could be installed on the top of an ODL probe with good visibility of the sky.

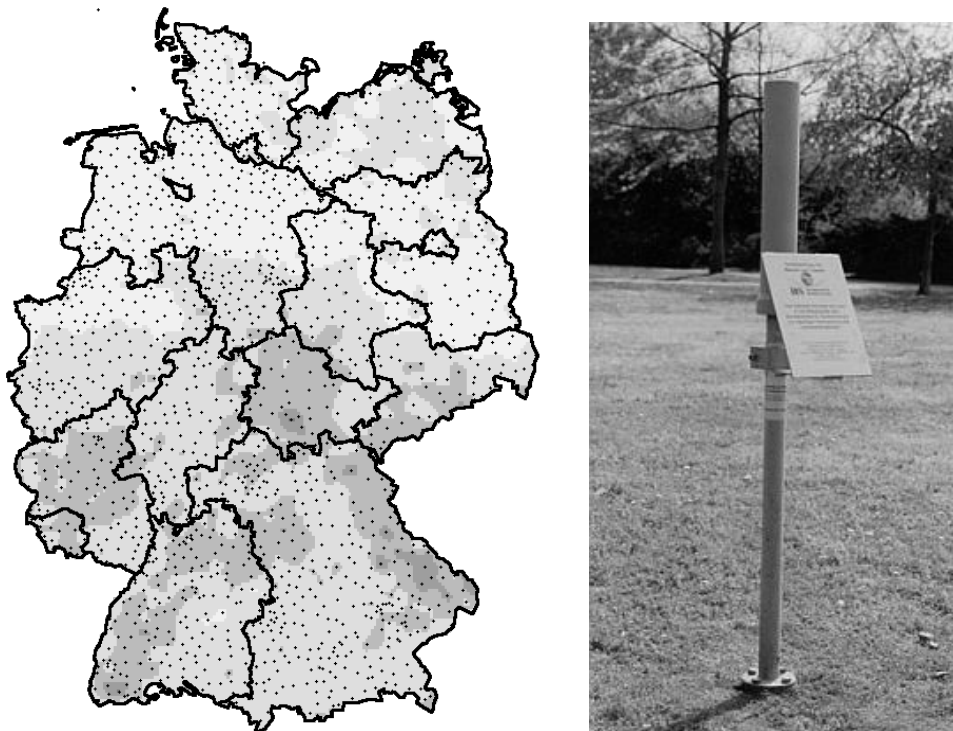


Figure 1.5: Left panel: BfS ODL monitoring network with more than 1800 stations; Right panel: probe of a monitoring station (www.bfs.de, 2011).

The primary objective of this thesis is to investigate and discuss the possibility and attainable accuracy of water vapor determination with SF receivers in GPS meteorology for the potential densification of regional GPS networks. To estimate ionospheric corrections for SF receivers embedded in networks of double frequency (DF) receivers the Satellite-specific Epoch-differenced Ionospheric Delay model (SEID) will be introduced and discussed. With such ionospheric corrections the SF GPS data can be processed in the same way as the DF data.

2 GPS meteorology

The concept of GPS meteorology was first published by Bevis et al. (1992), and has been rapidly accepted in meteorological sciences. GPS meteorology means using GPS data for the monitoring and analyses of water vapor in the atmosphere. The principle is that the atmospheric gases, including water vapor cause an additional delay (range error) in GPS observables as the signals travel through the neutral atmosphere. The additional delay can be modeled and estimated by a parameter called Zenith total delay (ZTD). Using the surface temperature and pressure at the GPS receiver site the ZTD can be transformed into IWV. For the precise positioning of a GPS station, the ZTD must be accurately estimated. The ZTD is an error term for positioning, while it is useful information for meteorology.

Over the past 20 years, the applications of GPS technologies have been developed in many different areas. GPS has become a mainstay of transportation systems worldwide, providing navigation for aviation, ground, and maritime operations. Disaster relief and emergency services depend upon GPS for location and timing capabilities in their life-saving missions. The accurate timing that GPS provides facilitates everyday activities such as banking, mobile phone operations, and even the control of power grids. Farmers, surveyors, geologists and countless others perform their work more efficiently, safely, economically, and accurately using the GPS. For scientific applications the GPS technologies are also widely used in many fields, such as geodesy, atmospheric research, seismology, geology, space sciences and oceanography, etc (Seeber, 2003).

2.1 Introduction to GPS

The NAVSTAR Global Positioning System (GPS) is a satellite-based navigation system. It provides services of positioning, navigation, and timing to worldwide users on a continuous basis in all weather, day and night, anywhere on or near the Earth. In 1973 the U.S. Department of Defense decided to establish, develop, test, acquire, and deploy the GPS. The primary goal of GPS is to provide land, air and marine positioning capabilities to the U.S. armed forces and its allies (Seeber, 2003). The GPS signal is freely available to all users, the number of civilian users is already far greater than the military users. Civilian applications include land surveying, vehicle guidance and control, as well as high-precision science, like GPS meteorology.

GPS system components

Usually, the description of the GPS follows the division into the space, ground and user segment (Seeber, 2003). The space segment consists of (more than) 24 satellites in orbit at an altitude of 20,200 km. Due to the unexpected long lifetime of the GPS satellites, recently 31 satellites were available (Aug. 2011). The orbital configuration is designed in such a way that at every point of the Earth's surface and at every time at least 4 satellites are above the radio horizon. The GPS satellites operate in circular orbits, with about a 12-hour period. They are distributed in 6 orbital planes. The ascending nodes of the orbital planes are separated by 60 degrees and the inclination of the planes is 55

degrees (see **Figure 2.1**).

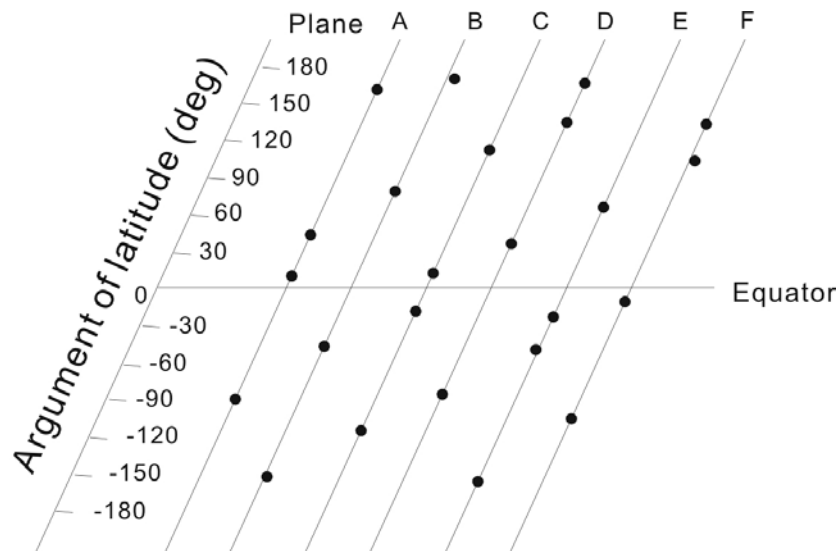


Figure 2.1: GPS satellite constellation (Seeber, 2003).

The control segment consists of the Master Control Station and five monitor stations, which control the satellites for orbit adjustment and provide the broadcast ephemerides. The user segment consists of GPS antennas and receivers that provide positioning, velocity, and precise timing to the user. Since the GPS is a passive system and there is no interaction from the user segment to the other segments, the number of users of the system can be arbitrarily high.

GPS signal

The GPS satellites transmit signals at two L-band frequencies with carrier wave frequencies of $L1 = 1575.42$ MHz and $L2 = 1227.60$ MHz. Onto these two carrier frequencies the navigation signals and system messages are modulated. The navigation signal is coded as a so-called pseudo random noise (PRN) sequence. To simultaneously observe many GPS satellites at the same time the PRN codes are unique for each satellite and the correlation between any pair of codes is very low. The PRN codes make it possible that all satellites share the same carrier frequency (Seeber, 2003).

In 1996, a GPS modernization was planned and since then it has been advanced. According to this plan, a new civil signal was added to the GPS L2 frequency. Instead of replicating the C/A-code, a truly modernized L2 civil (L2C) signal was designed. L2C is tasked with improving accuracy of navigation, providing an easy to track signal, and acting as a redundant signal in case of localized interference. Also, to satisfy the needs of aviation, the third civil frequency, known as L5, is centered at 1176.45 MHz, in the Aeronautical Radio Navigation Services (ARNS) band. Two PRN ranging codes are transmitted on L5: the in-phase code (denoted as the I5-code); and the quadrature-phase code (denoted as the Q5-code). Both codes are 10,230 bits long and transmitted at 10.23 MHz (1ms repetition). The new L5 is available on GPS Block IIF satellites, and does not cause any interference to existing systems. Therefore, without any modification of existing systems, the L5 will make GPS more robust for many aviation applications, as well as assist all ground-based users (Braschak et al., 2010).

GPS observables

In most cases two basic observations are used with the GPS system: pseudoranges from code measurements and carrier phases. The pseudoranges (C/A, L2C, P1, and P2) are measures of the travel time between the satellite and receiver. The GPS receiver generates a copy of the pseudorandom code and compares it to that arriving from the satellite. A time offset is computed by an autocorrelation function between the received pseudorandom code from the satellite and that generated by the receiver. This offset contains the signal travel time and the mis-synchronization of the satellite and receiver clocks. The pseudorange measurements typically have a precision on the order of 1-10 meters. The equation for the pseudorange observable is (Seeber, 2003):

$$P_i = \rho + c(dt_r - dt^s) + I_i + T + \varepsilon, \quad (2.1)$$

where i is the frequency index 1 and 2 for frequency L_1 and L_2 respectively, P is the pseudorange, ρ is the range from the receiver to the satellite, c is the vacuum speed of light, dt_r and dt^s are the offsets of the receiver and satellite clock with respect to GPS time, I is the ionosphere delay and T is the troposphere delay, ε represents the effect of multipath and receiver noise.

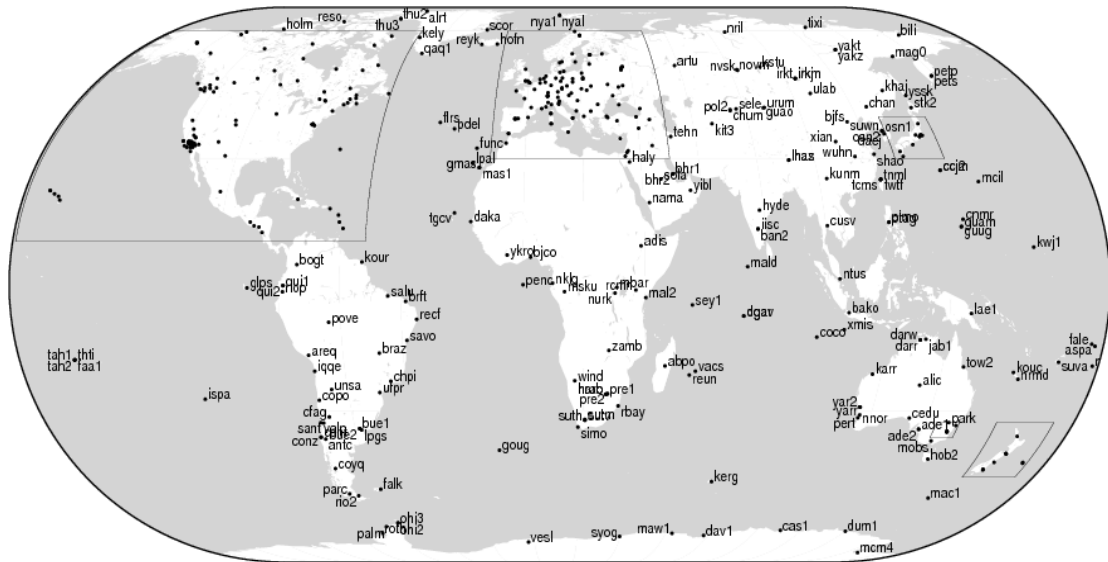
Beside the pseudorange the two carrier phase (L_1 and L_2) observations can also be used as phase measurements. The phase observations have a noise of a few millimeters and are more accurate than pseudoranges. For high-precision GPS positioning and GPS meteorology the phase observations are more important. The receiver records the fractional phase of L_1 and L_2 from a GPS satellite and keeps track of the changes of the received carrier phase. The initial phase, called ambiguity, is unknown. In order to use phase observations the so-called phase ambiguity must be resolved or accounted for (Seeber, 2003). The equation for the carrier phase measurements L in units of length can be written as:

$$L_i = \lambda_i \cdot \varphi_i = \rho + c \cdot (dt_r - dt^s) - I_i + T + \lambda_i \cdot N_i + \varepsilon, \quad (2.2)$$

where λ is the carrier wavelength, φ is the carrier phase observation in cycles and L is carrier phase observation in meter, I is the ionospheric delay, N is the integer ambiguity for a particular receiver-satellite pair, ε describes un-modeled effects, modeling errors and measurement errors for carrier phase observations. The ionospheric delay for carrier phase measurements has the same magnitude as for pseudorange measurements, but is of the opposite sign.

The International GNSS Service (IGS)

The International GNSS Service, formerly the International GPS Service, presently has 12 Analysis Centers (ACs). Each AC computes products based on data collected from a global network of continuously operating GPS stations equipped with DF receivers (**Figure 2.2**). The IGS ACs use the collected data from more than 360 stations worldwide to provide precise GPS ephemerides and adjusted clock parameters. GFZ operates one of the global Analysis Centers since the very beginning of the IGS activities. A list of IGS products is shown in **Table 2.1**.



EMF 2011 Jun 01 18:45:41

Figure 2.2: IGS network of globally distributed tracking sites (<http://igsb.jpl.nasa.gov>, 2011).

Products Type	Orbit		Clock		Latency	Update intervals	
	RMS	interval	RMS	interval			
Broadcast	~ 100 cm	Daily	~ 5 ns	Daily	Real time		
IGU	Ultra-Rapid predicted half	~ 5 cm	15 min.	~ 3 ns	15 min.	Real time	Four times each day
	Ultra-Rapid observed half	< 3 cm	15 min.	~ 150 ps	15 min.	3-9 h	Four times each day
IGR	Rapid	~ 2.5 cm	15 min.	~ 75 ps	5 min	17 - 41 h	Daily
IGS	Final	~ 2.5 cm	15 min.	~ 75 ns	30 s	12 - 18 days	Weekly

Table 2.1: Broadcast values and IGS combined orbit and clock products (<http://igsb.jpl.nasa.gov/components/prods.html>, 2011).

GNSS - Global Navigation Satellite Systems

In the last years the Russian counterpart GLONASS improved its stability with the help of India. As of June 2011, GLONASS consists of 27 satellites, 23 of them are in operation (<http://www.glonass-ianc.rsa.ru>). All the GLONASS satellites operate at an altitude of 20,000 km in 3 orbital planes. The GLONASS satellites transmit radio signals on a different frequency using a 15-channel frequency division multiple access (FDMA) technique spanning either side from 1602.0 MHz. The latest GLONASS-K2 satellites to be launched in 2013 will introduce a new code division multiple access (CDMA) signal, which allows messages from individual GLONASS satellites to be distinguished from each other based on unique encodings.

Additional systems in Europe (Galileo) and China (Compass) are now in development. The general name given to all these systems is Global Navigation Satellite Systems (GNSS). Currently about 10 GPS satellites can be observed simultaneously in Europe. If the other three GNSS systems are fully in operation, the number of the observed satellites can increase to about 40. The spatial coverage of the atmosphere with tropospheric slant paths will considerably be improved by an increasing number of GNSS satellites leading to a more homogeneous coverage of the troposphere in space and time.

2.2 GPS observation equations

To retrieve the ZTD from the GPS data two basic observables are used:

- Pseudoranges from code measurements,
- Carrier phases or carrier phase differences.

The pseudoranges have a noise level of some decimeters up to a few meters (Seeber, 2003) and are primarily used to synchronize receiver clocks to GPS time and to set initial ambiguities of the carrier phases. In comparison to pseudoranges the carrier phases are much more precise with a precision of a few millimeters. For this reason the carrier phases are the most important observation type for precise GPS applications like precise positioning and GPS meteorology.

2.2.1 Linear combinations of observations

The pseudorange and carrier phase observables (P_1 , P_2 , L_1 and L_2), expressed in units of distance (meters), can be linearly combined to eliminate or isolate certain components of the observation equation. For instance, a linear combination can be formed to remove the effect of the ionosphere. Similarly, a linear combination can be formed that isolates the ionosphere. These combinations are listed below, followed by a brief description.

Ionosphere-free combination

From the P_1 , P_2 , L_1 and L_2 observation Eq. (2.1) and Eq. (2.2) the ionosphere-free linear combination can be described as:

$$\begin{aligned}
 L_3 &= \frac{f_1^2 \cdot L_1 - f_2^2 \cdot L_2}{f_1^2 - f_2^2} \\
 &= \rho + c \cdot (dt_r - dt^s) + \frac{c \cdot f_1 \cdot N_1 - c \cdot f_2 \cdot N_2}{f_1^2 - f_2^2} + T + \varepsilon_{L_3}, \\
 P_3 &= \frac{f_1^2 \cdot P_1 - f_2^2 \cdot P_2}{f_1^2 - f_2^2} \\
 &= \rho + c \cdot (dt_r - dt^s) + T + \varepsilon_{P_3}.
 \end{aligned} \tag{2.3}$$

The ionospheric delay is frequency-dependent; Eq. (2.3) eliminates the effect of the first-order ionospheric delay on the observables, and is widely used in GPS data

processing. The disadvantage of this linear combination is that the noise from the L_1 and L_2 carrier phase measurements is increased by nearly a factor of three (Seeber, 2003), and that the ambiguities cannot directly be solved as integer.

For receivers that have DF capability, the L_3 combination is usually the preferred method to use in geodetic and atmospheric applications. Only for networks of stations operated over short distances, i.e., $< 5\sim 10$ km, L_1 or L_2 observations are used individually (Janssen and Rizos, 2005) and the ionospheric effects can be considerable reduced through single differencing between stations. The GPS data processing package EPOS uses the L_3 combination to estimate the tropospheric delay as well as station coordinates and receiver clock biases.

Ionosphere linear combination (geometry-free linear combination)

$$\begin{aligned} L_4 &= L_1 - L_2 = I_4 + \lambda_1 N_1 - \lambda_2 N_2 + \varepsilon, \\ P_4 &= P_1 - P_2 = -I_4 + \varepsilon, \\ I_4 &= -\left(1 - \frac{f_1^2}{f_2^2}\right) \cdot I_1. \end{aligned} \quad (2.4)$$

The carrier phase ionosphere linear combination L_4 eliminates the geometric, tropospheric, and clock synchronization components of the carrier phase equation (Schaer, 1999). The noise of L_4 is about 1.63 times the noise of the L_1 observations. Since the combination of the initial phase ambiguities remains, L_4 can only represent the complete variation of the ionospheric delay during a continuous tracking. Similar to L_4 the code combination P_4 is also a reasonably smooth function. However, sometimes multi-path effects on P_4 are larger than centimeter level and L_4 cannot be successfully calibrated by P_4 . This linear combination is used to estimate global, regional, and high-resolution local ionosphere models. With these models the ionospheric correction for SF GPS receiver can be calculated with different accuracy (from several millimeters to a few meters) (Bern, 2008).

For the GPS data pre-processing it is possible to construct a polynomial fit for L_4 , and to identify discontinuities such as cycle slips or outliers. But under high ionospheric activity conditions it is difficult to detect cycle slips with the ionosphere linear combination (Blewitt, 1990).

Wide-lane linear combination

$$\begin{aligned} L_w &= \frac{f_1 L_1 - f_2 L_2}{f_1 - f_2} = \rho + \frac{If_1 f_2}{f_1^2 - f_2^2} + \lambda_w N_w + \varepsilon_{L_w}, \\ P_w &= \frac{f_1 P_1 + f_2 P_2}{f_1 + f_2} = \rho + \frac{If_1 f_2}{f_1^2 - f_2^2} + \varepsilon_{P_w}. \end{aligned} \quad (2.5)$$

Eq. (2.5) is called the wide-lane linear combination. The combined wavelength λ_w of the L_1 and L_2 carrier phase measurements amounts to 84 cm. This long wavelength simplifies ambiguity resolution. It is commonly used in the analysis of stations that are separated by more than a few tens of km. In the data pre-processing it can also be applied for detecting cycle slips (Blewitt, 1990).

2.2.2 Differencing of observations

In addition, to the linear combinations of different observables, observations from pairs of stations and satellites can be differenced (**Figure 2.3**). Differencing is commonly used to eliminate satellite and receiver clock errors. The two most common differencing equations used are the single difference and the double difference.

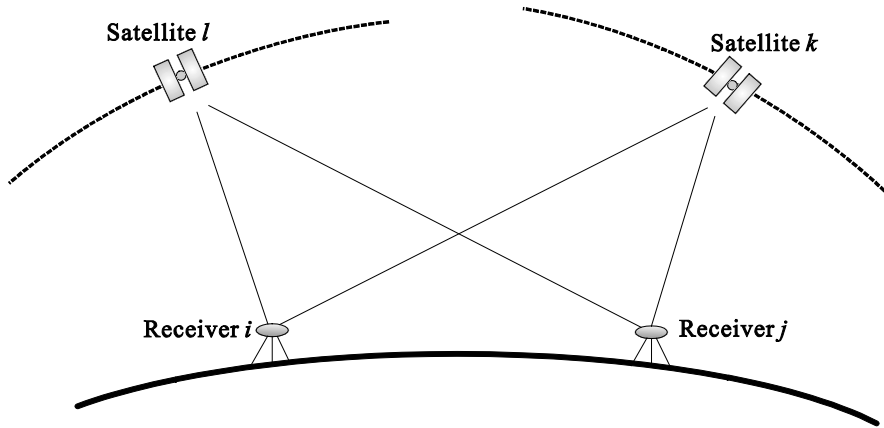


Figure 2.3: Four observations from two receivers and two satellites.

Single difference (SD)

A single difference observation is usually the combination of observations from two stations and one satellite or one station and two satellites.

For two stations and one satellite the observable reads:

$$\begin{aligned}\Delta L_{ij}^k &= L_i^k - L_j^k = \Delta \rho_{ij}^k + c \cdot \Delta dt_{ij} - \Delta I_{ij}^k + \Delta T_{ij}^k + \lambda \cdot \Delta N_{ij}^k + \varepsilon_{L,ij}^k, \\ \Delta P_{ij}^k &= P_i^k - P_j^k = \Delta \rho_{ij}^k + c \cdot \Delta dt_{ij} + \Delta I_{ij}^k + \Delta T_{ij}^k + \varepsilon_{P,ij}^k,\end{aligned}\quad (2.6)$$

the subscripts i and j denote the receivers i and j , respectively, the superscript k and l denotes the satellites k and l . In this SD the satellite clock errors are almost eliminated. For short baselines up to a few kilometers the ionospheric delay and the tropospheric delay can be canceled or largely reduced by forming the single difference between stations, because the signal paths from the same GPS satellite are very close to each other.

For one station and two satellites the observable reads:

$$\begin{aligned}\nabla L_i^{lk} &= L_i^l - L_i^k = \nabla \rho_i^{lk} + c \cdot \nabla dt^{lk} - \nabla I_i^{lk} + \nabla T_i^{lk} + \lambda \cdot \nabla N_i^{lk} + \varepsilon_{L,i}^{lk}, \\ \nabla P_i^{lk} &= P_i^l - P_i^k = \nabla \rho_i^{lk} + c \cdot \nabla dt^{lk} + \nabla I_i^{lk} + \nabla T_i^{lk} + \varepsilon_{P,i}^{lk},\end{aligned}\quad (2.7)$$

which forms the single differences between satellites, and the receiver clock term is canceled. Since most GPS receivers are equipped with inexpensive quartz crystal clocks, the receiver clock term is one of the most significant error sources.

Double difference (DD)

A double difference is the difference of two single differences. It is the combination of observations from two stations and two satellites. In this combination, satellite clocks as well as station clocks are almost eliminated.

$$\begin{aligned}\nabla\Delta L_{ij}^{kl} &= \Delta L_{ij}^k - \Delta L_{ij}^l = \nabla\Delta\rho_{ij}^{kl} - \nabla\Delta I_{ij}^{kl} + \nabla\Delta T_{ij}^{kl} + \lambda \cdot \nabla\Delta N_{ij}^{kl} + \varepsilon_{L,ij}^{kl}, \\ \nabla\Delta P_{ij}^{kl} &= \Delta P_{ij}^k - \Delta P_{ij}^l = \nabla\Delta\rho_{ij}^{kl} + \nabla\Delta I_{ij}^{kl} + \nabla\Delta T_{ij}^{kl} + \varepsilon_{P,ij}^{kl}.\end{aligned}\quad (2.8)$$

For GPS remote sensing the double differencing is a commonly used technique. DD permits ambiguity-fixing solutions since the hardware delays cancel and thus provides very accurate results. There are some disadvantages when it is used to measure atmospheric delays. First, for baselines shorter than a few hundred kilometers the ZTD solution is a relative estimate, because a satellite observed at each end of the baseline is seen almost at identical elevation angles. Second, to build double difference observations data synchronization between the receivers is required. An alternative to the DD approach is the Precise Point Positioning (PPP) technique.

2.3 Precise Point Positioning (PPP)

The theoretical foundation of the PPP is documented in Zumberge et al. (1997). Unlike the DD mode, the PPP uses ionosphere-free, un-differenced phase and pseudorange observations from a single GPS receiver. As a result the common errors do not cancel, such as satellite clock errors and receiver clock errors. Introducing precise satellite orbit and clock information computed by the International GNSS Service (IGS), the remaining errors are station parameters such as tropospheric delays, receiver clocks and coordinates. For GPS/MET the station coordinates are determined using IGS final products and are then fixed during the tropospheric delay estimation.

The PPP allows analyzing data from hundreds or thousands of sites in parallel, with results of comparable quality to the simultaneous analysis of all data. Due to the steadily increasing number of sites in Germany, the PPP mode is used in EPOS. The computation time could be kept within 15 minutes for more than 300 stations even when setting up an increasing number of parameters like tropospheric zenith delay and gradients with high sampling rate (15 or 30 minutes) (Gendt et al., 2004).

The disadvantage of the PPP is that precise GPS satellite orbits and clocks are needed. The precise satellite orbits and clocks must be computed from a high-quality global GPS tracking network. In the data processing the PPP mode is unable to take correlations between stations into account (Seeber, 2003). Compared with the DD mode, the common errors between stations, e.g., orbit and clock errors cannot be reduced in the PPP mode.

Antenna corrections

Due to the separation between the satellite's center of mass and the antenna phase center position, the correction of satellite antenna Phase Center Offsets (PCO) and Phase Center Variations (PCV) must be considered in PPP for highly precise applications. Like the satellite antenna PCO, the phase center of a receiver antenna is different from the

antenna reference point and should be taken into account. The phase center of the receiver antenna varies with the changing direction of the received signal. The corrections of PCV should be applied.

Besides individual corrections for a specific antenna, there are also type-specific antenna corrections. These are mean values from calibrations of several antennas of the same antenna type, which can then be used for all antennas of this type. The use of individual calibration values is preferred, since PCO and PCV of one antenna can be different from those of other antennas of the same type, with differences even up to 15 mm at low elevations for L_3 observation (Seeber, 2003; Wübbena et al., 2000).

Receiver noise and multipath

Receiver noise results from the fact that GPS phase and code observations cannot be measured perfectly but are subject to random influences. For classical receivers the resolution of the observation is about 1% of the signal wavelength (**Table 2.2**):

C/A-code	$\lambda \approx 300$ m	noise ≈ 3 m
P-code	$\lambda \approx 30$ m	noise ≈ 30 cm
carrier	$\lambda \approx 20$ cm	noise ≈ 2 mm

Table 2.2: Observation noise (Seeber, 2003).

For modern receivers, the magnitude of the phase noise was decreased below 1 mm, which reduces the code noise to the 10 centimeter level (Seeber, 2003).

Multipath propagation is caused by one or more reflected signals, which reach the antenna, in addition, to the direct signal. Multipath propagation could affect both code and carrier measurements. The magnitude of the multipath errors is related to the environment of the station location. The effect on P-code measurements can reach decimeters to meters, and is two orders of magnitude larger than on carrier phase measurements. Many cycle slips are caused by multipath effects. Using high-quality antennas (choke ring and ground plane) multipath effects can be greatly reduced. The polarization of the GNSS signal (direct signal: right-handed, reflected signal: left-handed) can be used for the elimination of reflected components in the received signal (Hofmann-Wellenhof et al., 2001).

Relativity

The GPS satellite clock and the clock on the ground operate at different gravitational potential values and move with different velocities, which causes an apparent frequency shift in the satellite oscillator (with respect to the ground). The relativistic correction Δt_r is given as (ICD, 2000):

$$\Delta t_r = -4.442807633 \cdot 10^{-10} \cdot e \cdot \sqrt{a} \cdot \sin E, \quad (2.9)$$

where e is the GPS orbit eccentricity, a is the orbit semi-major axis in units of meter and E is the satellite eccentric anomaly. The maximum value of the relativity correction can reach 70 nanoseconds in time, and 0.01 nanoseconds/sec for the clock drift (Seeber, 2003). In the PPP the relativity correction must be applied.

Earth tides

The Earth responds as an elastic body to external forces caused by the Sun and Moon. They cause periodic deformations of the Earth's crust and lead to vertical and horizontal site displacement, which can be computed quite accurately from simple Earth models, while the ocean tides are strongly influenced by the coastal outlines and the shape of the near-coastal ocean floor. The magnitude of the Earth tides is dependent on station latitude, tide frequency, and sidereal time. The effect of the tidal variation is larger in the vertical component and can reach as much as 50 cm (Sun + Moon) and 5 cm in the horizontal plane (H roux and Kouba, 2001). The displacement caused by the solid Earth tide may be divided into a permanent part and a periodic part. The periodic part can be largely averaged out in the static positioning of an entire day while the permanent part that can reach 12 cm in the middle latitude region remains (H roux and Kouba, 2001). Neglecting the Earth tide correction can result in position errors in PPP of up to 12.5 cm and 5 cm in the radial and north directions, respectively (Kouba, 2009).

Ocean tides

When stations are located not too far from the nearest coast line (<1000 km), the ocean loading effects should be taken into account for applications such as point positioning with centimeter or millimeter accuracy, or GPS meteorology (Kouba, 2009). Otherwise, this effect will be mapped into the ZTD and station clock correction.

Phase wind up

Since GPS satellites transmit right-hand circularly polarized radio signals on L_1 and L_2 , the received carrier phase observations from a station are dependent on the relative orientation of the satellite and receiver antennas. Due to the continuous reorientation of the satellite's solar panels towards the Sun, the satellite antenna rotates slowly. The relative rotation between satellite and receiver antenna will change the observed carrier phase up to one cycle. This effect is called "phase wind up" (Wu et al., 1993). The effect of the phase wind up is negligible for DD with baselines up to a few hundred kilometers. For PPP it is quite significant since this effect can reach up to one half of the observation wavelength, and must be corrected.

2.4 Overview on EPOS software

There are only few GPS software packages available for geodetic and atmospheric scientific applications. The most commonly used packages are GAMIT (King, 2003), GIPSY (Zumberge et al., 1997), Bernese (Dach et al., 2005), and GFZ's own GPS software package EPOS (Earth Parameter and Orbit determination System) (Gendt et al., 1999). There are some differences between the software packages. GAMIT uses the double difference measurements as the fundamental observable. Bernese can analyze data using both un-differenced and double differenced observations. GIPSY and EPOS use the un-differenced one-way phase measurement, and estimate the receiver clock errors as additional random walk parameters.

At GFZ the GPS data processing procedure using the EPOS software includes several separate parts to generate tropospheric products in Near-Real-Time (NRT) as well as in post-processing mode.

For the NRT mode EPOS is set up with the following main tasks: Data pre-processing, orbit and clock analysis, ZTD analysis, ZTD product generation, ZTD to IWV conversion, archiving and export.

The details of each task are described below. The post-processing mode uses the IGS orbit and clock products, and the task ‘orbit and clock analysis’ is omitted as compared to the NRT mode. Here the NRT mode of the EPOS software package will be described in detail.

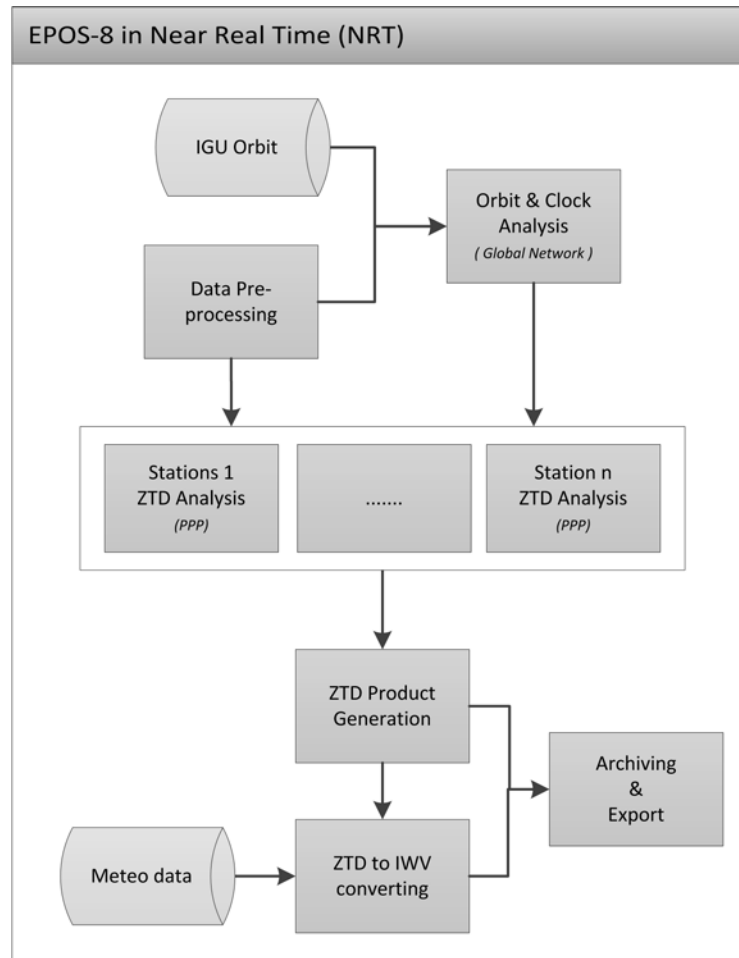


Figure 2.4: Flow diagram of the main components of EPOS.

The main parts of the NRT processing are shown in **Figure 2.4**. Two GPS networks are used in the NRT mode: a global GPS network with about 40 well-distributed reference stations and a local network with about 320 GPS stations in Germany for GPS meteorology. The IGU orbit prediction is used as initial orbit. To achieve sufficiently accurate GPS orbits for the ZTD estimation, the data from the global GPS reference stations are used to improve the orbits and to estimate the satellite clock corrections. The data from the local network are processed in Precise Point Positioning (PPP) mode to retrieve the ZTDs. With additional meteorological data (temperature and pressure) the estimated ZTDs can be converted to IWVs. Finally, the ZTD and IWV products are exported for meteorological applications, e.g., weather prediction, and stored in the GFZ data archive.

2.4.1 Data pre-processing

In the data pre-processing the RINEX raw data from both networks is checked and prepared for the analysis (**Figure 2.5**). All the incoming GPS data are stored in RINEX files (or compressed RINEX files) on data servers. For a defined station list and a given time period the data servers are scanned to search the stations with available GPS data. Then two station lists are created, one includes the global reference stations, which are used for orbit improvement and satellite clock estimation; the other includes the local stations. For these stations the troposphere products are generated. According to the two station lists the available RINEX files are imported and uncompressed; the original observation *raw_rin* files are generated in this step. Due to GPS P1-C1 code biases of some receiver types the *cc2noncc* correction is applied to correct the pseudorange observations obtained by cross-correlation (cc) style receivers to non-cross-correlation (noncc) observations. The subroutine TRIMCORR has the function to generate the consistency of variations between pseudorange and phase observables from some Trimble receivers.

In EPOS the pre-processing module “*TURBOEDIT*” is based on the algorithm TurboEdit (Blewitt, 1990). The *TURBOEDIT* cleans the RINEX data station by station. The short data spans and the outliers are removed, at the same time the cycle slips are detected and flagged.

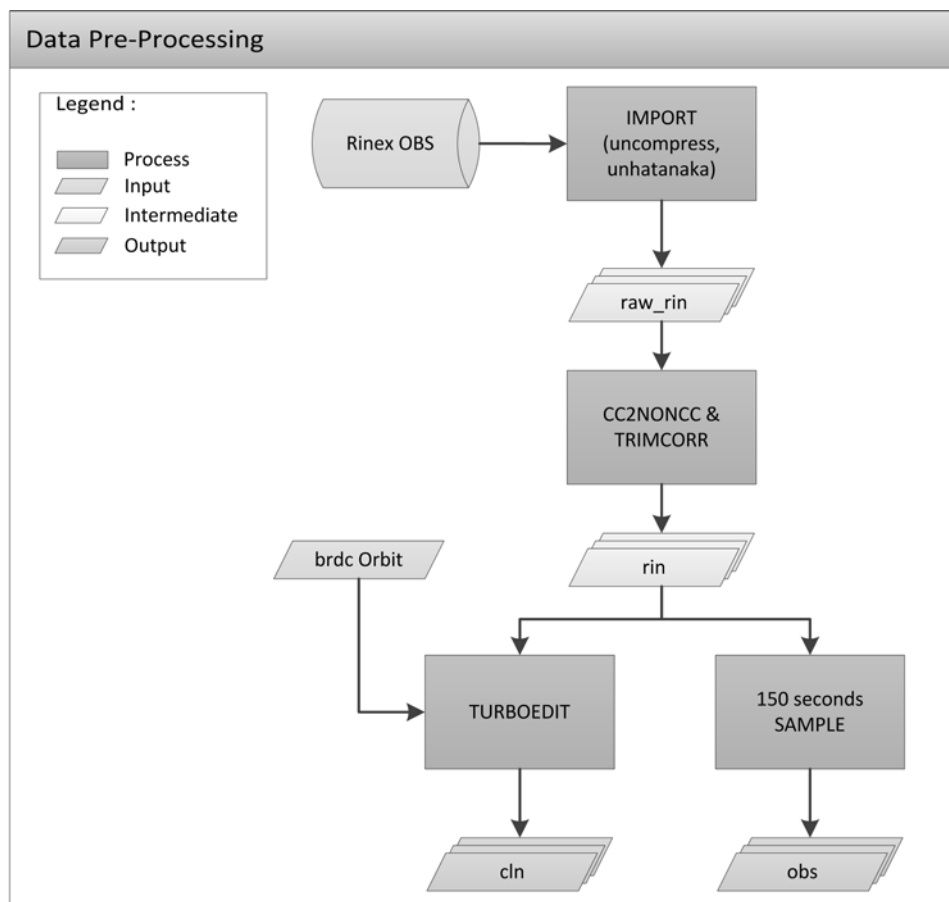


Figure 2.5: Flow diagram of GPS data pre-processing in EPOS.

All the information from the *TURBOEDIT* is registered in a so-called *cln* file for each station. The observation files of selected sites corrected for *CC2NONCC* and *TRIMCORR* together with pre-processing *cln* files will be used to generate a single data file in the format for the EPOS software. Compared with keeping a preprocessed data file, the advantage of using such editing *cln* file is to keep all pre-processing information in a relatively small-size file to save computer storage space.

The GPS data *rin* files have a sampling interval of 30 seconds. For further analysis the observation data are down sampled to 150 seconds. At the same time the observation types, which are not used in the further analysis, are excluded. The remaining observations are saved in *obs* files. With the *cln* files the GPS observations are ready for the data analysis.

2.4.2 Near-real-time orbit and clock products

In this step the observations from the global GPS network are processed to improve the IGU orbits and determine satellite clocks as well (**Figure 2.6**). The main characteristics of the EPOS network solution are listed in **Table 2.3**

Data cleaning in the network solution

Small cycle slips and outliers, which are not perceived by the pre-processing, can further be detected in the network solution. The network cleaning procedure is carried out iteratively. After an iteration the post-fit residuals are analyzed, and the most significant cycle slips or bad observations are recognized and flagged out. Then the data without the flagged observations are processed again to estimate the parameters and produce new post-fit residuals. The iteration stops when no more cycle slips or bad observations are found. Normally 5 iterations are sufficient. The new cycle slips and bad observations will be registered in the data-editing *cln* files.

Satellite orbit improvements and clock estimation in the network solution

After the network cleaning procedure the satellite orbit improvements and clock corrections are estimated using the remaining observations. The estimated parameters include initial conditions of orbits parameters, satellite clock corrections, dynamical parameters (e.g., solar radiation pressure coefficients), station coordinates, Earth rotation parameters, ionosphere-free ambiguities, receiver clocks at each epoch, ZTDs as well as troposphere gradients. The improved satellite orbits and estimated satellite clocks are converted to the *SP3* orbit format and the *CLK* clock format.

This part comprises the following programs:

INSES: The observation *obs* files and the corresponding *cln* files from all stations are read, and are written in one file, named *session* file, with other information, e.g., time interval, elevation cut-off angle, list of stations/satellites and observation types. The generated *session* file is an EPOS internal observation input file.

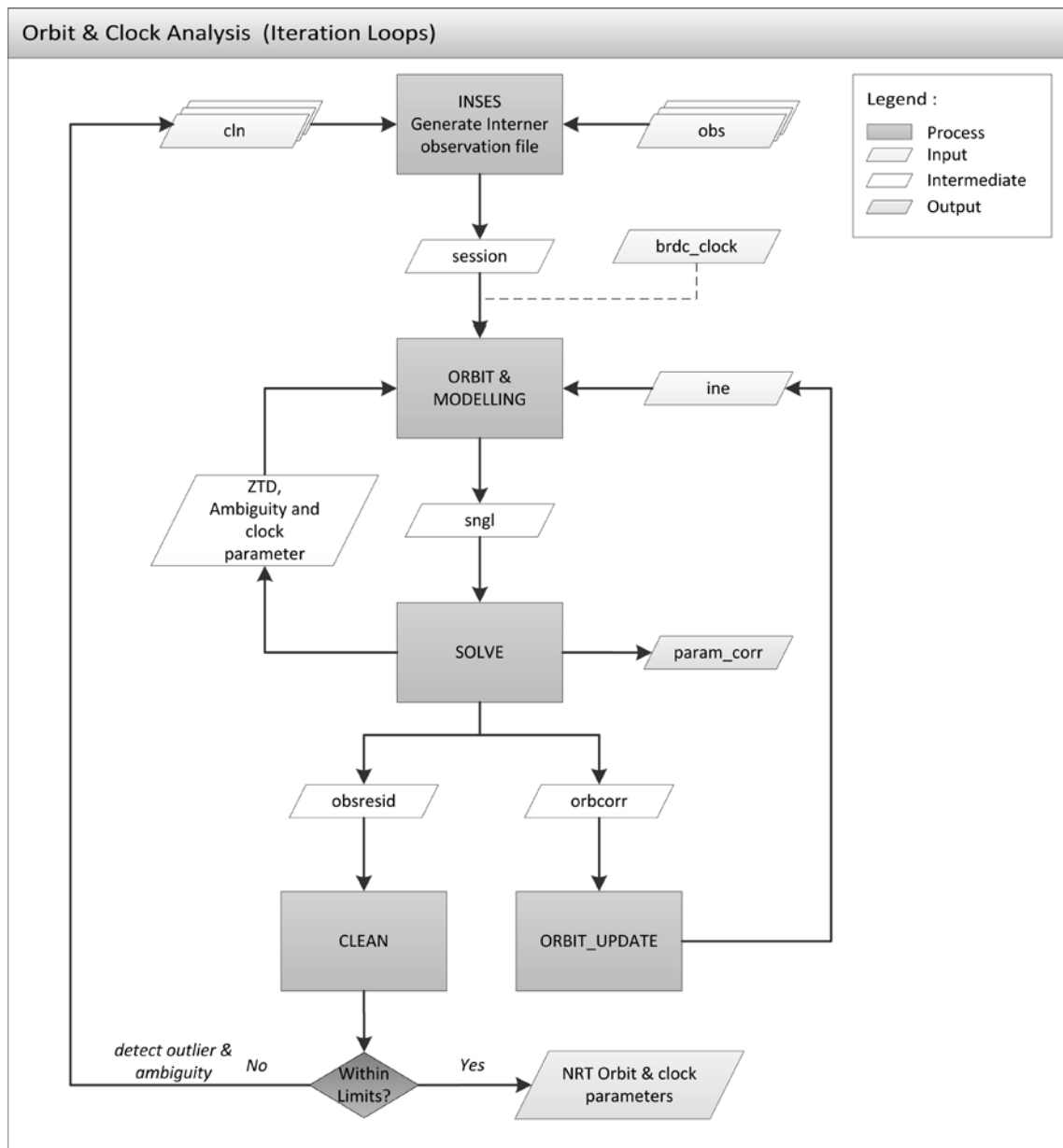


Figure 2.6: Flow diagram of GPS satellite orbit and clock determination with EPOS.

ORBIT & MODELLING: According to the satellite orbit status *ine* file the satellite orbits are integrated to the epochs of the observations considering the dynamical models, such as gravity field, solar radiation pressure, etc. After the orbit interpolation the observations are modeled and corrected epoch by epoch using parameters like ambiguities, clock correction, PCV correction, tidal displacement and tropospheric delays etc. For the first iteration the tropospheric delays are calculated from the Saastamoinen model. According to the estimated parameters the observation equations with all partial derivatives are saved in a *sngl* file.

SOLVE: Using the *sngl* file SOLVE inverts and solves the normal equation system using the least-squares method. The adjustments of the estimated parameters are saved for the next iteration or the products. The post-fit residuals are written in the *obsresid* file. In a summary file the statistical information of the adjustment process is given.

CLEAN: In this step the outliers and cycle slips are detected using the post-fit residual *obsresid* file, and are added to the *cln* file for the next iteration. If no more outliers or

cycle slips are found, the network cleaning procedure is finished, and is ready for the satellite products generation.

ORBIT_UPDATE: With the adjustment of the orbit parameters the satellite orbit status *ine* file is updated.

Coordinate system	ITRF 2005
Orbits and pole	IGU
Basic observable	Un-differenced ionosphere-free combination
Sampling interval	150 seconds
Elevation cut-off angle	7 °
Elevation-depended weighting	$1/[2\sin(e)]$ for $e < 30$ °
Ocean loading	FES2004
Tidal effects	IERS Conventions 2003
Phase centre correction	Absolute antenna PCV IGS model
A priori zenith delay	Saastamoinen
Pressure and temperature	Global Pressure and Temperature model (GPT)
Mapping function	Global Mapping Function (GMF)
ZTD estimation interval	2 hours
Gradient in east and north	12-hour

Table 2.3: Main characteristics of the EPOS network solution.

2.4.3 Tropospheric product generation

It is possible to generate ZTDs and STDs using the PPP or the double-differencing processing. Both of them have advantages and disadvantages. The PPP technique models the line-of-sight observations from the receiving antenna to each GPS satellite individually. Therefore the ZTD and STD products of each station are independent from all other stations. The anisotropic tropospheric state is described by the gradients and the residual directly. The disadvantage of the PPP approach is that the PPP analysis needs accurate satellite clock values and orbit parameters, and it is not possible to resolve the integer carrier phase ambiguities. The STD products using the DD technique are more accurate than using the PPP technique, but they are not independent from each other because of the combination of 4 simultaneous observations. The direct transformation from double-difference STDs to one-way STDs is therefore impossible.

In the previous step the satellite clock values and improved orbits were calculated using a large global GPS tracking network. With the improved satellite orbits and estimated clocks the GPS data, in our case the German SAPOS data, are processed in the PPP mode to retrieve ZTD and STD products for each station. The ZTD is estimated every 15 minutes, troposphere gradients in east and north directions are estimated in hourly bins. The structure of the ZTD analysis is similar to the last step ‘orbit and clock determination’, only without the orbit improvement. With fixed orbit and clock products the ZTD for each station is estimated. Similar to the network cleaning procedure the cycle slips or bad observations are detected iteratively, until there is no cycle slip or bad observation left in the remaining observations. Then the ZTD and gradients estimated in the last iteration are saved in the SINEX² formatted .zpd files.

² Solution (Software/technique) INdependent EXchange

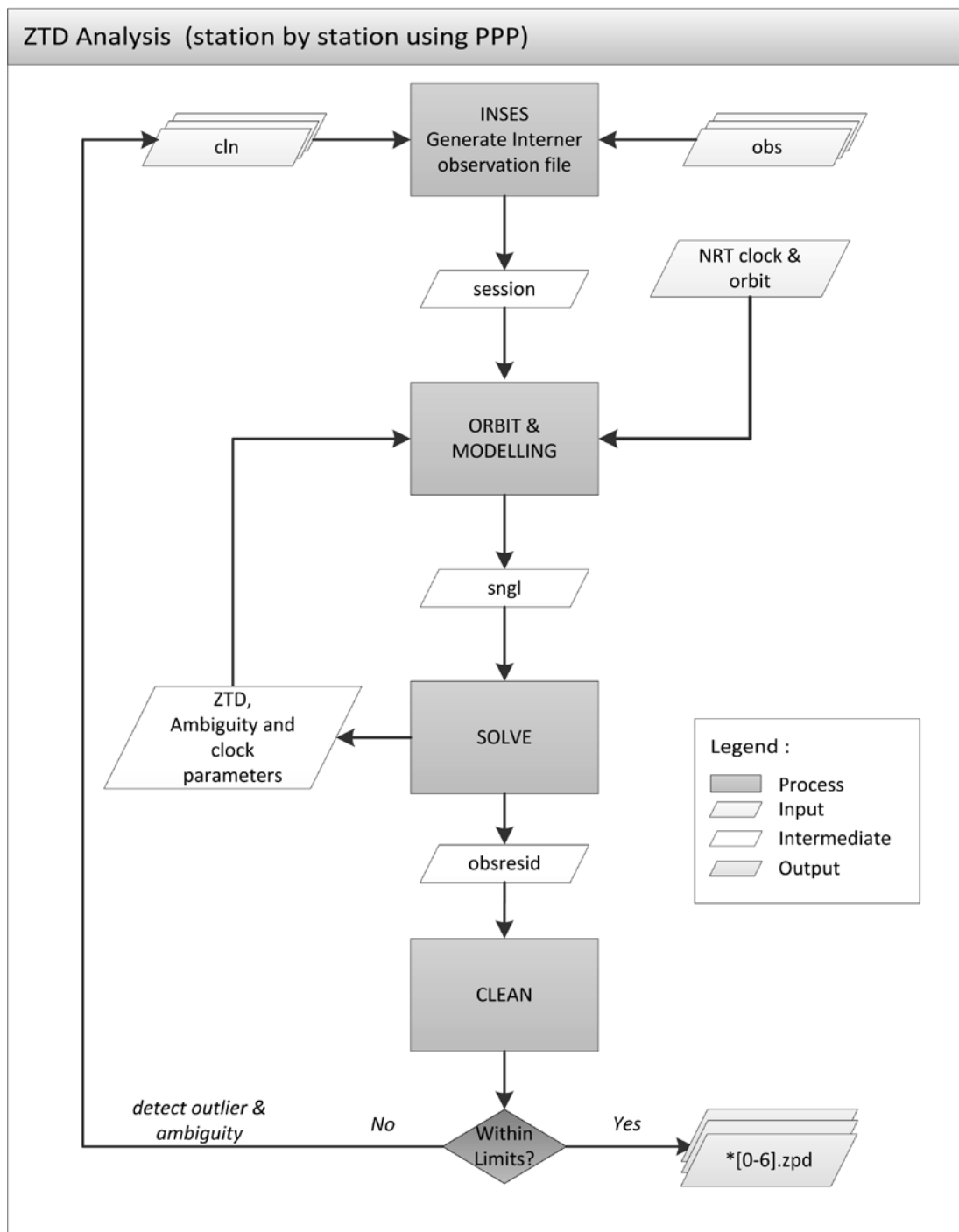


Figure 2.7: Flow diagram of ZTD generation in EPOS using PPP.

Integrated water vapor (IWV)

The ZTD can be converted to IWV using meteorological observations (Figure 2.8). However, for the majority of GPS sites in Germany no meteorological sensors are installed. Therefore, the temperature and pressure have to be interpolated using the observations from the dense synoptic network of the German Weather service (DWD). Before the interpolation the quality of the SYNOP data is checked by mutual interpolation in the whole network. The SYNOP stations, which fail in the quality control, will not be used for the interpolation. In the function “Meteo data interpolation”

temperature and pressure are interpolated to the GPS stations. Statistics show a typical RMS of 0.3 hPa and 1 K for the pressure and temperature interpolation, respectively. Errors of 0.5 hPa correspond to 0.2 kg/m^{-2} IWV and are acceptable for numerical weather prediction applications, even random fluctuations up to 1 hPa may be tolerated (Gendt et al., 2001). 1 K temperature error causes about 0.2% IWV error and can be ignored. The converted IWV will be saved in the SINEX formatted .tro file for each station in the function PROD_ZTD.

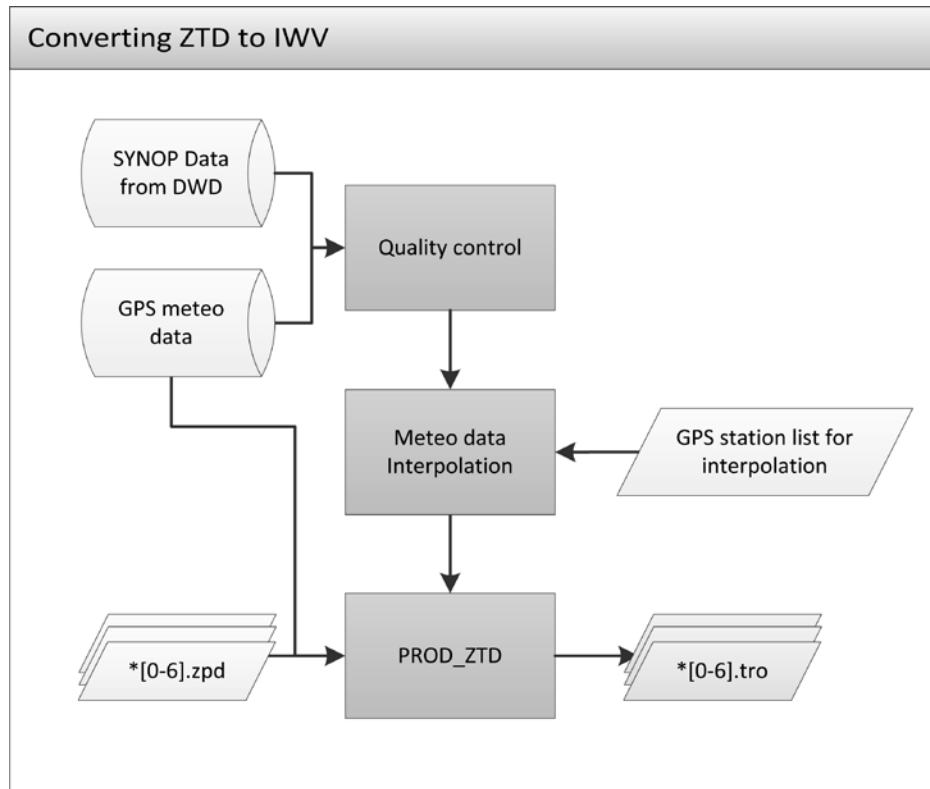


Figure 2.8: Flow diagram of IWV generation in EPOS.

2.5 Description of the IGS data used

Usually the IGS Rapid or Final products are used to reduce the errors in GPS satellite orbits and clocks compared to the IGU products, and accurate troposphere products can be achieved. However, the IGS Rapid or Final products have time latency from several hours to some days (<http://igscb.jpl.nasa.gov/>). For meteorological forecasting applications the GPS-derived water vapor parameters have to be produced on an hourly basis. Therefore, high-quality satellite orbits and clock products are required in NRT.

In the IGS ultra-rapid orbits (IGU) predicted orbits are available four times a day, and their accuracy is about 5 cm. Because of unpredictable non-conservative forces the predicted orbit accuracy decreases with time. When a satellite has a maneuver, the accuracy of the predicted orbit decreases to a few hundred meters. In addition, the IGU predicted clocks have an accuracy of about 3 ns (**Table 2.1**). For operational weather forecasts the accuracy of the orbits and clocks are insufficient for providing ZTD products with adequate accuracy.

To improve the IGU prediction quality the GPS data from about 40 well-distributed global stations in a 12-hour data window are used. In addition, five German stations are included for good clock coverage over Germany (**Figure 2.9**). The predicted IGU orbits of GFZ with 3-hour repetition are used as initial orbits for the orbits and clocks adjustment. The improved predicted IGU orbits are named GASP³ orbits—hourly estimated orbits from NRT analysis based on 12-hour data windows (Gendt et al., 2004).

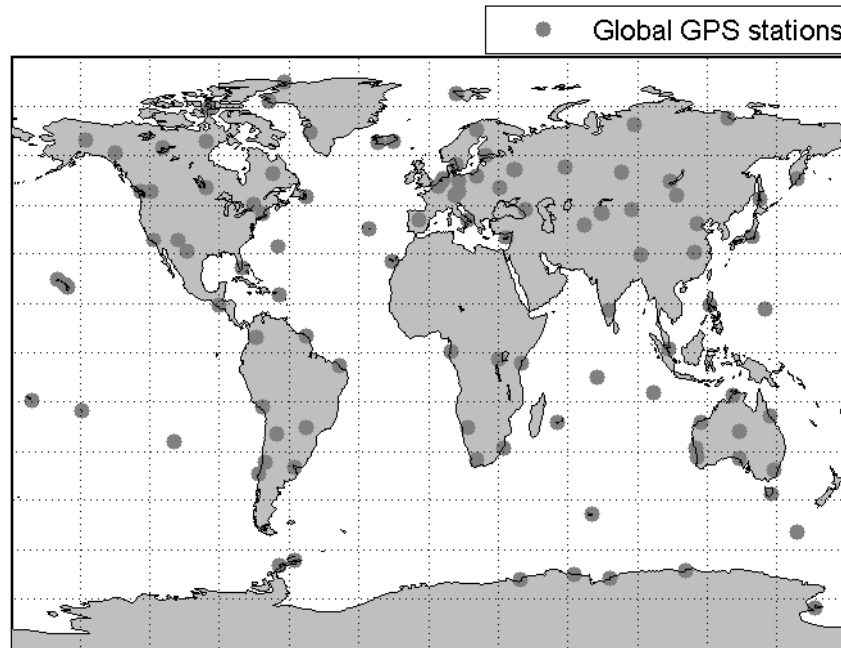


Figure 2.9: 40 global GPS stations are selected from about 160 global IGS stations (black dots) according to data availability.

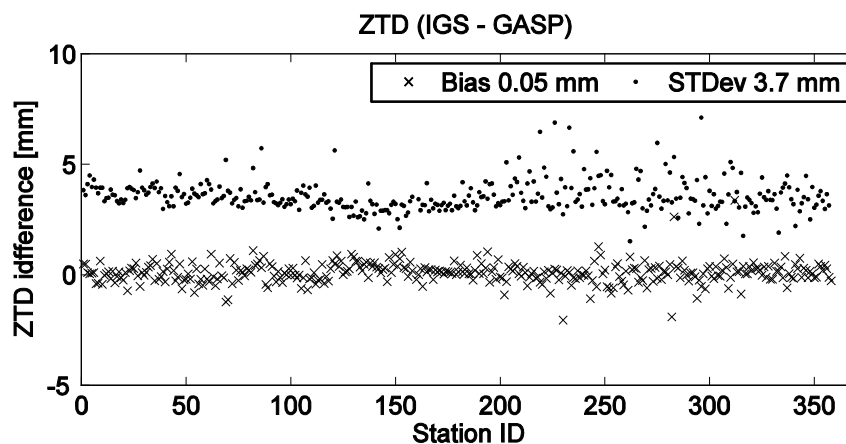


Figure 2.10: The statistics of the ZTD differences for 360 German stations using IGS final products and GASP products: the crosses indicate the bias; the dots are standard deviations.

To validate the NRT GASP orbit and clock products the data from about 360 Germany GPS stations for the GPS week 1433 in 2007 (DOY 175 – 181) were analyzed. The retrieved ZTDs were compared with those using final IGS orbit and clock products. The

³ GPS Atmosphere Sounding Project

biases and standard deviations of the estimated ZTDs are given for each station in **Figure 2.10**. The total ZTD differences have a standard deviation of 3.7 mm with a negligible bias of 0.05 mm.

Besides consistency checks between NRT and post-processed estimated ZTDs using EPOS software, important checks are performed with other IGS analysis centers. 34 of the 360 test stations are IGS stations, the ZTDs of the 34 stations are compared with those from JPL. **Figure 2.11** shows the statistics of a ZTD comparison for the 34 stations. The ZTDs estimated using GASP products are in good agreement with the ZTDs from JPL with a mean bias of -0.5 mm and a mean standard deviation of 3.0 mm.

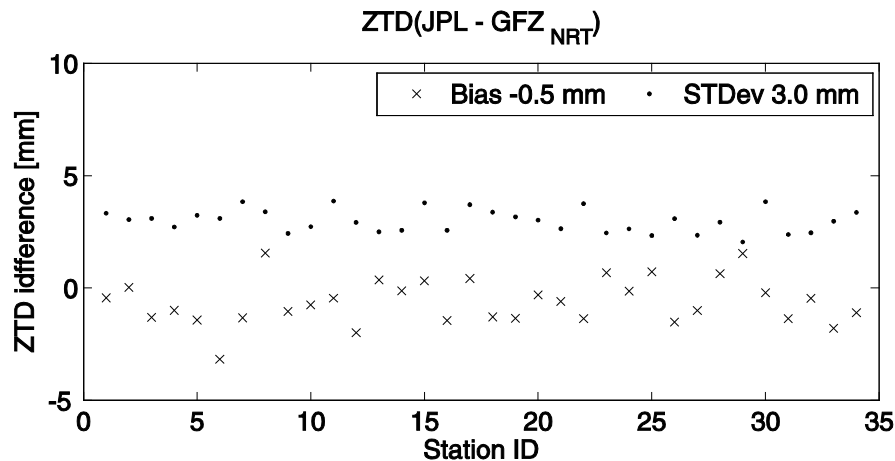


Figure 2.11: Statistics of the ZTD differences between JPL and GFZ NRT products for 34 IGS stations for one week of data: the crosses indicate the bias; the dots are standard deviations.

2.6 Introduction to GPS meteorology and summary of recent results

GPS meteorology is a remote sensing technology for the monitoring of atmospheric conditions using GPS data. According to the location of the GPS receivers, there are two main methods: ground-based and space-based GPS meteorology.

2.6.1 Ground-based GPS meteorology

For the ground-based GPS meteorology, GPS observation networks distributed on the surface of the Earth receive the signals from the GPS satellites. The water vapor distribution over the stations can be estimated from the GPS signal delays. Compared with the conventional observations, e.g., water vapor radiometers, balloons and remote-sensing satellites, ground-based GPS observations offer IWV data of high temporal resolution and high-accuracy in all weather conditions.

The tropospheric delay

The troposphere is the lowest part of the atmosphere. As the GPS radio signals propagate through the troposphere, the speed of propagation of GPS signals is slower in

the troposphere than in vacuum, and the signal path is bent due to the gradient in the index of refraction of the atmosphere. The excess path length is the troposphere delay, named Slant Total Delay (STD). Unlike the ionosphere, the troposphere is electrically neutral and non-dispersive for GPS frequencies; therefore, the troposphere delay cannot be cancelled using DF combinations.

The STD can be defined as:

$$STD = \int_S n ds - \int_{S_0} ds'. \quad (2.10)$$

Here n is the atmospheric refraction index along the path S ; S is the real bended signal path through the atmosphere, and S_0 is the geometrical straight-line path through the atmosphere (see **Figure 2.12**). Since the index of refraction n is numerically close to unity, it is usually expressed by the refractivity

$$N = (n - 1) \cdot 10^6. \quad (2.11)$$

The STD can be written as:

$$STD = 10^{-6} \int_S N ds + \left(\int_S ds - \int_{S_0} ds' \right). \quad (2.12)$$

The first term on the right side corresponds to the microwave delay and the second term relates the curvature between S and S_0 . N is related to the local pressure, temperature, and water vapor content:

$$N = N_h + N_{wet} = k_1 \frac{P}{T} + \left(k_2' \frac{1}{T} + k_3 \frac{1}{T^2} \right) P_v, \quad (2.13)$$

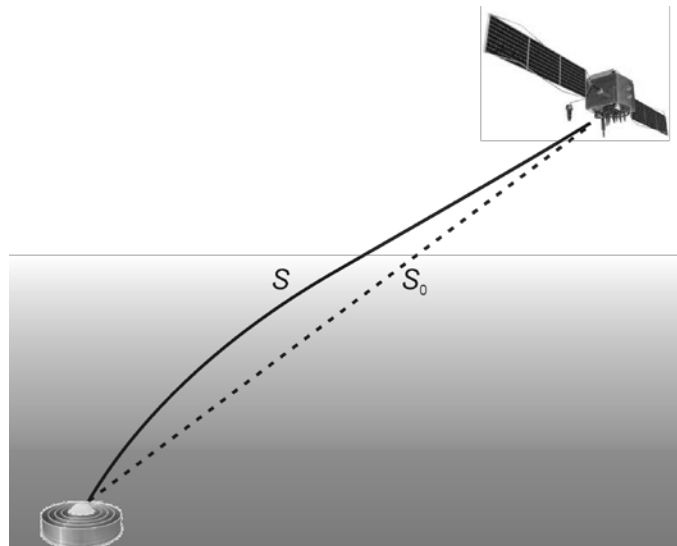


Figure 2.12: GPS signal geometry: GPS signal path (solid line S) in the atmosphere. The STD is the integrated signal delay as compared to the undisturbed signal propagation through vacuum (dotted line S_0).

where P is the hydrostatic pressure of the air in mbar, P_v is the partial pressure of water vapor in mbar, and T is the temperature in K. The empirically determined constants $k_1 = 77.6 \text{ K mbar}^{-1}$, $k_2' = 22.1 \text{ K mbar}^{-1}$ and $k_3 = 3.73 \cdot 10^5 \text{ K}^2 \text{ mbar}^{-1}$ can be found in

Bevis et al. (1994); N_h represents the refractivity of an ideal gas in hydrostatic equilibrium and N_{wet} is a function of the partial water vapor pressure and temperature:

$$N_h = k_1 \frac{P}{T},$$

$$N_{wet} = k_2 \frac{P_v}{T} + k_3 \frac{P_v}{T^2},$$
(2.14)

where the hydrostatic refractivity N_h depends on the hydrostatic pressure and temperature, which is relatively stable in space and time; N_{wet} undergoes strong variations with height, time, and location and is very difficult to predict. In terms of N_h and N_{wet} the slant path delay can be written as:

$$STD = \left[10^{-6} \int_s N_h ds + \left(\int_s ds - \int_{s_0} ds' \right) \right] + 10^{-6} \int_s N_{wet} ds.$$
(2.15)

The two terms on the right hand side are referred to as the Slant Hydrostatic Delay (include geometric delay due to signal path curvature) (SHD) and the Slant Wet Delay (SWD). Eq. (2.15) can be simplified to contain only the integral of refractivity.

$$STD = SHD + SWD.$$
(2.16)

The SWD is highly variable in space and time and can contribute up to 10% of the STD. To separate the SWD from the STD, the SHD must be estimated from the surface pressure in advance.

The mapping function and ZTD

For a short period of time (from several minutes to hours) the STDs of one station can be modeled by one ZTD parameter using a mapping function.

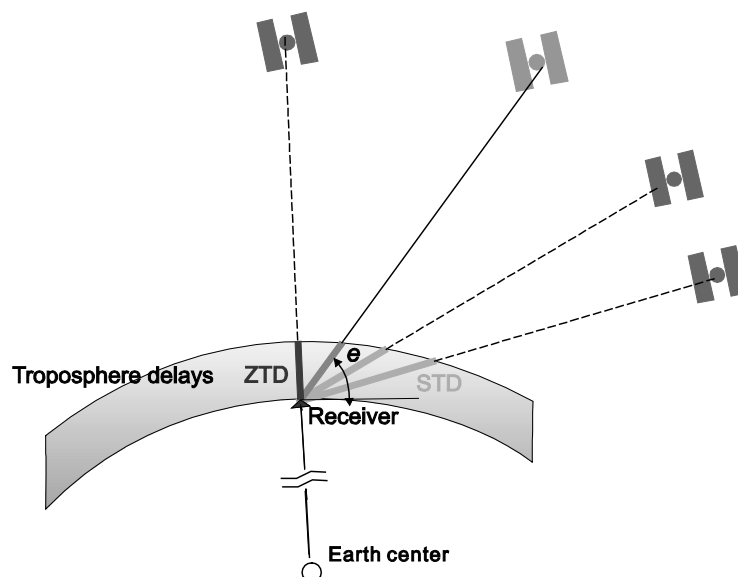


Figure 2.13: Illustration of the ZTD and STD geometry.

As shown in **Figure 2.13**, the ZTD is a spatial average of all STDs taken over a period of time. Thus the ZTD is an average of both space and time. With a decreasing elevation angle of a satellite, the length of the path through the neutral atmosphere increases. The

STDs are scaled to their equivalent zenith delay according to:

$$ZTD = ZHD + ZWD = \frac{SHD}{M_h(e)} + \frac{SWD}{M_w(e)}. \quad (2.17)$$

Like the STD, the ZTD is further divided into two terms, one that represents the delay due to hydrostatic gases (ZHD) and another due to the partial pressure of water vapor (ZWD). Base on the approximation by Saastamoinen (1972), the ZHD can be expressed by (Davis et al., 1985):

$$ZHD(P_s, \phi, H) = \frac{0.0022768P_s}{1 - 0.00266 \cos(2\phi) - 0.00028H}, \quad (2.18)$$

where P_s is the surface pressure, ϕ is the station latitude, and H is the station altitude. The ZWD can be separated from the ZTD using the ZHD.

The terms $M_h(e)$ and $M_w(e)$ are the hydrostatic mapping function and the wet mapping function, respectively. If the atmosphere above the GPS antenna is homogeneous in azimuth angle, the STDs can be related to the ZTD by mapping functions. Prominent examples have been formulated by Davis et al. (1985), Niell (1996) and Boehm (2006). Using a three term continued fraction of $1/\sin(e)$ the mapping function is modeled with sufficient accuracy for elevations down to 3° (Mendes, 1999). The hydrostatic $M_h(e)$ and wet $M_w(e)$ mapping functions are similar but not identical.

$$M_h(e) = \frac{1 + \frac{a_h}{1 + \frac{b_h}{1 + c_h}}}{\sin(e) + \frac{a_h}{\sin(e) + \frac{b_h}{\sin(e) + c_h}}} + h \cdot \left(\frac{1}{\sin(e)} - \frac{1 + \frac{a_{hc}}{1 + \frac{b_{hc}}{1 + c_{hc}}}}{\sin(e) + \frac{a_{hc}}{\sin(e) + \frac{b_{hc}}{\sin(e) + c_{hc}}}} \right), \quad (2.19)$$

$$M_w(e) = \frac{1 + \frac{a_w}{1 + \frac{b_w}{1 + c_w}}}{\sin(e) + \frac{a_w}{\sin(e) + \frac{b_w}{\sin(e) + c_w}}}. \quad (2.20)$$

The wet mapping function is slightly larger and much more variable than the hydrostatic mapping function. The difference between the two mapping functions is related to the scale heights of water vapor (2-3 km) and the neutral atmosphere (closer to 8 km). At 10° elevation angle, the hydrostatic mapping function has values between five and six. At 5° elevation it is approximately 10. In the EPOS software the Global Mapping Function (Boehm et al., 2006) is used.

The ZWD is correlated with the Integrated Water Vapor (IWV) and can be obtained with the method suggested by Bevis et al. (1994):

$$IWV = \Pi(T_m)ZWD, \quad (2.21)$$

where the conversion factor $\Pi(T_m)$ depends on the mean weighted temperature of the atmosphere and can approximately be calculated from surface meteorological measurements (Bevis et al., 1992).

$$\Pi(T_m) = \frac{10^6}{R_v \left(k'_2 + \frac{k_3}{T_m} \right)},$$

with (2.22)

$$T_m = \frac{\int \frac{P_v}{T} dz}{\int \frac{P_v}{T^2} dz},$$

where $R_v = 461.495 \text{ J/(K} \cdot \text{kg)}$ is the water vapor gas constant; and T is the temperature at a given height. Bevis et al. (1992) investigated the correlation between the surface temperature and the mean temperature based on radiosonde observations in North America over 2 years. A linear correlation between T_m and T was found:

$$T_m = 70.2 + 0.72T, \quad (2.23)$$

with a RMS of 4.7 K.

Initially motivated by atmosphere corrections for precise positioning applications GFZ started GPS atmosphere sounding in 1996 and provides ZTDs as well as the IWV with the same temporal resolution of one hour since 1996. An improved temporal resolution of 15 minutes is used since 2004. The IWV has an accuracy of 1–2 kg m^{-2} and a precision of 1 kg m^{-2} (see Gendt et al., 2001, 2004).

2.6.2 Space-based GPS radio occultation

The space-based GPS radio occultation (RO) technique uses radio signal delays caused by the atmosphere, when the radio signal travels from a GPS satellite to a GPS receiver on board a LEO satellite (**Figure 2.14**). The LEO satellite observes radio signals from GPS satellites rising or setting behind the Earth. The bending angle of the signal path is a key measurement of GPS RO and is induced by ionospheric and neutral atmospheric refraction. With the RO technique profiles of refractivity, temperature, pressure, and water vapor in the neutral atmosphere and profiles of the electron density in the ionosphere can be obtained. In the GPS meteorology (GPS/MET) experiment on the Micro Lab-1 satellite launched in April 1995, the temperature profiles with a vertical resolution of approximately 1 km showed an accuracy of better than 0.5 °C at the tropopause (Ware et al., 1996). It has been demonstrated that the GPS/MET accuracy is comparable to that of the traditional atmosphere sensing techniques (e.g., Kursinski and Hajj, 2001). For more details on the RO technique please refer to Kursinski et al. (1996, 1997) or Wickert (2002).

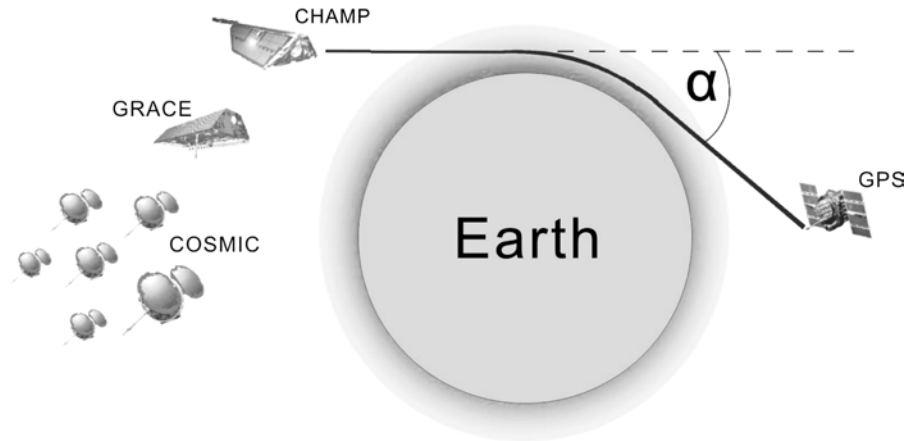


Figure 2.14: GPS radio occultation (RO) with the LEO satellites CHAMP, GRACE and COSMIC (Arras, 2010); a key measure of GPS RO is the bending angle α .

2.7 The SAPOS network and densification with single frequency GPS receivers

The SAPOS network

SAPOS stands for Satellite Positioning Service, and is organized by the German State Surveying Agencies (AdV). The SAPOS stations provide GPS data to support high-precision GNSS measurements. In order to cover all parts of Germany, a network of about 250 reference stations with inter-station distances of about 40 km to 70 km was set up (**Figure 2.15**). The hardware and software at the reference stations comply with specific standards fixed by the AdV and are updated within the framework of SAPOS quality assurance measures (www.sapos.de).

SAPOS provides differential GNSS correction data for network Real Time Kinematics (RTK) or for relative positioning in post-processing, which can be applied to

- positioning and navigation at land and water,
- effective and precise surveying for geodetic applications, cadastre and engineering surveying and
- acquisition of Geographic Information System (GIS) data.

For the reference stations the long-term stability is important and only high-quality geodetic GNSS DF receivers and antennas are used. Sites and antennas are also selected to provide maximum sky coverage without obstruction and to avoid external radio interference and multipath effects on satellite signals. By using appropriately calibrated choke ring antennas, possible multipath effects are further counteracted. Coordinates of the reference stations are determined with high-precision (www.sapos.de).

The positions of the SAPOS reference station antennas are checked regularly (four times a year) for any displacement in relation to selected stations of the German GPS reference network (GREF), the European references network (EUREF, see www.euref.org) and the IGS network (<http://igs.cb.jpl.nasa.gov/>).

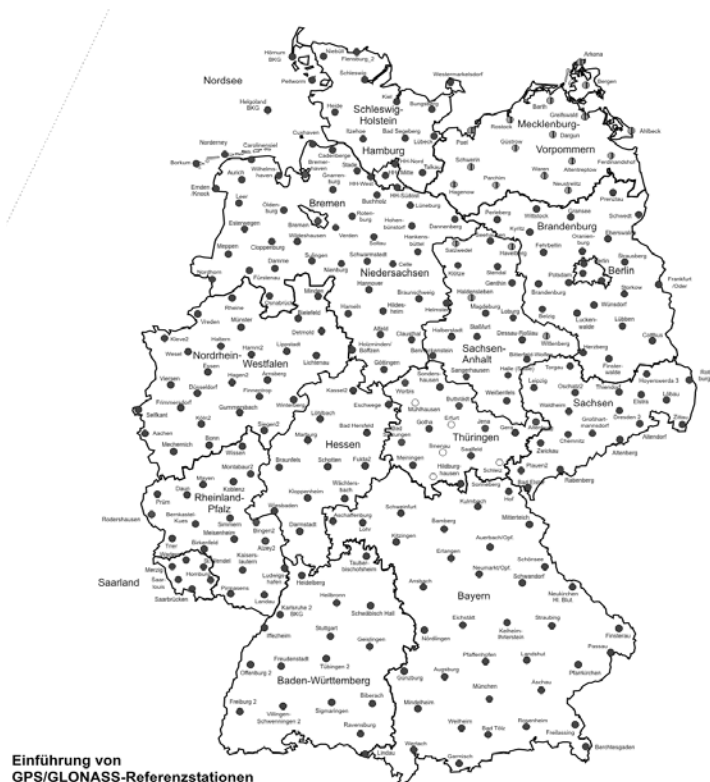


Figure 2.15: The German SAPOS reference stations (status March 2011, www.sapos.de).

Densification for water vapor monitoring

In 2001 a national-wide GNSS network consisting of 29 stations became fully operational in Switzerland. The inter-station distances within the Automated GNSS Network for Switzerland (AGNES) are between 40 and 80 km, and attempts were made to interpolate the ZTD observations between the stations in order to obtain spatially resolved ZTD and IWV data for weather forecasts. It turned out that an interpolation accuracy of about 8 mm for the ZTDs could be achieved for all regions in Switzerland. However, in summer and during rapid weather change the accuracy is reduced. The quality of the interpolated ZTD and IWV data was not sufficient for numerical weather prediction applications, especially in summer and during severe weather events.

The ZTD estimates at the GNSS station were of good quality but the spatial resolution of the AGNES network was not sufficient to improve the humidity field within the weather model satisfactorily. Therefore a densified GNSS network would be required, e.g., supplemented with SF GPS receivers. Inter-station distances below ~ 20 km would be desirable for water vapor monitoring (Bender et al., 2009; Braun et al., 1999).

The results from the AGNES network can be applied to the German SAPOS network and a network consisting of low-cost SF GPS receivers and the geodetic DF receivers from SAPOS will be proposed. Such a design would be significantly cheaper than an extended DF network and provide ZTD/IWV data of sufficient quality for meteorological applications.

As shown in the introduction, the nationwide gamma dose rate (ODL) network of the BfS has the potential to be used for the densification of the existing SAPOS network in Germany. The SF GPS antenna could be installed on top of an ODL probe with good satellite visibility. With access to a telephone mainline and a 230V power supply the received data can continuously be sent to a data centre.

3 Single frequency GPS receivers selection

For many meteorological applications, such as short-term numerical forecasting and the reconstruction of the spatial temporal distribution of the tropospheric water vapor, GPS derived tropospheric information of high spatial and temporal resolution is required. However, the deployment of such dense high-quality GPS networks requires substantial financial and infrastructure resources. To detect the water vapor distribution with resolutions of kilometer scale in horizontal and sub-kilometer scale in vertical, developing of a new method of collecting data economically is required. Since a SF GPS station is almost as accurate and reliable as a DF station, such SF GPS stations can be used (Braun et al., 1999; Rizos et al., 2000). The components of the system are described in this chapter.

3.1 Overview on single frequency GPS receivers and hardware selection

At present there are two generic types of GPS receivers on the market: the SF and DF receivers. SF GPS receivers are less expensive than DF receivers, and many SF solutions exhibit equivalent accuracy as those obtained from DF observations. Several authors, like e.g., Rizos et al. (2000), Braun et al. (1999, 2004), Janssen et al. (2002) and Rocken et al. (2000) investigated the potential of using low-cost SF receivers for high-accuracy positioning and for geodetic applications. They found a differential positioning accuracy ranging from a few millimeters to several meters using SF receivers of different manufacturers. The use of a low-cost SF GPS receiver to obtain accurate results is therefore a major challenge.

3.1.1 Single frequency GPS receivers

Three SF GPS receiver were tested and validated by Deng (2008). The specifications of the three receivers are listed in **Table 3.1**.

During the test the GARMIN GPS 17-HVS had a clock drift of about 77 milliseconds per hour. For the other two receivers no conspicuous offset and drift of the receiver clock was detected. To check the quality of the phase observations, 1-Hz GPS observations from the three receivers were used. The noise of the single difference between satellites was checked. The quality of the GPS carrier phase measurements of the THALES (AC 12) is equivalent to DF geodetic GPS receivers. The single differences noise of the THALES AC12 receiver is about 0.8 mm, which is smaller than that of the NovAtel SMART antenna (about 1.6 mm). Both of the receivers are suitable to provide carrier phase observations. The products have different prices: the NOVATEL SMART antenna with integrated GPS receiver SUPERSTAR II, costs about 600 Euros; the THALES receiver costs about 700 Euros without antenna. In consideration of the quality and price the NovAtel SMART antenna was selected for the GPS meteorology experiments.




SF receivers			
Type	GARMIN GPS 17-HVS	NovAtel SMART	THALES AC12
Integrated antenna	Yes	Yes	No
Price (2008)	~200 €	~600 €	~700 €
Observation	12 channels C/A code & L1 phase	12 channels C/A code & L1 phase	12 channels C/A code & L1 phase
Carrier phase accuracy (RMS)	Not available	1 cm	3 mm
Data rate	Max. 1 Hz	Max. 10 Hz	Max. 1 Hz
Power consumption	Not available	1.4 W (typical)	Not available

Table 3.1: Specifications of three SF receiver types (Deng, 2008; Glabsch et al., 2009).

Unexpectedly the company NovAtel stopped to produce NovAtel SMART antennas. A new type, named NovAtel SMART-V1 antenna is now available. The specifications of the NovAtel SMART-V1 antenna are introduced below.

3.1.2 NovAtel (SMART-V1 antenna)

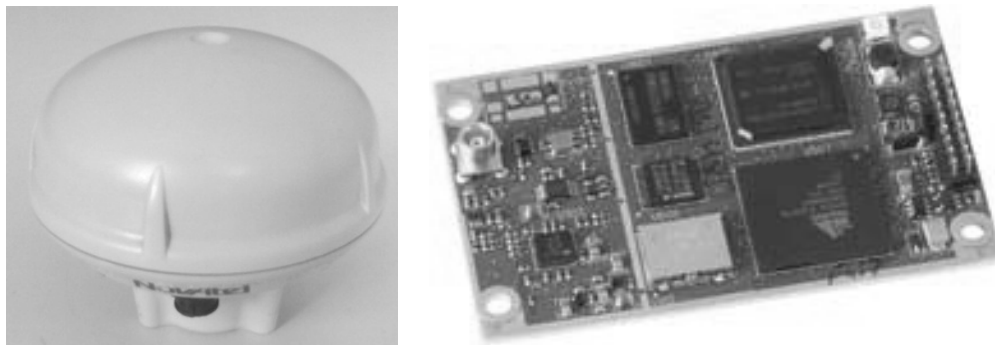


Figure 3.1: NovAtel SMART-V1 antenna (left panel) and the integrated receiver OEMV-1 (right panel).

The SMART-V1 antenna provides an integrated L1 GPS receiver with 14 channels for L1 GPS code and phase tracking (**Figure 3.1**). To check the quality of L1 data from the SF GPS NovAtel SMART-V1 receiver a small GPS network was set up at GFZ. The network consisted of 2 SF stations and 2 DF stations. **Figure 3.2** shows the map of the network. POTS and POTM (**Figure 3.3**) are DF stations; GP00 and GP20 are SF stations (**Figure 3.4**). A list of receiver and antenna types of the test stations is given in **Table 3.3**. Because the distances of the baselines are extremely short, orbit errors and

the atmospheric delays will cancel when processing the baseline data, but the multipath errors will not be eliminated. However, the performance of the full SF/DF GPS antennas and receivers can be addressed.

GNSS system	GPS
Number of channels	14 L1 GPS
Receiver card	NovAtel's OEMV-1
Measurement precision (RMS)	C/A code: 18 cm; phase 1.5 mm
Sampling rate	Max. 20 Hz
Input voltage	9 – 24 VDC
Power consumption	1.2 W (typical)
Interface	RS-232 / RS-422 / USB

Table 3.2: NovAtel SMART-V1 antenna specifications (NovAtel, 2008).

For the processing of the test network data the broadcast messages are used and the absolute antenna phase center variation (PCV) corrections are applied. The elevation cut-off angle for the data processing is 7 degrees. The data sampling interval is 30 seconds.

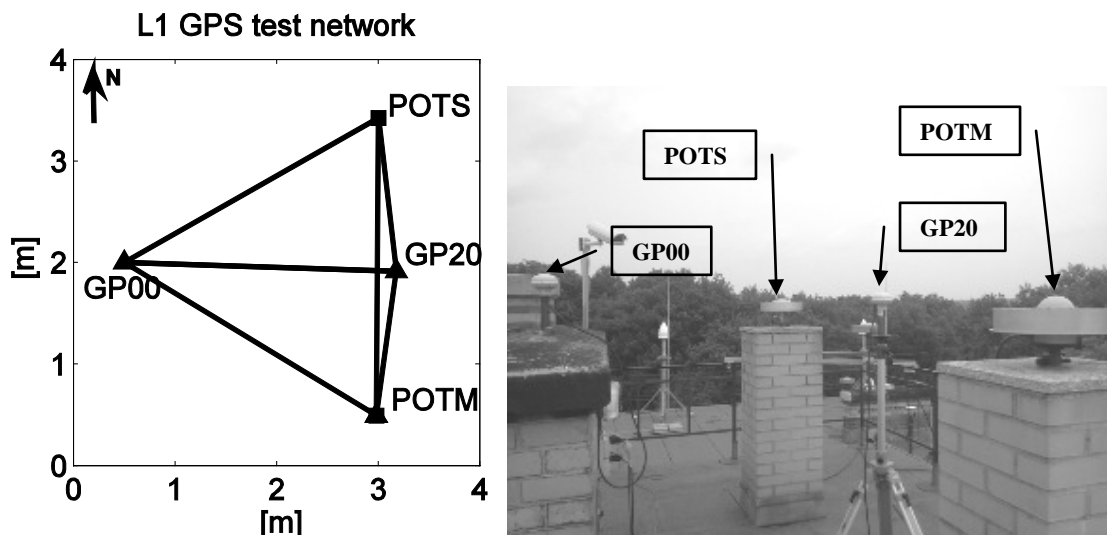


Figure 3.2: GPS test network on the roof: the two triangles denote SF stations (GP00 and GP20); the squares denote two DF stations (POTS and POTM).



Figure 3.3: DF station POTS (left) and POTM (right) of the test network equipped with choke ring antennas.

The test GPS network was set up on the roof of the geodesy section at the GFZ. POTS is an IGS station, and POTM is a permanent station of GFZ.



Figure 3.4: SF station GP00 (left) and GP20 (right) of the test network.

name	Receiver type	Antenna type
GP00	OEMV-1	NOVATEL SMART-V1
GP20	OEMV-1	NOVATEL SMART-V1
POTS	JAVAD TRE_G3TH DETAL	JAV_RINGANT_G3T NONE
POTM	AOA BENCHMARK ACT	AOAD/M_T NONE

Table 3.3: List of receiver and antenna types for the test stations.

The two SF stations are equipped with low-cost integrated L1-only GPS receivers of the type NovAtel SMART-V1. The DF stations have geodetic equipments with choke-ring antennas. The SNR can be used as a parameter for the precision of the pseudorange and carrier-phase observations. From the RINEX file SNR values for all epochs can be extracted. However, the SNR values from different manufacturers are not directly comparable as each manufacturer defines different noise characteristics. In the short baseline test all three receiver types report SNR as Carrier to Noise Power (C/N_0) expressed as a ratio in units of dB-Hz.

Figure 3.5 and **Figure 3.6** show the C/N_0 collected using the DF GPS receivers. **Figure 3.7** plots the C/N_0 collected with the low-cost SF receiver OEMV-1.

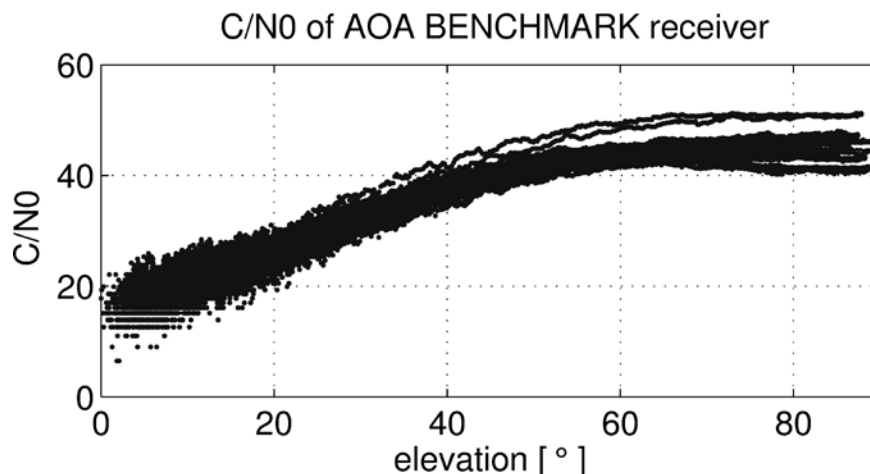


Figure 3.5: C/N_0 values in dB-Hz from the DF GPS receiver AOA BENCHMARK (station POTM).

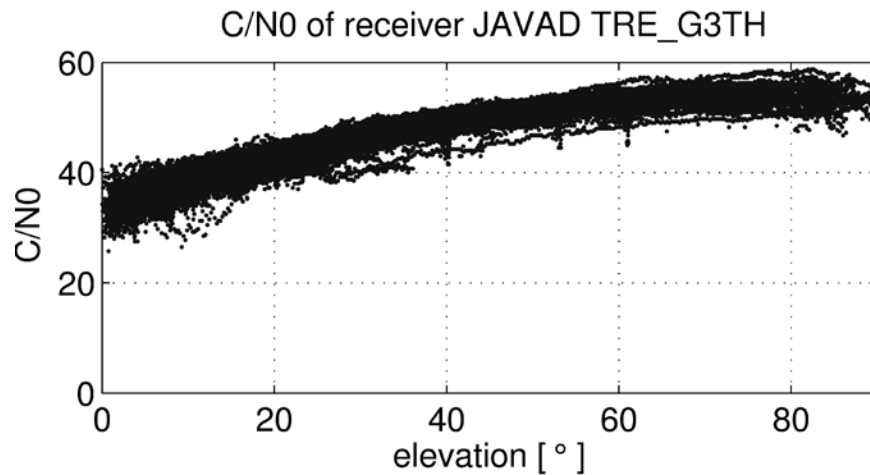


Figure 3.6: C/N_0 values in dB-Hz from the DF GPS receiver JAVAD TRE_G3TH (station POTS).

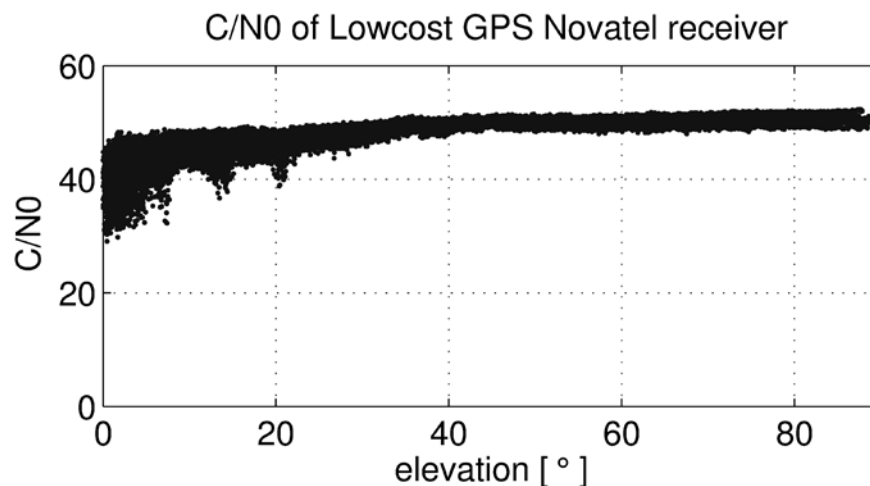


Figure 3.7: C/N_0 values in dB-Hz from the SF GPS receiver OEMV1 (station GP00).

The cut-off angle of the four test stations was 0 degree. The C/N_0 of the observation from the receiver AOA BENCHMARK decreased rapidly from about 45 dB-Hz near zenith to about 15 dB-Hz at lower elevations. The other DF receiver JAVAD TRE_G3TH showed a relatively slow variation with elevation. The C/N_0 from the SF receiver varies from about 50 dB-Hz to 30 dB-Hz. The C/N_0 between elevations 40 to 90 degrees is almost constant. The observations of the SF receiver could have suffered from an increased noise level, more frequent cycle slips and multi-path effects at low elevation.

Results of the test

6 baselines were formed from the 4 test stations. Each baseline was processed using daily data of the day of year (DOY) 130, 131 and 132 in the year 2011 with ambiguity-fixing. Their repeatability in the three days is better than 1 mm (Table 3.4). The Trimble commercial GPS software Ashtech Solutions 2.60 was used to process the L1 baselines, the standard deviation of the results can not be given better than 1 mm. This indicates that the quality of the low-cost SF data is comparable to that of normal geodetic equipment for short baseline determination.

Because the SF station GP00 received only 16 hours of data on DOY 130, the results of the baselines GP00-POTM and POTS-GP00 have 1 mm variation compared to the results of the other two days. The residuals of the 6 baselines on DOY 132 are given in **Figure 3.8**, **Figure 3.9** and **Figure 3.10**, respectively. The main intension is to show the relation between the noise level and the receiver types used.

Baseline	DOY	Length [m]	Std [mm]	North [m]	Std [mm]	East [m]	Std [mm]	Up [m]	Std [mm]
GP00-GP20	130	1,642	1	0.086	0	-1.638	0	-0.091	1
GP00-GP20	131	1,642	1	0.086	1	-1.638	0	-0.091	0
GP00-GP20	132	1,642	1	0.086	0	-1.638	0	-0.091	1
GP00-POTM	130	2,147	1	1.506	1	-1.517	1	-0.206	1
GP00-POTM	131	2,148	1	1.506	0	-1.518	0	-0.205	1
GP00-POTM	132	2,148	1	1.506	0	-1.518	0	-0.205	1
GP20-POTM	130	1,431	0	1.421	0	0.120	0	-0.115	0
GP20-POTM	131	1,431	0	1.421	0	0.120	0	-0.115	0
GP20-POTM	132	1,431	1	1.421	1	0.120	0	-0.115	0
POTS-GP00	130	2,103	1	1.423	1	1.530	1	0.230	1
POTS-GP00	131	2,102	1	1.423	1	1.531	0	0.229	0
POTS-GP00	132	2,102	1	1.423	0	1.531	0	0.229	0
POTS-GP20	130	1,518	0	1.508	0	-0.107	0	0.139	0
POTS-GP20	131	1,518	0	1.508	0	-0.107	0	0.139	0
POTS-GP20	132	1,518	0	1.508	0	-0.107	0	0.139	0
POTS-POTM	130	2,929	1	2.930	0	0.013	0	0.024	0
POTS-POTM	131	2,929	0	2.930	0	0.013	0	0.024	0
POTS-POTM	132	2,929	0	2.930	0	0.013	0	0.024	0

Table 3.4: Results of the 6 baselines for the three days; the bold numbers are the components of the baselines, which are 1 mm different from the results of the other two days.

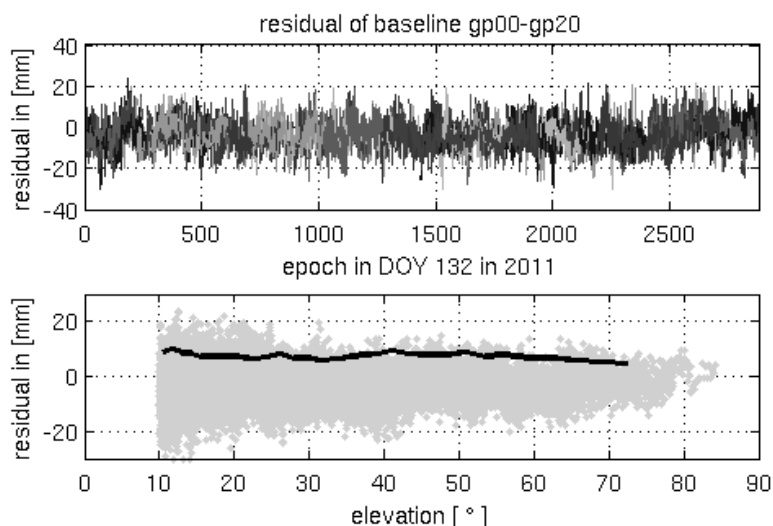


Figure 3.8: DD residuals of the L1 baseline of the two SF stations GP00 and GP20 for DOY 132 in 2011 (top panel) each gray value level indicates a different satellite; the 600-point running RMS is plotted as black line (bottom panel).

The residuals of the SF baseline are decreasing with the increasing elevation angles (**Figure 3.8**). The 600-point running RMS at an elevation of 72° is about 4.7 mm, which

indicates that the noise of the low-cost SF equipments is larger than the noise of a typical geodetic GPS receiver (2 mm carrier phase accuracy). The residuals of the baseline GP20 - POTM are plotted in **Figure 3.9**. They are smaller than the residuals from the baseline GP20 - GP00.

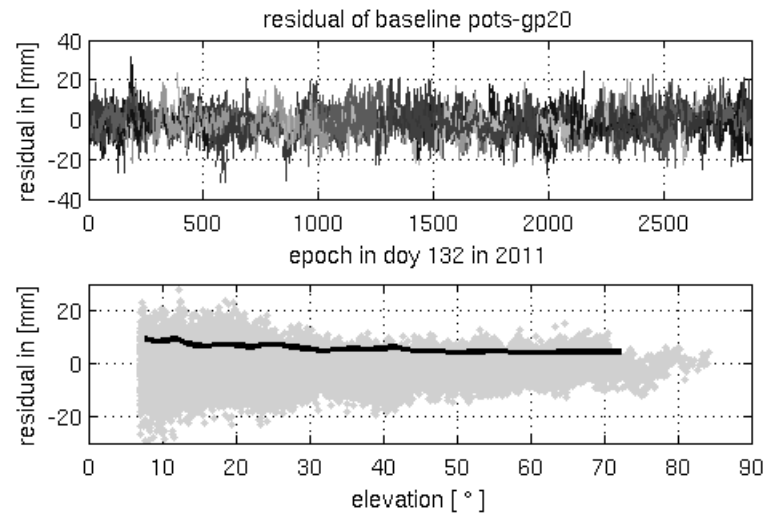


Figure 3.9: DD residuals of the L1 baseline of the SF station GP20 and the DF station POTM for DOY 132 in 2011 (top panel) each gray value level indicates a different satellite; the 600-point running RMS is plotted as black line (bottom panel)

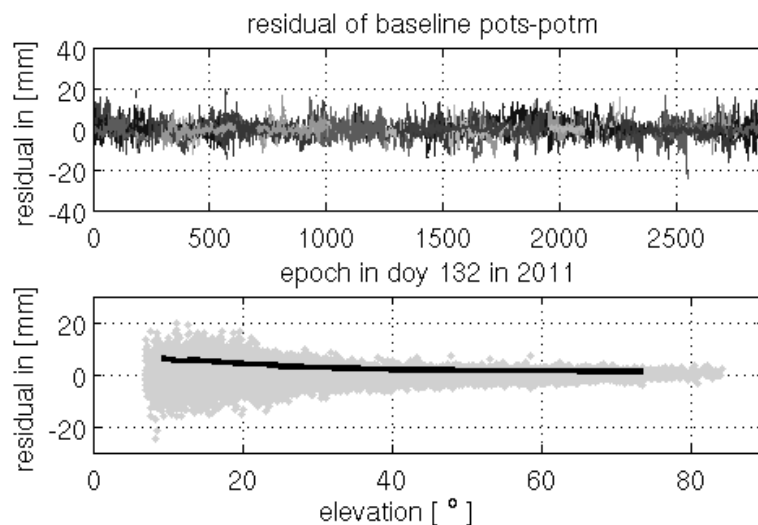


Figure 3.10: DD residuals of the L1 baseline of the DF stations POTM and POTS for DOY 132 in 2011 (top panel) each gray value level indicates a different satellite; the 600-point running RMS is plotted as black line (bottom panel)

In **Figure 3.10** the residuals of the baseline POTS — POTM decrease with the elevation angle more significantly than those from other baselines. The residuals of the baseline GP00-GP20 are the largest among the 6 baselines. This indicates that the GPS data from the low-cost SF receivers include more noise than the data from the geodetic receivers.

Figure 3.11 shows that the RMS of the SF baseline GP00-GP20 is about 5 mm larger than that of the DF baseline POTS-POTM. In order to estimate the impact on the ZTD, the ZTD covariance was analyzed. In EPOS the typical ZTD variation of the covariance matrix is about 0.1 to 0.2, the 5 mm RMS of the SF observations leads to a 0.5 – 1 mm

error in ZTD parameters, which can be neglected for meteorological applications. The short baseline tests confirm that the carrier phase observations output from the NovAtel receiver is of sufficient quality for accurate tropospheric parameter estimation.

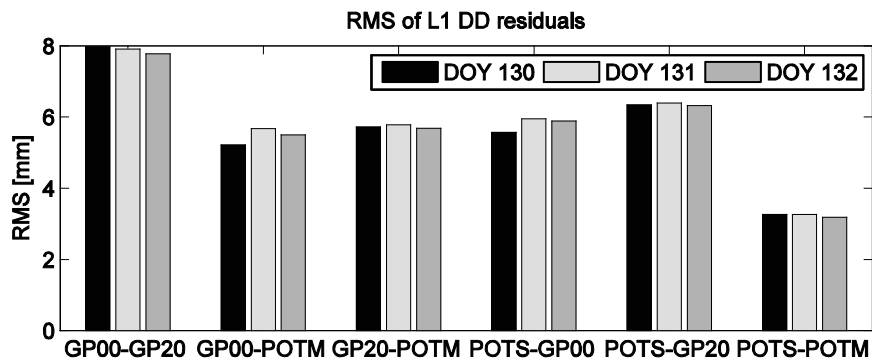


Figure 3.11: RMS of the L1 DD residuals from the six baselines for three days.

4 Precise processing of GPS single frequency data

The ionosphere is a shell of free electrons and electrically charged atoms and molecules, which surrounds the Earth, extending from a height of about 50 km to more than 1000 km above the Earth's surface. The charged particles in the ionosphere have a major effect on GPS signal propagation. The resulting range error for GPS frequencies can vary from less than 1 m to more than 100 m (Seeber, 2003). Since the ionospheric delay is frequency-dependent, DF GPS receivers are able to remove this ionospheric effect by using a linear combination of measurements on both frequencies. To retrieve precise tropospheric delays from the SF data, the ionospheric delay must be corrected in advance. There are already several different methods to solve this problem. In this chapter these methods are summarized. After discussing the existing methods a new ionospheric correction model is developed and the details of the strategy are presented.

4.1 Correction of ionospheric refraction for single frequency positioning

The ionospheric delay depends on the signal frequency and is proportional to the total electron content along the signal path. Usually, it can be removed by forming the linear combination of DF observations. Over short baselines, for example, up to a few kilometers, the ionospheric delay is cancelled or largely reduced in the differenced observation between stations because the transmitting paths of the signals are very close to each other (Janssen and Rizos, 2002). However, for baselines longer than 10 km or PPP using SF observations, an ionospheric correction is required, as the delay cannot be cancelled with the above strategies. In this part several models to correct ionospheric delays will be introduced and discussed.

- **Vertical total electron content model**

Conventionally, ionospheric delays on GPS observations can be reduced by using ionospheric delay models for SF applications (Teunissen and Kleusberg, 1998). Most of the available models assume a single ionospheric layer. The vertical total electron content (VTEC) of the ionosphere is represented by a thin shell with an altitude between 250 and 450 km above the Earth's surface. To get the total electron content (TEC) along the path from the GPS satellite to a receiver, the VTEC is mapped to the directions of the observations (**Figure 4.1**).

In the Klobuchar ionosphere model a cosine curve fits the average diurnal variation of the ionosphere. This model assumes that the maximum daily TEC value occurs at about 14:00 local time. Usually the ionospheric error of the SF data is corrected with the Klobuchar model. The parameters of the model are broadcast through the navigation message. However, the Klobuchar model can only compensate 50-60% of the total ionosphere effect (Klobuchar, 1987).

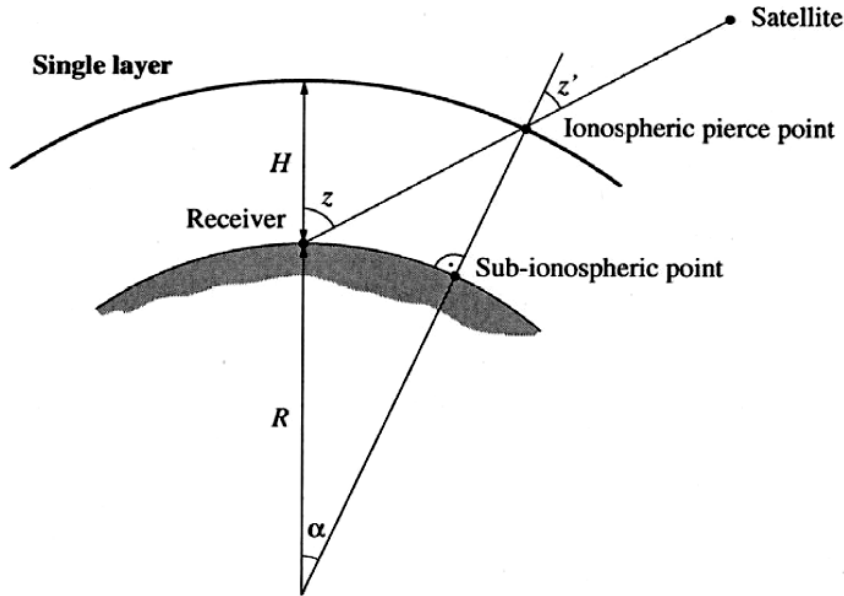


Figure 4.1: Geometry of the ionospheric single layer model (Schaer, 1999).

It is possible to compute the slant ionospheric corrections from a 2 or 3-dimensional ionosphere map generated by some IGS processing centers (Khattatov et al., 2004; Schaer, 1999). Sekido et al. (2003) showed that the total accuracy of a global ionosphere map from the Centre of Orbit Determination in Europe (CODE) is about 3.7 – 3.9 Total Electron Content Unit (TECU) (1 TECU corresponds to 10^{16} electro/m² and induces a delay of 0.163 m on L_1 signals).

Since the ionosphere is a shell stretching from a height of about 50 km to more than 1000 km, the ionosphere models described so far do not capture small-scale and high-frequency ionospheric disturbances. For precise applications of SF receivers more accurate ionospheric correction models are required.

- **Ionospheric correction with double difference residuals**

Ionospheric corrections can be retrieved from double difference results in different ways. Janssen and Rizos (2005) demonstrated an approach for deformation monitoring using SF and DF mixed-mode GPS network. The ideal configuration of a mixed-mode GPS network is given in **Figure 4.2**, where the triangles are reference stations equipped with DF GPS receiver, and the dots denote monitoring stations with SF receivers.

In a first step the data from three reference stations are processed using the double difference method. The ambiguities of the double difference observations can be resolved. With the ambiguity solution the ionospheric correction $\nabla\Delta I_{ij}^{kl}(t)$ of the double difference observations can be written:

$$\nabla\Delta I_{i,j}^{k,l}(t) = \left(\nabla\Delta L_{1,i,j}^{k,l}(t) - \nabla\Delta N_{1,i,j}^{k,l} \right) - \left(\nabla\Delta L_{2,i,j}^{k,l}(t) - \nabla\Delta N_{2,i,j}^{k,l} \right), \quad (4.1)$$

where the subscripts i and j denote the i_{th} and j_{th} receiver, respectively, the superscript k and l denote the k_{th} and l_{th} satellites and t is the epoch index. From the three reference stations two independent ionospheric corrections, e.g., $\nabla\Delta I_{1,3}^{k,l}(t)$ and $\nabla\Delta I_{2,3}^{k,l}(t)$, can be calculated. The ionospheric correction of the internal SF stations to the reference station

3 and the satellite pair k and l can then be interpolated linearly as (Janssen and Rizos, 2005):

$$\nabla\Delta I_{u,3}^{k,l}(t) = x_{u,3} \cdot a_N^{k,l}(t) + y_{u,3} \cdot a_E^{k,l}(t), \quad (4.2)$$

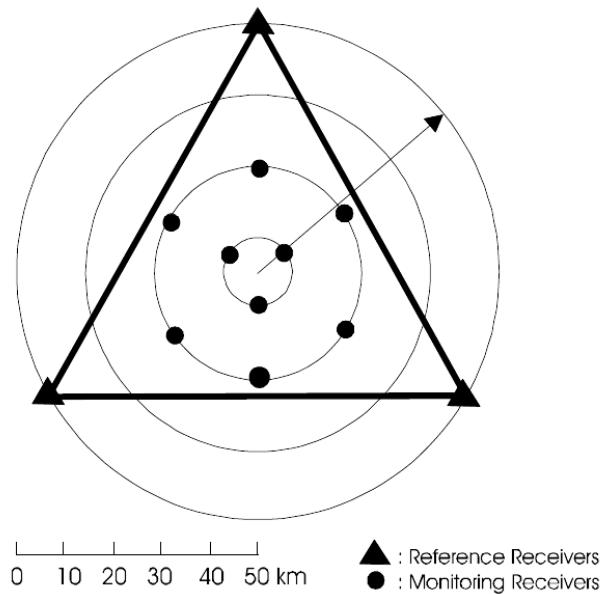


Figure 4.2: Deformation monitoring: Ideal configuration of a mixed-mode GPS network, adapted from (Janssen and Rizos, 2005).

where $a_N^{k,l}$ and $a_E^{k,l}$ are the north and east components of the ionospheric correction, which can be calculated from $\nabla\Delta I_{1,3}^{k,l}(t)$ and $\nabla\Delta I_{2,3}^{k,l}(t)$; u denotes the internal SF station; $x_{u,3}$ and $y_{u,3}$ are coordinates difference of the station u and the reference station 3 in a local plane coordinate system. With the ionospheric corrections $\nabla\Delta I_{u,3}^{k,l}(t)$ the double difference observations between the SF station u and the reference station 3 can be formed and used to solve the integer ambiguities. With the ionospheric corrections the repeatability of single frequency baselines in mid-latitude regions can be improved to a standard deviation less than 1 cm horizontally and 1.5 - 3 cm vertically for a single-epoch baseline solution. The standard deviations of the single-epoch baseline solution were reduced by 40-50 % as compared to the case with no ionospheric corrections. However, in the equatorial region a standard deviation of a few cm cannot be achieved (Janssen and Rizos, 2005).

Alternatively, the ionospheric correction $\nabla\Delta I_{i,j}^{k,l}(t)$ of the double difference observations can be converted to a distance-dependent ionospheric correction with weights (Han, 1997):

$$\sum_{i=1}^3 \alpha_i = 1, \quad \sum_{i=1}^3 \alpha_i \cdot (\mathbf{x}_u - \mathbf{x}_i) = 0, \quad \sum_{i=1}^3 \alpha_i^2 = \min, \quad (4.3)$$

where α_i are the weights, \mathbf{x}_u and \mathbf{x}_i the Gaussian plane coordinates of the SF station u and reference station i . Using the $\nabla\Delta I_{i,j}^{k,l}(t)$ vectors generated from the reference stations, the inner station baselines can be determined without using any reference

station observations. In practice, holding one reference site fixed, the baselines to the other two reference stations are processed and the $\nabla\Delta I_{i,j}^{k,l}(t)$ are obtained for both baselines.

Similar to the above approaches the high-resolution ionospheric modeling technique (called HiRIM) was developed by Rocken et al. (2000). Based on the baseline observation residuals from the surrounding grid of GPS sites spaced ~ 50 km, an imported primary ionospheric model is improved for individual satellites at each epoch.

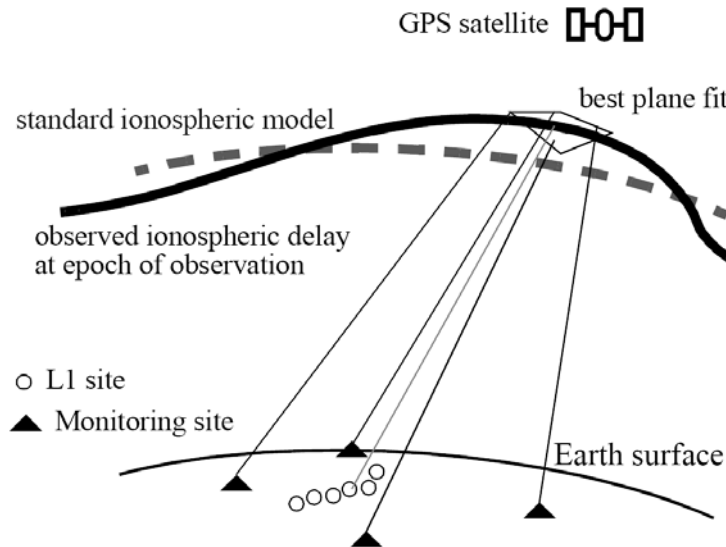


Figure 4.3: Geometry for the ionospheric single layer model HiRIM (adapted from Rocken et al., 2000).

In **Figure 4.3** the thick dashed line is standard and observed VTEC ionospheric delay; the thick solid line indicates real ionospheric delay; ionospheric delay values calculated from the monitoring sites are used to estimate the best plane fit. The ray path Ionospheric Pierce Point (IPP) of L1 sites (dotted line) with this plane is used to compute the ionospheric correction.

Similar to the approach of the deformation monitoring the monitoring sites (**Figure 4.2**) are processed with the double difference method and the ambiguities are solved. The double difference analysis provides post-fit double difference residuals and an ionospheric model that approximately describes TEC in the region of the GPS network. Next the double difference ionospheric delay residuals are converted to zero difference residuals. This double difference to zero difference conversion is based on two assumptions (Alber et al., 2000; Braun et al., 2001):

- When converting double difference residuals to single difference residuals the weighted sum of all single differences between stations observed from one baseline at one epoch is equal to zero,
- When converting single difference residuals to zero difference residuals the weighted sum of all zero differences observed from one satellite by the entire monitoring network at one epoch is equal to zero.

It has been demonstrate that the HiRIM-corrected L_1 solutions up to 30 km baseline are even more precise than ionosphere-free L_3 solutions.

- **Network RTK**

The single-baseline Real-time kinematic (RTK) was developed in the mid-1990s. With the RTK technique centimeter-level accuracy positioning can be achieved in real-time based on GPS measurements or more generally on GNSS measurements. One reference station and one rover station form a baseline. Since the distance-dependent biases such as orbit errors, and ionospheric and tropospheric signal refraction increase with the length of the baseline, moderate distances (up to 10 ~ 20 kilometers) are important to get fast and reliably carrier phase ambiguity fixing solutions. However, using area correction parameters from an array of surrounding reference stations highly accurate positioning is achievable over distances of several tens of kilometers, and the reference station spacing could generally be extended up to 70-100 km. This multi-reference technique is called Network RTK (Wanninger, 2006; Wübbena et al., 2001). The Network RTK reduces the investment of a RTK positioning service. One of the most prevalent Network RTK methodologies currently available is the Virtual Reference Station (VRS) (Landau et al., 2002).

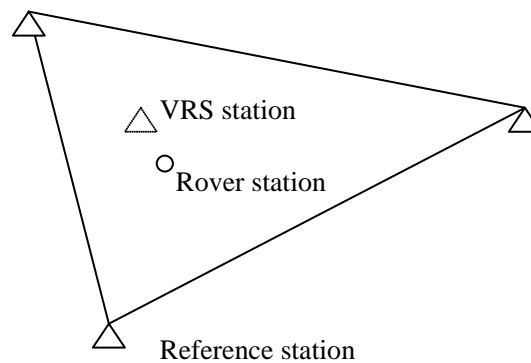


Figure 4.4: The data of the surrounding reference stations are processed by the control center in order to generate a Virtual Reference Station (VRS) close to the rover station.

To implement the VRS technique at least three reference stations are required (**Figure 4.4**). The reference stations are continuously connected to a control centre, and are processed in real-time with an ambiguity-fixed solution to generate regional area corrections across the network. The rover station must be capable of two-way communication. It sends its approximate position to the control centre. The control centre generates VRS observations according to the approximate position and sends them back to the rover station. The VRS is usually only a few meters away from the initial rover location. The rover uses the VRS observations just as if they had come from a single, real reference station and uses them for baseline positioning. Compared to RTK there is no requirement for an upgrade of the rover equipment software.

The surface correction parameterization (FKP) method uses a polynomial parameterization to describe the distance-dependent errors for any rover position in a certain region (**Figure 4.5**). The FKP describes the state space information in the area. Each reference station in the area is the center of a FKP model, and the horizontal gradients for the geometric and ionospheric signal components can be described with the FKP. As one part of the state space information the ionospheric delay can be represented by a plane or low-order surface. For a SF receiver the ionospheric delay can simply be interpolated in the plane.

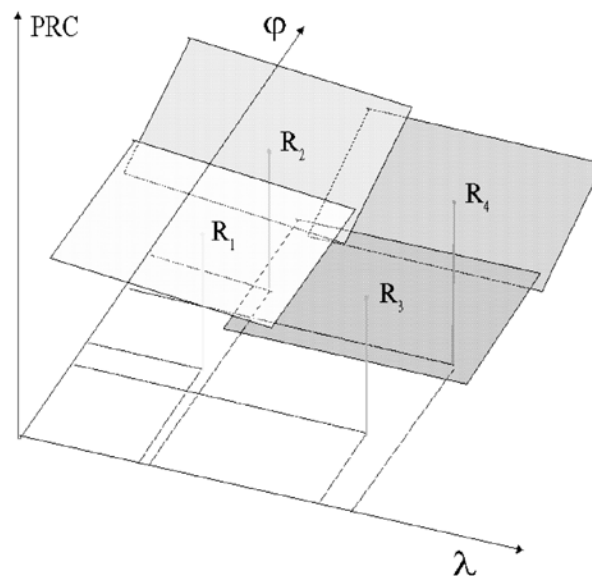


Figure 4.5: Schema of linear FKP planes for four reference stations (adapted from Wübbena et al., 2001).

- **PPP-RTK**

One limitation of PPP is that it is not possible to resolve ambiguities as integers, since the ionospheric-free linear combination is not based on integer ambiguities. Therefore, a long observation time is required. To overcome this limitation the state space modeling from the RTK network can be used. Since all individual GNSS errors in RTK networks can be consistently derived in real-time, the state space modeling PPP can resolve integer ambiguities and achieve the accuracy level of network RTK. The synthesis of those two methods is named PPP-RTK (Wübbena et al., 2005). The performance of fast ambiguity resolution and the high-accuracy positioning of the PPP-RTK has been demonstrated by several studies (Geng et al., 2010; Geng et al., 2009; Mervart et al., 2008).

All above mentioned approaches (with corrections from reference stations) are demonstrated to be very efficient for high-precision geodetic applications. But the ambiguity parameters of the reference stations must be resolved to generate the corrections. If the ambiguity parameter of one satellite cannot be estimated, the correction for the satellite will also not be available. This is a significant limitation of those approaches.

4.2 The SEID algorithm

Currently (as of March 2011), tropospheric products from about 320 German and European GPS stations (**Figure 4.6**) are generated with the EPOS software (see, e.g., Gendt et al. (2004) and Dick et al. (2000)). The atmospheric products are available in near real-time and post-processing mode as well. The ZTDs and IWVs are estimated every 15 minutes. STDs are obtained with a sampling rate of 2.5 minutes.

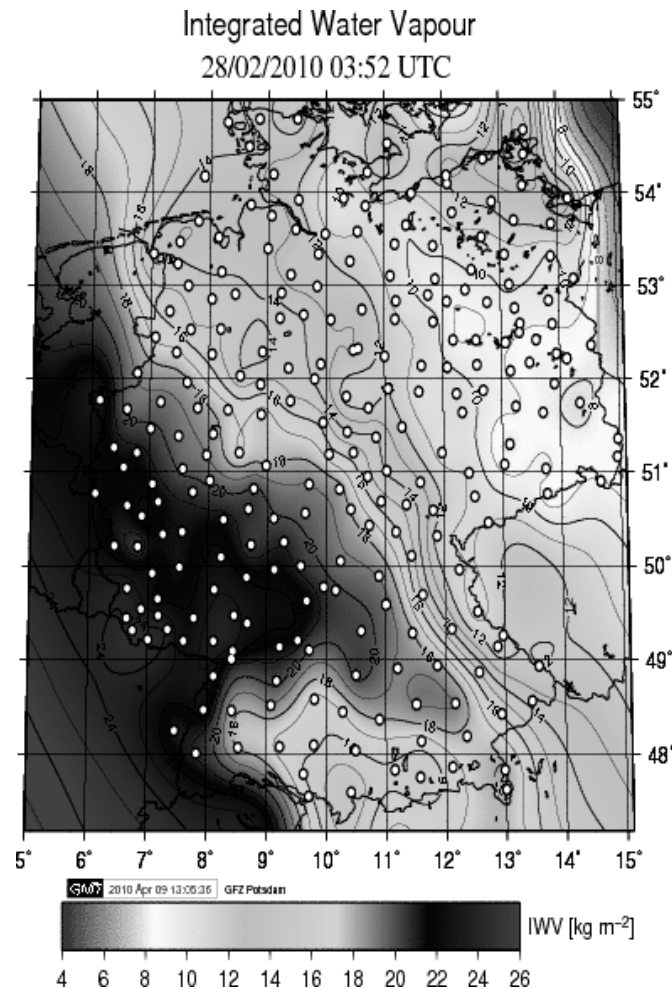


Figure 4.6: Interpolated IWV distribution over Germany provided by GFZ (see Chapter 2.2), the white circles indicate the GPS stations providing IWV data.

Due to the continually increasing number of GPS stations the PPP model is used to estimate the ZTDs and STDs. Every station is processed separately while fixing the high-quality GPS orbits and clocks. This analysis strategy makes it possible that the processing of even thousands of stations can easily be distributed over various PCs (Gendt et al., 2004).

In PPP mode the ionosphere-free observations L_3 and P_3 are used, i.e., the first-order ionospheric delay is cancelled. The second-order ionospheric delay, caused by the Faraday rotation effect induced by the Earth's magnetic field, is about 1,000 times smaller than the first-order ionospheric delay (Kedar et al., 2003), i.e., about < 10 mm, which is ignored in the EPOS software. In the next upgrade of the EPOS software the second-order ionospheric correction will be applied.

Since the SF receiver can only track the L_1 signals, the ionospheric delay cannot be canceled by computing L_3 from L_1 and L_2 observations. To process the SF data using the EPOS software the ionospheric delay of the SF data must be corrected in advance. Generally most of the existing ionospheric models are usually developed for large regions and cannot capture small scale and rapid ionospheric fluctuations (Rocken, Johnson and Braun, 2000; Schaer, 1999). These models are not accurate enough for the ZTD estimation.

Some new approaches were developed by Rocken et al., (2000) and Janssen and Rizos, (2005), where precise ionospheric corrections for SF stations are derived from the

observation residuals of the DF observations of the reference stations. With the widely used VRS the ionospheric delay of the SF receiver can be considerably reduced by forming short baselines with the VRS station. Alternatively, the ionospheric corrections can be generated using the FKP method (for more details see chapter 4.3). The approaches above mentioned are very efficient for precise SF data processing even in real-time. But there are three disadvantages: 1) the development of such specialized software needs years, 2) these approaches are GPS software package dependent, and cannot be implemented directly into other types of GPS software packages, 3) however, the most important disadvantage is the need of resolving ambiguity parameters of the reference stations in advance.

On the other hand, the processing scheme is quite different from most of the operational GPS meteorology systems, where software packages like BERNESE, EPOS, GAMIT, GPSNET_2.0, or GIPSY are applied. Within E-GVAP there are 13 agencies, which use the following software packages:

Software version	Analysis center (AC)
GIPSY	ASI, NGAA
BERNESE V5.0	BKG, GOP1, IES2, IGE, KNMI, METO, ROB, SGN
EPOS_P.V2	GFZ
GAMIT 10.3	IRE1
GPSNET_2.0	LPTR

Table 4.1: The software packages, which are used by the analysis centers in E-GVAP (status March 2011) (<http://egvap.dmi.dk>, all the AC names can be found in the list of abbreviations).

A new approach, which should be independent from the GPS software packages, is required. The new approach should have the ability to process SF data in near real-time and possibly in real-time for GPS meteorology applications.

4.2.1 Detailed description of the developed ionosphere correction method (SEID)

The ionosphere, ranging from altitudes of 50 to 1,000 km, gives rise to a signal delay which causes significant range errors. Fortunately, the ionospheric delay is frequency-dependent and can be reduced to a millimeter or less by forming particular linear combinations of the observations from the two frequencies L_1 and L_2 . An adequate expression for the ionosphere group delay d_{ion} and the ionosphere phase advance ϕ_{ion} for a microwave propagating from the satellite to the ground receiver is:

$$d_{ion} = -\phi_{ion} \cdot \frac{c}{f} = \alpha \cdot \frac{STEC}{f^2},$$

with

$$\alpha \approx 40.28 \left[m \cdot TECU^{-1} \cdot s^{-2} \right]$$

where d_{ion} is ionospheric group delay in meter; ϕ_{ion} ionospheric phase advance in units

of cycles; *STEC* is Slant Total Electron Content, giving in TECU, and f is signal frequency.

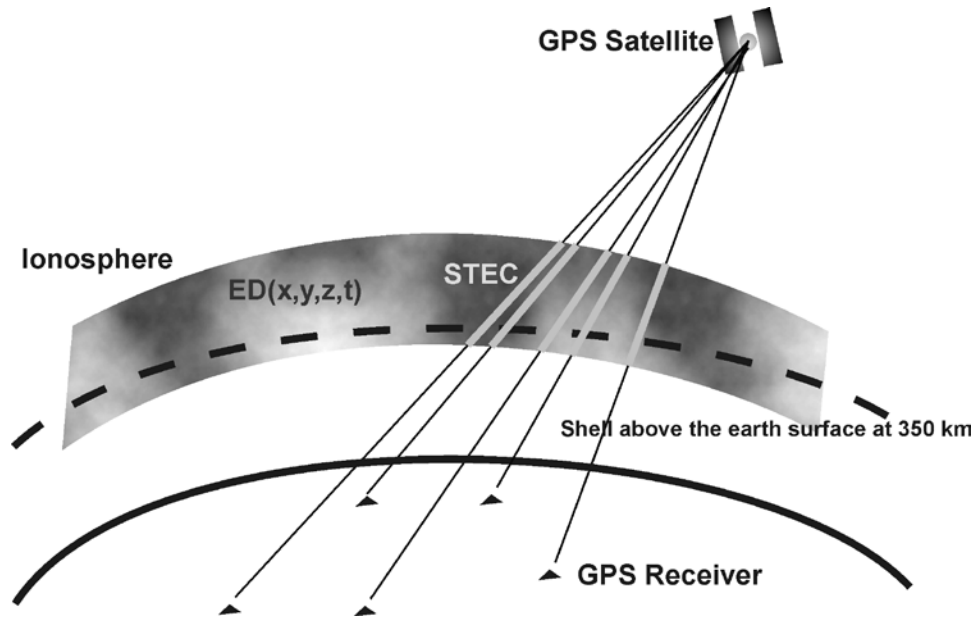


Figure 4.7: The ionospheric electron content can be approximated by a single shell with a height of 350 km.

It can be assumed that the electron density in the ionosphere is a 4D function $ED(x, y, z, t)$, where x, y, z are terrestrial coordinates in the Earth-centered Earth-fixed coordinate system like, e.g., IGS05; t is the GPS time. Regarding one GPS satellite, the *STEC* can be obtained by integration of $ED(x, y, z, t)$ along the signal path between the satellite and the receiver. Similar to the single layer ionospheric model by Klobuchar the *STEC* is represented by its IPP on a shell above the Earth's surface at 350 km, where the peak of the maximum electron concentration (F2 layer) locates approximately (**Figure 4.7**):

$$STEC(\lambda, \theta, t) = \int_{rec.}^{sat.} ED(x, y, z, t) ds. \quad (4.5)$$

Since the ionosphere extends from 50 km to 1,000 km and shows a more irregular distribution than the troposphere, the accuracy of the ionospheric observations will be reduced by the *STEC* to *VTEC* mapping. Therefore, the *VTEC* models are not sufficient for high-precise GPS applications. To obtain precise ionospheric corrections for GPS receivers, the *STEC* should be used. It is also possible to get *STEC* estimates from phase-smoothed code observations. However, the code observation's accuracy is on decimeter level. This kind of *STEC* corrections can be used for the ionospheric correction of code observations, but it is not accurate enough for phase observation correction.

The ionospheric observation $L_{4,A}^i$, which is normally used for constructing the ionospheric model, is defined as:

$$\begin{aligned}
L_{4,A}^i &= L_{1,A}^i - L_{2,A}^i \\
&= N_{1,A}^i \lambda_1 - N_{2,A}^i \lambda_2 + A_{Ion} \cdot STEC(\lambda, \theta) - PWU_{4,A}^i \\
&\quad - PCV_4^i - PCO_4^i + d_4^i - PCV_{4,A}^i - PCO_{4,A}^i - d_{4,A}^i + \varepsilon, \\
A_{Ion} &= -\alpha \cdot \left(\frac{1}{f_1^2} - \frac{1}{f_2^2} \right),
\end{aligned} \tag{4.6}$$

where A_{Ion} is a constant; i and A are the satellite and receiver indices, respectively; $PWU_{4,A}^i$ is the phase wind up correction of $L_{4,A}^i$; PCV_4^i and PCO_4^i are the satellite PCV and PCO correction of L_4 , respectively; $PCV_{4,A}^i$ and $PCO_{4,A}^i$ are the receiver PCV and PCO correction; d_4^i and $d_{4,A}^i$ are the uncalibrated phase delays (UPD) originating from the receiver and satellite; ε is the observation error of L_4 . Since it was not possible to estimate the PCV and PCO corrections of the satellite antennas for L_1 and L_2 separately, only the PCV and PCO of the ionosphere-free linear combination L_3 are given by the IGS (Schmid et al., 2007), for L_4 observations the PCV and PCO effects of the GPS satellites cannot be taken into account at present. The PCV and PCO effects of the user antenna can be corrected using antenna calibrations, i.e., suggested by the IGS. In the ionospheric observations we neglect effects of higher order as well as differences in the ray paths between L_1 and L_2 due to bending. They may reach up to about 3.5 cm at low elevations and high ionospheric activity (Brunner and Gu, 1991; Odijk, 2002).

The ambiguity parameter in the L_4 observation is a major obstacle in the reconstruction algorithms, the L_4 from the reference stations cannot be interpolated directly to the SF stations inside the DF region. Due to the existence of UPD (Blewitt, 1989) the L_1 and L_2 ambiguities of a single DF GPS station cannot be estimated as an integer. Only DD ambiguities can be fixed, because the UPDs cancel in the DD model. To avoid estimating the ambiguities from the reference stations the epoch-difference dL_4 instead of L_4 itself is used to get the ionospheric correction for SF receivers.

The variation of L_4 between two consecutive epochs i and $i+1$ for one specific satellite-receiver link has two contributions: one is the temporal change of the ionosphere itself, i. e., the electron distributions at epoch i and $i+1$ are different; and the other part is the spatial variation due to the relative motion of the ionosphere, the receiver site and the GPS signal paths in the ionosphere. It is difficult to separate the two effects. The STEC observations at epoch i and $i+1$ are given by $STEC(\lambda, \theta, t_i)$ and $STEC(\lambda, \theta, t_{i+1})$ respectively. Both STECs are continuous in λ and θ ; therefore, the difference $dSTEC(\lambda, \theta, t_i, t_{i+1})$ or dL_4 is also a continuous function of λ and θ (**Figure 4.8**).

$$\begin{aligned}
dL_{4,A}^i(t_i, t_{i+1}) &= L_{4,A}^i(t_{i+1}) - L_{4,A}^i(t_i) \\
&= A_{Ion} \cdot dSTEC(\lambda, \theta, t_i, t_{i+1}) - dPWU_{4,A}^i(t_i, t_{i+1}) \\
&\quad - dPCV_{4,A}^i(t_i, t_{i+1}) - dPCO_{4,A}^i(t_i, t_{i+1}) + \varepsilon.
\end{aligned} \tag{4.7}$$

Where $PWU_{4,A}^i$, $PCV_{4,A}^i$ and $PCO_{4,A}^i$ are the sum effect of the PWU , PCV and PCO of the satellite and receivers at the L_4 observations; the $dPWU_{4,A}^i$, $dPCV_{4,A}^i$ and $dPCO_{4,A}^i$ are their differences between the epoch i and $i+1$.

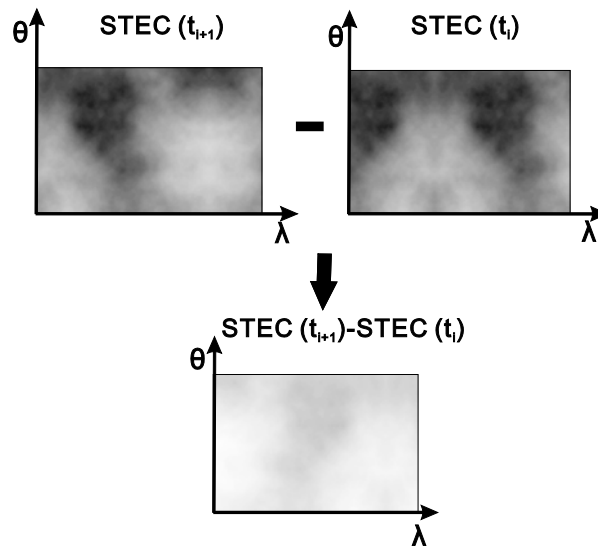


Figure 4.8: Schema of the *dSTEC* and *STEC*.

In a GPS network consisting of DF and SF receivers the ionosphere variation $dSTEC(\lambda, \theta, t_i, t_{i+1})$ can be interpolated with high-precision for SF GPS stations surrounded by DF stations. Similar to the residual fit (Rocken, Johnson and Braun, 2000) or area correction parameters (FPK) the epoch-differenced ionosphere delays dL_4 from a set of reference stations to a specific satellite can be fitted to a linear function, e.g., a plane. The linear function is evaluated at the IPPs of the SF stations in order to obtain the dL_4 value at a given latitude θ and longitude λ (**Figure 4.9**). The ionosphere pierce points IPP(λ, θ) on the shell can be estimated from the known coordinates of the sites and the satellite.

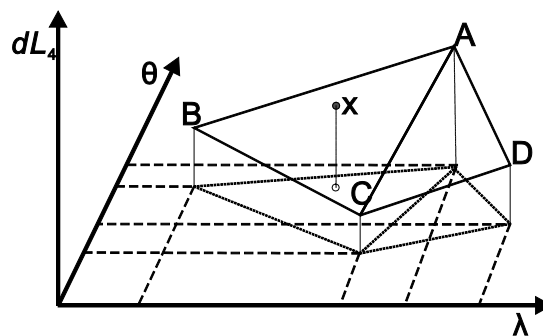


Figure 4.9: The four points A, B, C and D are IPPs from reference stations, dL_4 can be interpolated to a point x inside the region defined by A, B, C and D.

The dL_4 can be modeled by a plane as:

$$dL_4 = a_0 + a_1 \Delta\lambda + a_2 \Delta\theta,$$

with

$$\Delta\lambda = \lambda - \bar{\lambda}, \quad \Delta\theta = \theta - \bar{\theta}, \tag{4.8}$$

and

$$\bar{\lambda} = \frac{1}{n} \sum_{i=1}^n \lambda_i, \quad \bar{\theta} = \frac{1}{n} \sum_{i=1}^n \theta_i,$$

where α_0 , α_1 and α_2 are the model parameters to be estimated, $\Delta\lambda$ and $\Delta\theta$ the IPP coordinate differences to the centre of the IPP points $(\bar{\lambda}, \bar{\theta})$, n is the number of the

reference stations.

As the pseudo-range observation is usually not used or significantly down-weighted, its ionosphere correction is not as important as the correction of the carrier-phase observation. The model is established in a similar way as for the carrier-phase, but using P_4 directly instead of the epoch-differenced dP_4 ,

$$P_4 = b_0 + b_1 \Delta \lambda + b_2 \Delta \theta, \quad (4.9)$$

where b_0 , b_1 and b_2 are the model parameters to be estimated. The SEID algorithm can be derived into the steps described below.

Parameter estimation

In principle, the three parameters are determined with dL_4 observations from at least three reference stations. The parameter estimation is performed by means of a least-squares adjustment for each satellite at each epoch resulting in a satellite- and epoch-specific planar model. More reference stations will avoid problems caused by missing data and cycle slips. The calculation of the model parameters is carried out as described below:

$$\mathbf{l} + \mathbf{v} = \mathbf{A} \cdot \mathbf{x},$$

$$\hat{\mathbf{x}} = (\mathbf{A}^T \mathbf{A})^{-1} \mathbf{A}^T \mathbf{l},$$

with

$$\mathbf{l} = \begin{bmatrix} dL_{4,1} \\ \vdots \\ dL_{4,n} \end{bmatrix}, \quad \mathbf{v} = \begin{bmatrix} \varepsilon_1 \\ \vdots \\ \varepsilon_n \end{bmatrix}, \quad \mathbf{A} = \begin{bmatrix} 1 & \Delta \lambda_1 & \Delta \theta_1 \\ \vdots & \vdots & \vdots \\ 1 & \Delta \lambda_n & \Delta \theta_n \end{bmatrix}, \quad \mathbf{x} = \begin{bmatrix} a_0 \\ a_1 \\ a_2 \end{bmatrix}, \quad (4.10)$$

where n is the number of reference stations, $dL_{4,i}$ the epoch-differenced ionospheric observation from the reference station i , \mathbf{x} is the unknown parameter vector, \mathbf{A} is the design matrix and \mathbf{l} is the observation vector, here the vector of dL_4 .

Interpolation of dL_4

For a given SF station X with IPP coordinates λ_x , θ_x , the $d\tilde{L}_4$ correction can be calculated as:

$$\begin{aligned} d\tilde{L}_{4,x} &= \hat{a}_0 + \hat{a}_1 \Delta \lambda_x + \hat{a}_2 \Delta \theta_x \\ &= [1 \quad \Delta \lambda_x \quad \Delta \theta_x] \cdot \hat{\mathbf{x}} \\ &= \mathbf{w}^T \cdot \mathbf{l}, \end{aligned} \quad (4.11)$$

with

$$\begin{aligned} \mathbf{w} &= [w_1 \quad \cdots \quad w_n]^T = [1 \quad \Delta \lambda_x \quad \Delta \theta_x] \cdot (\mathbf{A}^T \mathbf{A})^{-1} \mathbf{A}^T, \\ \sum_n w_i &= 1. \end{aligned}$$

Obtaining ionospheric correction \tilde{L}_4

The ionospheric correction \tilde{L}_4 for the observation at epoch k , which was continuously

tracked since a first epoch i_0 is the sum of the epoch-differenced corrections $d\tilde{L}_4$ in between,

$$\tilde{L}_4(k) = \tilde{L}_4(i_0) + \sum_{i_0}^k d\tilde{L}_4(i), \quad (4.12)$$

where $\tilde{L}_4(i_0)$ is the ionospheric delay at epoch i_0 . $\tilde{L}_4(i_0)$ is unknown and can be an arbitrary real-value, which can be absorbed in phase ambiguities. In the integration it could be assigned to zero:

$$\tilde{L}_4(i_0) = 0. \quad (4.13)$$

Applying the correction

To implement the ionospheric correction for the SF data there are two possibilities.

a) The ionospheric delay L_1 is corrected with the simulated \tilde{L}_4 to get the ionosphere-free combination \tilde{L}_3

$$\begin{aligned} \tilde{L}_3 &= L_1 - \frac{f_2^2}{f_1^2 - f_2^2} \tilde{L}_4, \\ \tilde{P}_3 &= P_1 - \frac{f_2^2}{f_1^2 - f_2^2} \tilde{P}_4. \end{aligned} \quad (4.14)$$

If the reference stations are A, B and C, then for an inside SF station the noise of the \tilde{L}_3 is about 3.5 mm ~ 6 mm, which is smaller than the noise of L_3 of about 6 mm. However, the number of ambiguities in the \tilde{L}_3 is sum of the number of ambiguities and data gaps of the reference stations and the number of ambiguities of the SF station in L_1 . If we assume that the reference and SF stations have 8 ambiguities each, and each reference station has 8 data gaps (without cycle slip), the ambiguities and gaps from one station are different to those from other stations, since the SF \tilde{L}_3 observations have 56 ambiguities. In the data processing the increased ambiguity parameters reduce the accuracy of the ZTD estimation. To avoid this problem redundant reference stations should be used and the missing data and cycle slips should be repaired in advance.

b) In order to process the data from SF and DF receivers using the same software and procedure, we can also generate the observations \tilde{L}_2 and \tilde{P}_2 computed from the corresponding SF observations

$$\begin{aligned} \tilde{L}_2 &= L_1 - \tilde{L}_4, \\ \tilde{P}_2 &= P_1 - \tilde{P}_4. \end{aligned} \quad (4.15)$$

In the SEID model the new RINEX file with \tilde{L}_2 and \tilde{P}_2 is generated. The detailed algorithm of this approach is summarized as following:

At first, the data of the reference stations are screened to remove outliers and to identify cycle slips using the single station data cleaning approach (Turboedit TB) by Blewitt (1990). Remaining problematic data can also be detected during the model parameter estimation if there are redundant observations.

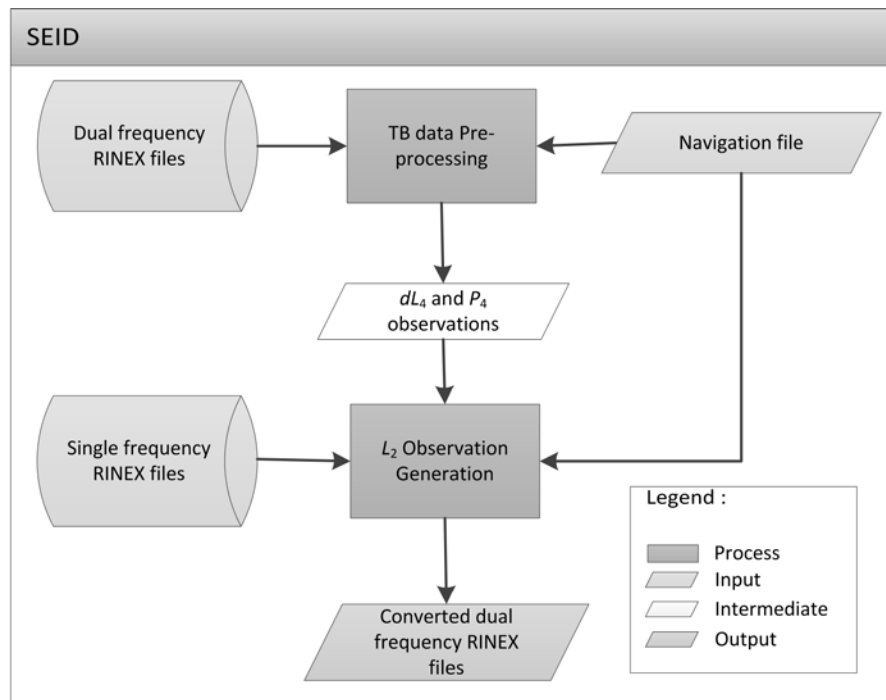


Figure 4.10: Flow diagram of SEID.

Afterwards, at each epoch all P_4 and the dL_4 observations are formed for each satellite after the antenna phase center corrections of the receivers have been applied. Then, the IPP positions for the DF signal paths are computed according to the station and satellite coordinates. The observation equations in Eq. (4.8) and (4.9) are formed and the parameters are estimated accordingly. This is repeated for all satellites at each epoch. With the coefficients a_i and b_i , the epoch- and satellite-specific ionosphere correction parameters, dL_4 and P_4 are calculated for the SF data. Finally, simulated \tilde{L}_2 and \tilde{P}_2 observations are generated according to Eq. (4.15) and are combined with the SF observations from the SF RINEX file into a new RINEX file, which has the same structure as a DF RINEX file. The new DF RINEX file can be processed like a normal real DF RINEX file.

4.2.2 Interpolation error study

In the SEID model the dL_4 observations are modeled with a planar, and interpolated for SF stations. In this section the accuracy of the interpolation is studied.

Standard deviation of \tilde{L}_4 observations

In the SEID method the \tilde{L}_4 observations of a SF station can be determined using ionospheric observations from surrounding reference stations, e.g., in the simple case of three DF stations A, B and C, according to:

$$\begin{aligned}
 \tilde{L}_{4,x}(k) &= \sum_{i=i_0}^k d\tilde{L}_4(i) \\
 &= \sum_{i=i_0}^k (w_{A,i} \cdot dL_{4,A}(i) + w_{B,i} \cdot dL_{4,B}(i) + w_{C,i} \cdot dL_{4,C}(i)) \\
 &= [w_{A,k} \cdot L_{4,A}(k) + w_{B,k} \cdot L_{4,B}(k) + w_{C,k} \cdot L_{4,C}(k) \\
 &\quad - w_{A,k} \cdot L_{4,A}(k-1) + w_{B,k} \cdot L_{4,B}(k-1) + w_{C,k} \cdot L_{4,C}(k-1) \\
 &\quad + w_{A,k-1} \cdot L_{4,A}(k-1) + w_{B,k-1} \cdot L_{4,B}(k-1) + w_{C,k-1} \cdot L_{4,C}(k-1) \\
 &\quad - w_{A,k-1} \cdot L_{4,A}(k-2) + w_{B,k-1} \cdot L_{4,B}(k-2) + w_{C,k-1} \cdot L_{4,C}(k-2) \\
 &\quad \dots \\
 &\quad + w_{A,i_0} \cdot L_{4,A}(i_0+1) + w_{B,i_0} \cdot L_{4,B}(i_0+1) + w_{C,i_0} \cdot L_{4,C}(i_0+1) \\
 &\quad - w_{A,i_0} \cdot L_{4,A}(i_0) + w_{B,i_0} \cdot L_{4,B}(i_0) + w_{C,i_0} \cdot L_{4,C}(i_0)].
 \end{aligned} \tag{4.16}$$

Between two consecutive epochs with, e.g., a 30 seconds interval, the weight quantities w_A , w_B and w_C remain almost unchanged and thus the intermediate sum of the STEC effect is close to zero. The remaining STEC effects are dominated by the L_4 differences between the first and the last epoch.

$$\begin{aligned}
 \tilde{L}_{4,x}(k) &= [w_{A,k} \cdot L_{4,A}(k) + w_{B,k} \cdot L_{4,B}(k) + w_{C,k} \cdot L_{4,C}(k) \\
 &\quad + 0 \\
 &\quad - w_{A,i_0} \cdot L_{4,A}(i_0) + w_{B,i_0} \cdot L_{4,B}(i_0) + w_{C,i_0} \cdot L_{4,i_0}(i_0)] \\
 &= \sum_{j=A}^C w_{j,k} \cdot L_{4,j}(k) - \sum_{j=A}^C w_{j,i_0} \cdot L_{4,j}(i_0).
 \end{aligned} \tag{4.17}$$

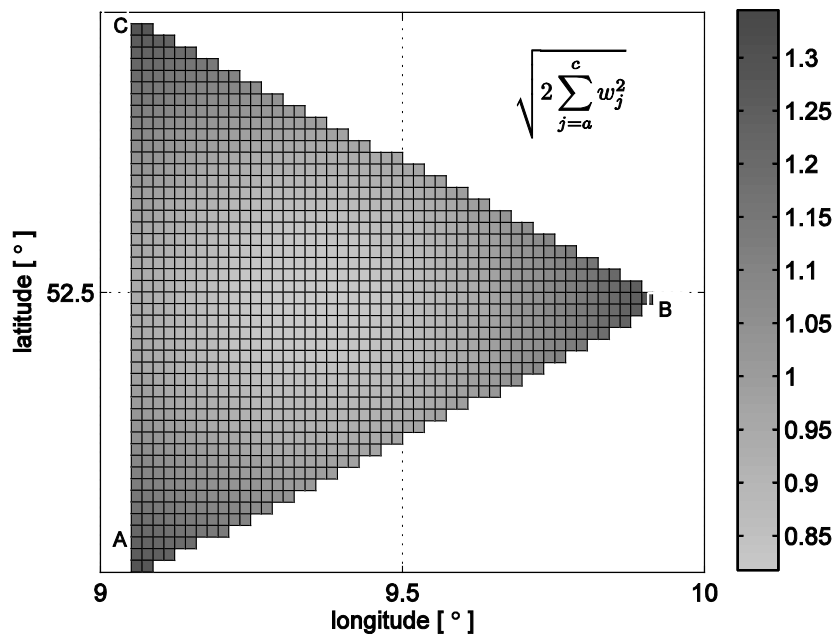


Figure 4.11: Evaluation of Eq. (4.18) for test stations inside of the triangle.

The maximum change of $w_{j,k}$ from a reference station (A, B and C) over a whole satellite track is small (about 0.018). If the L_4 observations from all reference stations have the same standard deviation σ_{L_4} , the standard deviation of $\tilde{L}_{4,x}(k)$ can be derived from the law of error propagation:

$$\sigma_{\tilde{L}_{4,x}} = \sigma_{L_4} \sqrt{\sum_{j=A}^C (w_{j,k}^2 + w_{j,i_0}^2)} \approx \sigma_{L_4} \sqrt{2 \sum_{j=A}^C w_{j,k}^2}. \quad (4.18)$$

If the SF station is located inside the triangle of the three reference stations, that are e.g., located at A(9°E, 52°N), B(9°E, 53°N) and C(10°E, 52.5°N), the $\sigma_{\tilde{L}_{4,x}}$ has a value between $\sigma_{L_4} \sqrt{2/3}$ and $\sigma_{L_4} \sqrt{2}$ (**Figure 4.11**). When the L_4 noise is about 3.3 mm, the $\tilde{L}_{4,x}$ noise can range between 2.7 mm and 4.7 mm.

Accuracy of \tilde{L}_2 observations

In the SEID model the ionospheric correction \tilde{L}_4 is generated using the ionospheric observations from several DF reference stations. With the \tilde{L}_4 observations the \tilde{L}_2 observations are calculated using Eq. (4.15). Assuming three reference stations A, B and C, the difference between the observed L_2 signals and the SEID generated \tilde{L}_2 observations at a given epoch k can be calculated as:

$$\begin{aligned} \Delta L_2(k) &= L_2(k) - \tilde{L}_2(k) \\ &= L_2(k) - (L_1(k) - \tilde{L}_4(k)) \\ &= -L_4(k) + \tilde{L}_4(k) \\ &= -I_4(k) - N_1 \lambda_1 + N_2 \lambda_2 + \sum_{i=i_0}^{k-1} \left(\sum_{j=A}^C w_{j,i} \cdot (L_{4,j}(i+1) - L_{4,j}(i)) \right) \\ &= -(I_4(k) - I_4(i_0)) + \sum_{i=i_0}^{k-1} \left(\sum_{j=A}^C w_{j,i} \cdot (L_{4,j}(i+1) - L_{4,j}(i)) \right) \\ &\quad + (-N_1 \lambda_1 / \lambda_2 + N_2 - I_4(i_0) / \lambda_2) \lambda_2, \end{aligned} \quad (4.19)$$

which can be separated into two parts:

$$\Delta I_4(k) = -(I_4(k) - I_4(i_0)) + \sum_{i=i_0}^{k-1} \left(\sum_{j=A}^C w_{j,i} \cdot (L_{4,j}(i+1) - L_{4,j}(i)) \right), \quad (4.20)$$

$$\Delta N_2 = (N_2 - (N_1 \lambda_1 + I_4(i_0)) / \lambda_2),$$

where ΔI_4 is the difference between the observed and interpolated ionosphere variation from epoch i_0 to epoch k and ΔN_2 is the ambiguity difference between L_2 and \tilde{L}_2 observations. Since N_1 and $I_4(i_0)$ are unknown, ΔN_2 is not an integer. However, in PPP mode where the ambiguity parameters cannot be fixed to integer, ΔN_2 has no impact on the data processing.

The accuracy of the \tilde{L}_2 observations depends on the accuracy of the ionospheric correction, i.e., the \tilde{L}_4 interpolation:

$$\tilde{L}_4 = \sum_{i=i_0}^k \left(\sum_{j=A}^C w_{j,i} \cdot (L_{4,j}(i) - L_{4,j}(i-1)) \right). \quad (4.21)$$

Since L_4 observations include STEC, PWU and satellite PCV effects, each of the effects can cause an interpolation error.

STEC ionospheric interpolation error

Firstly, the interpolation error of the STEC is studied exemplarily for three consecutive epochs 0 to 3.

$$\begin{aligned} \Delta I_{4,STEC}(3) = & A_{Ion} \cdot [w_{A,3} \cdot STEC_{4,A}(3) + w_{B,3} \cdot STEC_{4,B}(3) + w_{C,3} \cdot STEC_{4,C}(3) \\ & - w_{A,3} \cdot STEC_{4,A}(2) + w_{B,3} \cdot STEC_{4,B}(2) + w_{C,3} \cdot STEC_{4,C}(2) \\ & + w_{A,2} \cdot STEC_{4,A}(2) + w_{B,2} \cdot STEC_{4,B}(2) + w_{C,2} \cdot STEC_{4,C}(2) \\ & - w_{A,2} \cdot STEC_{4,A}(1) + w_{B,2} \cdot STEC_{4,B}(1) + w_{C,2} \cdot STEC_{4,C}(1) \\ & + w_{A,1} \cdot STEC_{4,A}(1) + w_{B,1} \cdot STEC_{4,B}(1) + w_{C,1} \cdot STEC_{4,C}(1) \\ & - w_{A,1} \cdot STEC_{4,A}(0) + w_{B,1} \cdot STEC_{4,B}(0) + w_{C,1} \cdot STEC_{4,C}(0)] \\ & - A_{Ion} \cdot [STEC_{4,x}(3) - STEC_{4,x}(0)]. \end{aligned} \quad (4.22)$$

If the spatio-temporal variation of the ionosphere over the densified GPS network is smooth, its effect can be modeled with a plane or a low-order surface, then we have:

$$\begin{aligned} STEC_{4,x}(0) &= w_{A,0} \cdot STEC_{4,A}(0) + w_{B,0} \cdot STEC_{4,B}(0) + w_{C,0} \cdot STEC_{4,C}(0), \\ STEC_{4,x}(3) &= w_{A,3} \cdot STEC_{4,A}(3) + w_{B,3} \cdot STEC_{4,B}(3) + w_{C,3} \cdot STEC_{4,C}(3). \end{aligned} \quad (4.23)$$

However, under rapid variations of the ionosphere, e.g., Traveling Ionospheric Disturbances (TID), the ionospheric effect is difficult to be modeled with a plane or a low-order surface. In Chapter 4.3.3 such situations will be discussed in detail.

With Eq. (4.23) the remaining STEC errors $\Delta_{4,STEC}(3)$ in $\Delta I_{4,STEC}(3)$ are only from epoch 1 and 2:

$$\begin{aligned} \Delta_{4,STEC}(3) = & A_{Ion} \cdot [- w_{A,3} \cdot STEC_{4,A}(2) + w_{B,3} \cdot STEC_{4,B}(2) + w_{C,3} \cdot STEC_{4,C}(2) \\ & + w_{A,2} \cdot STEC_{4,A}(2) + w_{B,2} \cdot STEC_{4,B}(2) + w_{C,2} \cdot STEC_{4,C}(2) \\ & - w_{A,2} \cdot STEC_{4,A}(1) + w_{B,2} \cdot STEC_{4,B}(1) + w_{C,2} \cdot STEC_{4,C}(1) \\ & + w_{A,1} \cdot STEC_{4,A}(1) + w_{B,1} \cdot STEC_{4,B}(1) + w_{C,1} \cdot STEC_{4,C}(1)]. \end{aligned} \quad (4.24)$$

In order to study the interpolation error caused by the STEC interpolation the VTEC product from CODE is applied. The single layer model is used to calculate STEC (**Figure 4.1**):

$$STEC = VTEC / \cos(z'), \quad (4.25)$$

where z' is the satellite's zenith angle at the IPP.

Four SAPOS stations are selected, three serve as reference stations (0514, 0525 and 0932), and the target station 0527 is assumed to be a SF station (**Figure 4.14**). In DOY 219 in 2011 the VTEC over Europe increased from 2 TECU at midnight to 20 TECU at noon. The IPPs of the observations are calculated using the GPS broadcast file. The result is plotted in top panel of **Figure 4.12** for the whole arc of each observed satellite. The grey value of the lines indicates a different satellite. The interpolation error $\varepsilon_{4,STEC}$

is between ± 1 mm. The RMS of the errors is about 0.3 mm, and can therefore be ignored. However, under abnormal ionospheric activity like the Halloween super-storm of 29-31 October 2003 (A.Pulkkinen et al., 2005), the STEC interpolation error will increase up to ± 4 mm at low elevations (bottom panel **Figure 4.12**). However, it should be noted that the TEC-maps are very smooth, so no about highly variable part can be drawn.

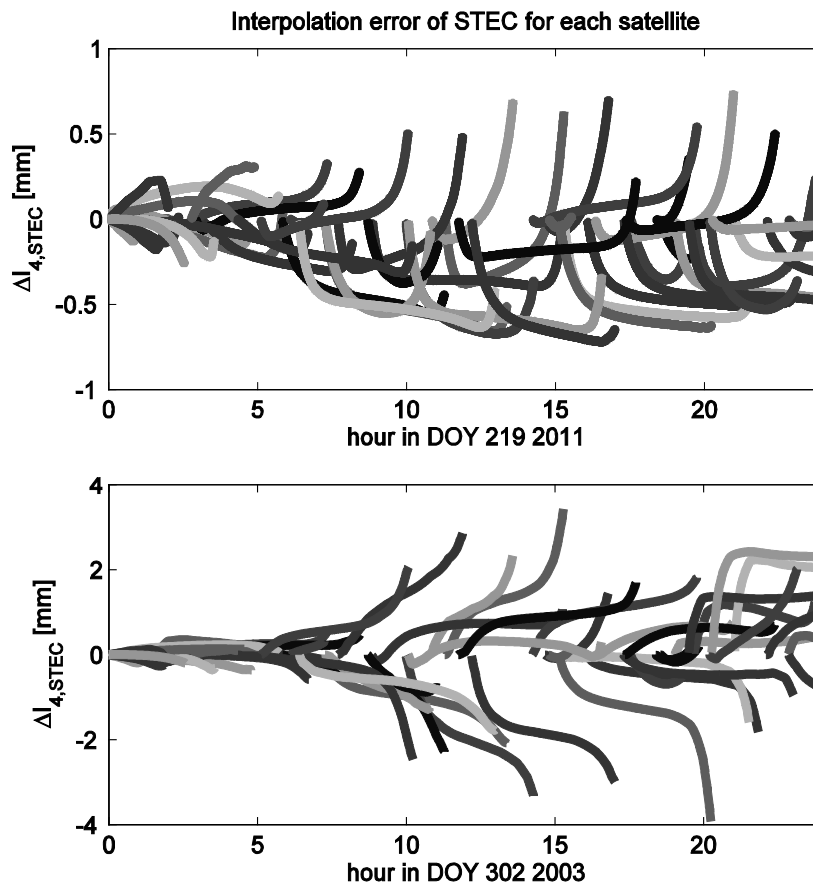


Figure 4.12: The STEC interpolation errors on DOY 219 in 2011 (top) and on DOY 302 in 2003 (bottom). The interpolation error sets zeros at the first epoch of a satellite track.

PWU interpolation error and satellite PCV/PCO

Similar to the STEC interpolation error the error caused by PWU effect $\Delta I_{4,PWU}$ is studied. The PWU interpolation errors are much smaller than one millimeter (**Figure 4.13**) and have no impact on the SEID method. Since only L_3 PCV/PCO of the satellite antenna are available, the PCV/PCO interpolation error cannot be estimated. All above mentioned errors are caused by small differences between the weights at consecutive epochs in Eq.(4.24), e.g., $w_{A,2} \neq w_{A,3}$. The short time interval between two consecutive epochs can reduce such errors. \tilde{L}_4 observations are independent of the L_1 observation of the SF station, the accuracy of the converted \tilde{L}_2 observations can be expressed as:

$$\delta \tilde{L}_2 = |\delta L_1| + |\delta \tilde{L}_4| + |\delta \Delta L_4|. \quad (4.26)$$

The δL_1 of the NovAtel SMART-V1 receiver is 1.3 mm (**Table 3.2**), and the noise of

$\tilde{L}_{4,x}$ is between 2.7 mm and 4.7 mm. The resulting noise of the converted \tilde{L}_2 observations of a NovAtel SMART-V1 receiver is about 4.0 – 6.0 mm, which is 2 – 4 mm larger than the L_2 noise of a geodetic DF receiver (about 2 mm). However, for low-cost SF receivers the impact of the unmodeled site-specific effects, e.g., multi-path effects and unmodeled antenna PCV are more significant than the interpolation errors.

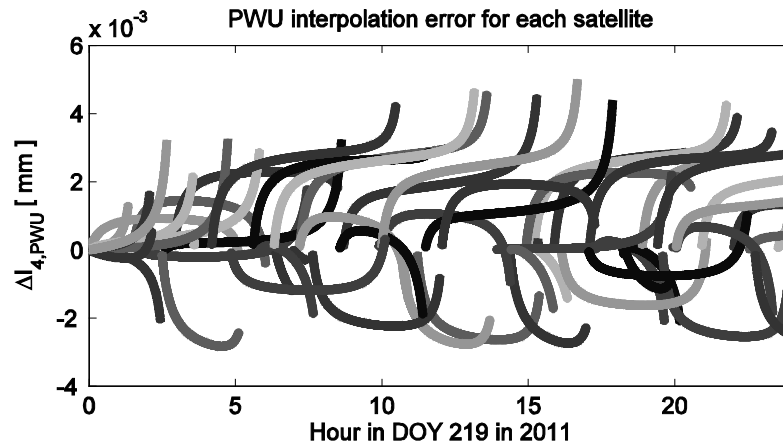


Figure 4.13: The PWU interpolation errors on DOY 219 in 2011. The interpolation error sets zeros at the first epoch of a satellite track.

Station-specific effects

The ionospheric observations from DF receivers can be corrupted by multi-path effects and other station-specific effects. To study the interpolation error caused by such errors from reference stations, a sub-network from the SAPOS network composed of 11 stations with DF receivers is selected. In **Figure 4.14**, the GPS station 0527 (marked with a circle) is assumed to be a SF GPS station, and the other 10 nearest stations serve as reference stations for the ionospheric correction.

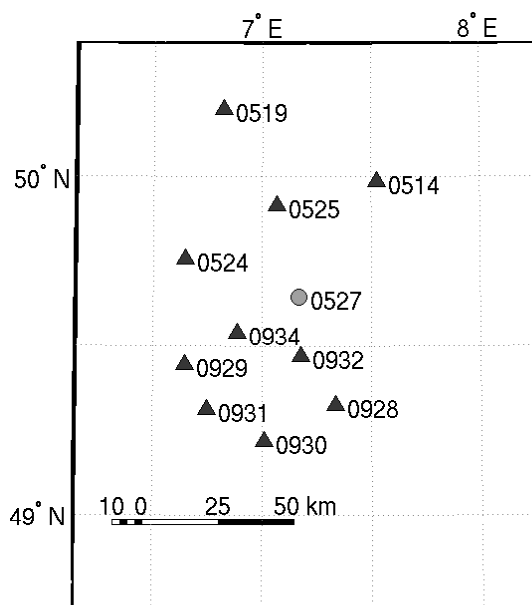


Figure 4.14: 10 SAPOS stations (triangles) around the assumed SF station 0527 (circle) served as reference stations for the interpolation error study.

The 11 DF stations are equipped with geodetic high-quality GPS receivers and located in the Western part of Germany. All 10 stations are within a radius of 50 km from the station 0527. Data observed on DOY 225 in 2007 are used. The dL_4 observations of the satellite 18 from the 11 stations are plotted in **Figure 4.15** with the elevation angles. The grey values of the lines identify the dL_4 observations of the 11 stations.

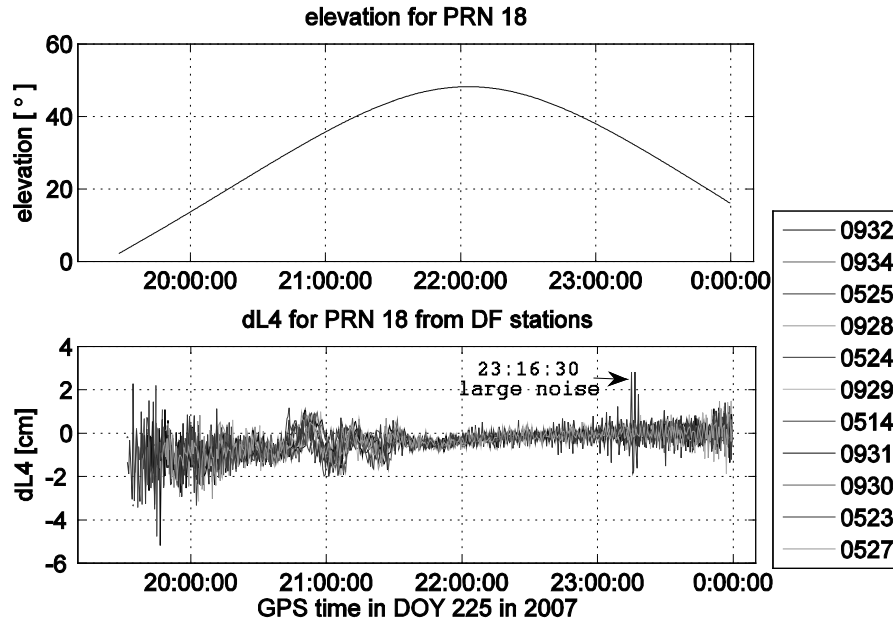


Figure 4.15: Elevation of PRN 18 (top); dL_4 of PRN 18 from the 11 stations (bottom); the sampling interval is 30 seconds.

In general the dL_4 observations at low elevation angles ($< 20^\circ$) have a larger noise level than the observations at higher elevations. In EPOS the observations with elevations below 30° are down-weighted to reduce the impact of the larger noise and unmodeled effects. Therefore, for the ZTD estimation the error of the interpolated ionospheric corrections at low elevation has a smaller impact than those at high elevations. The dL_4 data from the 11 stations show that the dL_4 error from the reference stations could be up to several centimeters even at an elevation angle of 30° . At 23:16:30 (GPS time) the dL_4 error of the station 0524 is larger than 2 cm (**Figure 4.16**) compared to the other stations.

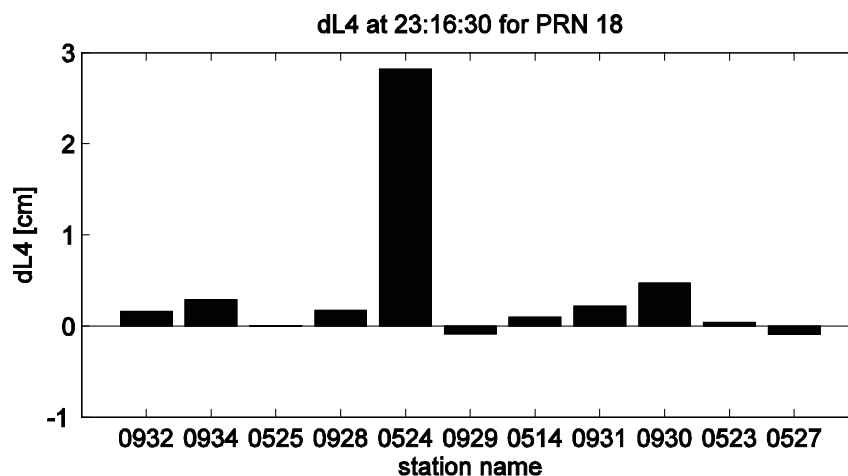


Figure 4.16: dL_4 observations from the 11 DF stations at GPS time 23:16:30 of DOY 225 in year 2007 for PRN 18; the elevation angle of the satellite is about 33° .

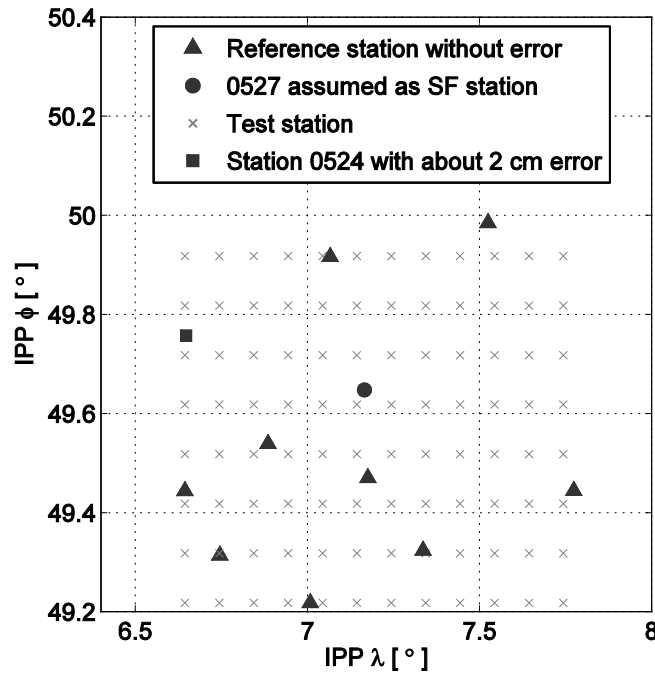


Figure 4.17: The distribution of the 9 SAPOS reference stations (triangles) without error in dL_4 observation, one reference station 0524 (square) with a rather large error and symmetrically distributed test stations (crosses).

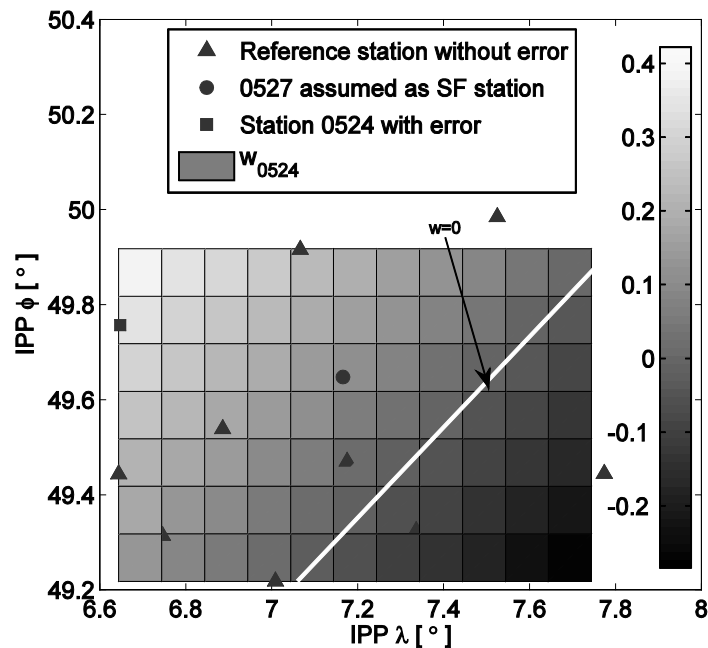


Figure 4.18: The variation of the coefficient w of the station 0524 with respect to the location of the test station. The white line indicates $w = 0$.

If in the interpolation the observation of the station 0524 is used, the variation of the contribution parameter w of the station 0524 is between -0.28 and 0.42 (Figure 4.18). If a dL_4 error of 2.5 cm is assumed for station 0524, an error between -0.7 cm and 1.05 cm can be expected for the interpolated dL_4 value. For the assumed SF station 0527 the contribution parameter w for the station 0524 is about 0.11.

In order to estimate the impact of a reference station with a rather large dL_4 error, the dL_4 observation at the assumed SF station was interpolated with and without the

erroneous station 0524. Using the data of station 0524 the interpolated dL_4 observation at station 0527 is 0.42 cm. This leads to an error of 348% as compared to the 0.09 cm obtained with the data of station 0527. Without station 0524 the interpolated dL_4 observation is 0.11, i.e., an error of 19%.

There are two approaches to avoid the interpolation errors caused by the dL_4 errors from the reference stations. 1) In the reference data pre-processing an elevation-dependent threshold value for the error detection can be applied, i.e., the threshold at low elevations (below 30°) is larger than that at high elevations. 2) When redundant observations are available, a robust test can be used to detect outliers.

4.2.3 Densification study

In order to evaluate the efficiency of the SEID method for the ZTD estimation, a sub-network consisting of eight DF stations from the COPS⁴ region (Wulfmeyer et al., 2008) is assumed to be SF stations to simulate the densification. A densification scenario is defined by selecting 27 stations from the surrounding network as already existing reference network, which is assumed to be densified with the eight embedded SF stations (**Figure 4.19**).

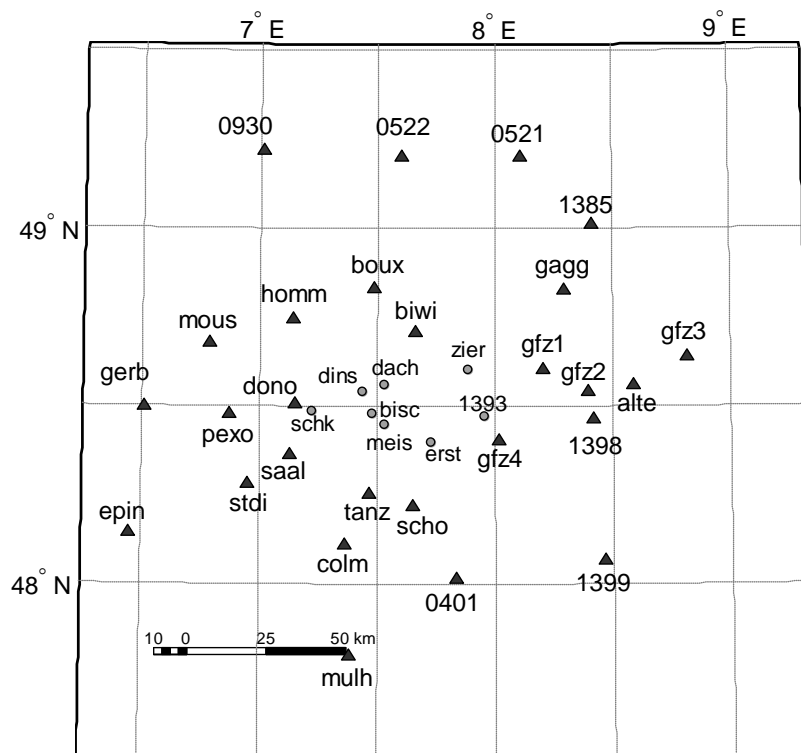


Figure 4.19: Densification test network: The 27 triangles are the reference stations with DF receivers (triangles), and eight stations assumed to be SF stations (circles).

Since the 35 stations were operated by several providers, eight different types of receivers and ten different types of antennas were found among the 35 stations. In **Table 4.2** and **Table 4.3** the receiver types, antenna types and observation cut-off angles of the reference stations and test stations are given. The antennas of the eight SAPOS

⁴ Convective and Orographically-induced Precipitation Study (<http://www.cops2007.de/>).

stations (named by number) were individually and absolutely calibrated by a robot. The antenna PCV/PCO effects of the other stations were corrected with type-specific antenna corrections.

Based on the 27 reference stations, 24 densification scenarios were identified, to study the impact of the separation between reference stations as well as the differences in equipment and the number of reference stations. The averaged distances of the reference stations to the SF test stations ranges from 33 to 87 km and the number of reference stations varies from four to eight. To simplify the later discussion the 24 scenarios are classified into three groups, called 'small', 'middle' and 'large', which are listed in **Table 4.4**. The different reference stations are used to generate ionospheric corrections, and the averaged distances of the reference stations to test SF stations are given.

Station name	Receiver type		Antenna type		Cut-off angle [°]
0401	LEICA	SR520	LEIAT503	LEIC	0
0521	LEICA	GRX1200GGPRO	LEIAT503	LEIC	0
0522	LEICA	GRX1200GGPRO	LEIAT503	LEIC	0
0930	OEM_3	MILLENRT2	NOV503_CR	NONE	0
1385	JPS	LEGACY	TRM29659_00	NONE	0
1398	LEICA	SR520	LEIAT303	LEIC	0
1399	LEICA	SR520	LEIAT303	LEIC	3
ALTE	ASHTECH	UZ_12	ASH701945B_M	NONE	0
BIWI	LEICA	GRX1200GGPRO	LEIAX1202GG	NONE	10
BOUX	ASHTECH	UZ_12	ASH701945B_M	NONE	0
COLM	ASHTECH	UZ_12	ASH701945B_M	NONE	0
DONO	ASHTECH	UZ_12	ASH701945B_M	NONE	3
EPIN	TRIMBLE	NETRS	TRM41249_00	NONE	0
GAGG	ASHTECH	UZ_12	ASH701945B_M	NONE	0
GERB	TRIMBLE	NETRS	TRM41249_00	NONE	0
GFZ1	TRIMBLE	4000SSE	TRM14532_00	NONE	5
GFZ2	TRIMBLE	4000SSE	TRM14532_00	NONE	5
GFZ3	TRIMBLE	4000SSE	TRM14532_00	NONE	5
GFZ4	TRIMBLE	4000SSE	TRM14532_00	NONE	5
HOMM	ASHTECH	UZ_12	ASH701945B_M	NONE	0
MOUS	LEICA	GRX1200GGPRO	LEIAX1202GG	NONE	10
MULH	TRIMBLE	NETRS	TRM41249_00	NONE	0
PEXO	ASHTECH	UZ_12	ASH701945B_M	NONE	0
SAAL	ASHTECH	UZ_12	ASH701945B_M	NONE	0
SCHO	ASHTECH	UZ_12	ASH701945B_M	NONE	0
STDI	TRIMBLE	NETRS	TRM29659_00	NONE	0
TANZ	ASHTECH	UZ_12	ASH701945E_M	NONE	5

Table 4.2: List of receiver types, antenna types and observation cut-off angles of the reference stations.

The data from DOY 220 to 229 in 2007 are used. The daily data of the selected eight test stations is processed twice using the EPOS software. Firstly, the DF data of the eight test stations are processed to estimate the ZTD parameters. The ZTD products serve as the reference solution in the validations. Then for each densification scenario the L_2 and P_2 observations of the eight test stations were generated from the surrounding

reference stations using the SEID model. The converted DF data are processed in the same way as the DF data. The retrieved ZTD parameters from the converted DF data are compared with the reference solution.

Station name	Receiver type		Antenna type		Cut-off angle [°]
1393	LEICA	SR520	LEIAT503	LEIC	0
BISC	ASHTECH	UZ_12	ASH701945B_M	NONE	0
DACH	ASHTECH	UZ_12	ASH701945B_M	NONE	0
DINS	ASHTECH	UZ_12	ASH701945B_M	NONE	0
ERST	ASHTECH	UZ_12	ASH701945B_M	NONE	0
MEIS	ASHTECH	UZ_12	ASH701945B_M	NONE	0
SCHK	ASHTECH	UZ_12	ASH701945B_M	NONE	0
ZIER	ASHTECH	UZ_12	ASH701945B_M	NONE	0

Table 4.3: List of receiver and antenna types of the test stations.

Name	Distance [km]	Reference stations
Group: Large		
A1	87	EPIN, 0930, 1385, MULH
A2	83	0522, GFZ3, MULH, GERB
A3	85	0522, GFZ3, MULH, GERB, EPIN
A4	85	0522, GFZ3, MULH, GERB, EPIN, 1385
A5	86	0522, GFZ3, MULH, GERB, EPIN, 1385, 0930
A6	86	0522, GFZ3, MULH, GERB, EPIN, 1385, 0930, 0521
Group: Middle		
M1	61	HOMM, GAGG, STDI, 1399
M2	54	MOUS, 1398, BOUX, COLM
M3	53	MOUS, GAGG, BOUX, COLM
M4	52	BOUX, PEXO, GAGG, COLM
M5	51	PEXO, 1398, BOUX, COLM
M6	58	BOUX, PEXO, GAGG, COLM, 1399
M7	58	BOUX, GAGG, STDI, 1399, COLM
M8	59	HOMM, GAGG, STDI, COLM, 1399
M9	58	BOUX, MOUS, PEXO, GAGG, 1399, COLM
M10	59	BOUX, MOUS, PEXO, GAGG, 1399, COLM, 0401
M11	61	BOUX, MOUS, PEXO, GAGG, 1399, COLM, 0401, ALTE
Group: Small		
S1	47	DONO, GFZ2, 1398, TANZ
S2	39	DONO, BIWI, 1398, TANZ
S3	33	GFZ4, TANZ, DONO, BIWI
S4	33	BIWI, GFZ4, DONO, SCHO
S5	39	DONO, BIWI, 1398, TANZ, GFZ4
S6	37	BIWI, GFZ4, DONO, SCHO, SAAL, GFZ1
S7	36	BIWI, GFZ4, DONO, SCHO, SAAL, GFZ1, TANZ

Table 4.4: The three densification scenario groups referred to as ‘large’, ‘middle’ and ‘small’.

All the eight test stations have no observation gaps during the ten days. **Figure 4.20** shows the RMS of the ZTD differences of each test station for the 24 densification scenarios. Most of the RMS values are smaller than 5 mm, i.e., smaller than the GPS measurement noise in the ZTD estimation of 7 mm (Haase et al., 2003). In the three groups of scenarios the increasing number of reference stations clearly improves the accuracy of the ZTD products and avoids problems caused by missing data of the reference stations.

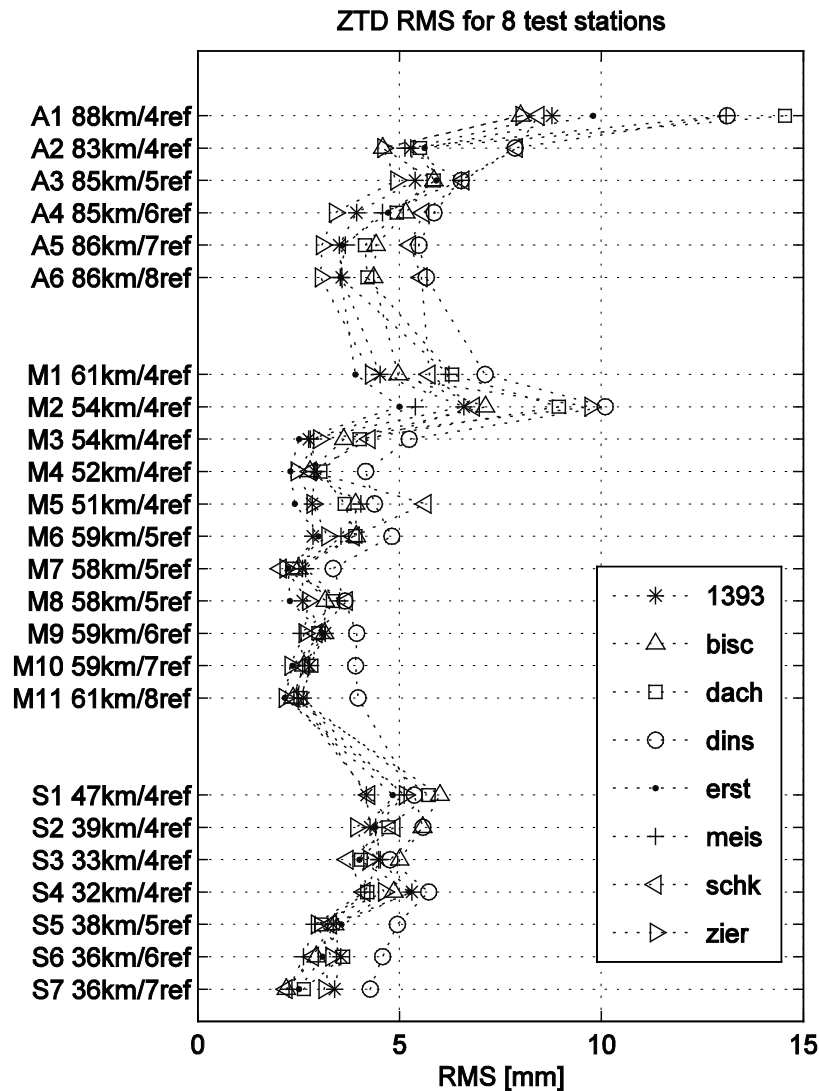


Figure 4.20: RMS of the ZTD differences between the DF results and the SF results for each test station in the 24 densification scenarios. The Y-axis shows the densification scenarios with the number of reference stations and average distances from the test stations to the reference stations. The X-axis shows the RMS of the ZTD differences.

Generally the RMS decreases with the number of the reference stations, and increases with the inter-station distances. The scenario groups ‘small’ and ‘middle’ have similar RMS levels. Within average distances up to 60 km the ionospheric correction can be modeled with almost the same accuracy level. In the ‘small’ and ‘middle’ groups the accuracy of the retrieved ZTD estimates from the SF data significantly depends on the selection of the reference stations. The scenarios with 4 reference stations show more unstable RMS values than those with more reference stations. With an increased number

of reference stations the RMS is reduced in most case.

Some stations seem to perform systematically worse or better than others like, e.g., DINS (‘◦’ in Figure 4.20) and ZIER (‘▷’ in Figure 4.20). In the following, some specific situations were analyzed exemplarily in detail and the possible error sources were discussed. In the scenario M2 the RMS values are larger than those in M4. The reason could be that in M2 the 4 reference stations have 3 different antenna types (**Table 4.5**); whereas the 4 reference stations in M4 have the same antenna type as the test stations (**Table 4.6**). In addition, the reference station MOUS has a cut-off angle of 10°, while other reference and test stations have a cut-off angle of 0°. In the data processing the observations with elevations larger than 7° are used. For the assumed SF station the converted observations between elevations of 7° and 10° use the ionospheric correction from the three stations, while the converted observations above 10° elevation have four reference stations. The inconsistent ionospheric corrections may corrupt the ZTD parameter.

Station name	Antenna type		Cut-off angle [°]
BOUX	ASH701945B_M	NONE	0
COLM	ASH701945B_M	NONE	0
1398	LEIAT303	LEIC	0
MOUS	LEIAX1202GG	NONE	10

Table 4.5: The reference stations in the scenario M2 have three different antenna types, the elevation cut-off angle of the station MOUS is 10°.

Station name	Antenna type		Cut-off angle [°]
BOUX	ASH701945B_M	NONE	0
COLM	ASH701945B_M	NONE	0
GAGG	ASH701945B_M	NONE	0
PEXO	ASH701945B_M	NONE	0

Table 4.6: The reference stations in the scenario M4 have the same antenna type; all the stations have the same cut-off angle.

There are two identical reference stations BOUX and COLM in M2 and M4, both stations equipped with the antenna type ASH701945B_M. In two other scenarios, M3 and M5, the reference stations 1398 and MOUS of M2 were replaced with the reference stations GAGG and PEXO. The RMS values in M3 and M5 are significantly smaller than in the M2 scenario but still larger than in the M4 scenario, probably because the antenna types of the reference stations are not identical. The 10° cut-off angle at the reference station MOUS causes the large RMS of the ZTD differences in M2.

The RMS values of the test station DINS are almost always larger than all other test stations in the 24 densification scenarios. The reference stations for the ionospheric correction are the same for all test stations; the ZTD errors of the station DINS should therefore be caused by a station-specific effect. To identify this effect the residual stacking map of the station DINS is generated in **Figure 4.21** left panel (Fuhrmann et al., 2010); the residuals of the real DF data from DOY 220 to 229 in 2007 are used, which were averaged using a sinusoidal projection for azimuth and elevation in a 1° ×

1° grid. The stacking map shows signal obstruction and multi-path effects in the west of the station. Since the obstruction and multi-path effects can be found at elevations up to about 30°, the \tilde{L}_2 observations can be very different to the observed L_2 observations. In addition, the lack of observations in the western direction disrupts the ZTD parameter estimation.

Similar to the DINS the stacking map of the station DACH (‘□’ in Figure 4.20) was checked. The station shows also large RMS in **Figure 4.20**. The stacking map of DACH shows obvious multi-path effects up to an elevation of 30° (**Figure 4.21** right panel), i.e., strong periodical variations in the residuals.

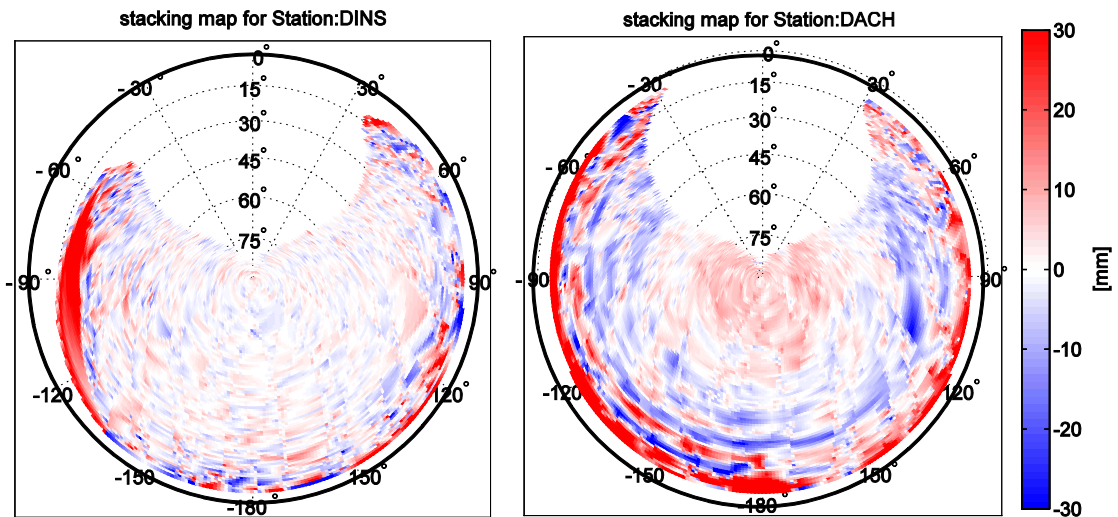


Figure 4.21: The stacking map of the stations DINS (left panel) and DACH (right panel), the color indicates the amplitude of the mean residual after the data processing (DOY 220-229 in 2007).

In the group ‘large’, i.e., the scenario A1 (88km/4ref) one reference station was missing for five days and only a few ZTD parameters of A1 were estimated (**Figure 4.22**). Its ZTD RMS is the largest of the 24 scenarios. One ZTD parameter is estimated for a 15 minute interval, the total number of ZTDs for the 10 days from one station is therefore 960. To retrieve all ZTDs more reference stations should be used. With an increasing number of reference stations in group A the RMS values decrease rapidly, and the number of the estimated ZTDs increases accordingly.

Compared to the ‘small’ and ‘middle’ scenarios the RMS values of the ‘large’ scenario group are larger. One reason could be that in the ‘large’ group the small scale ionospheric fluctuations cannot be modeled as well as in other two groups.

In **Figure 4.22** the number of estimated ZTD from SF data shows the reliability of the SEID method in the different scenarios. In the scenario M1 (61km/4ref) the reference station HOMM was missing on DOY 221 and 222; as a result the SEID could not generate \tilde{L}_2 and \tilde{P}_2 successfully for the assumed SF stations. More reference stations improve the reliability of estimating ZTDs from the SF data. In the scenario group ‘large’ the ZTDs could not be estimated reliably from the SF data with less than 6 reference stations. Therefore, more than 5 reference stations should be considered in practice for retrieving ZTDs from SF data using the SEID method.

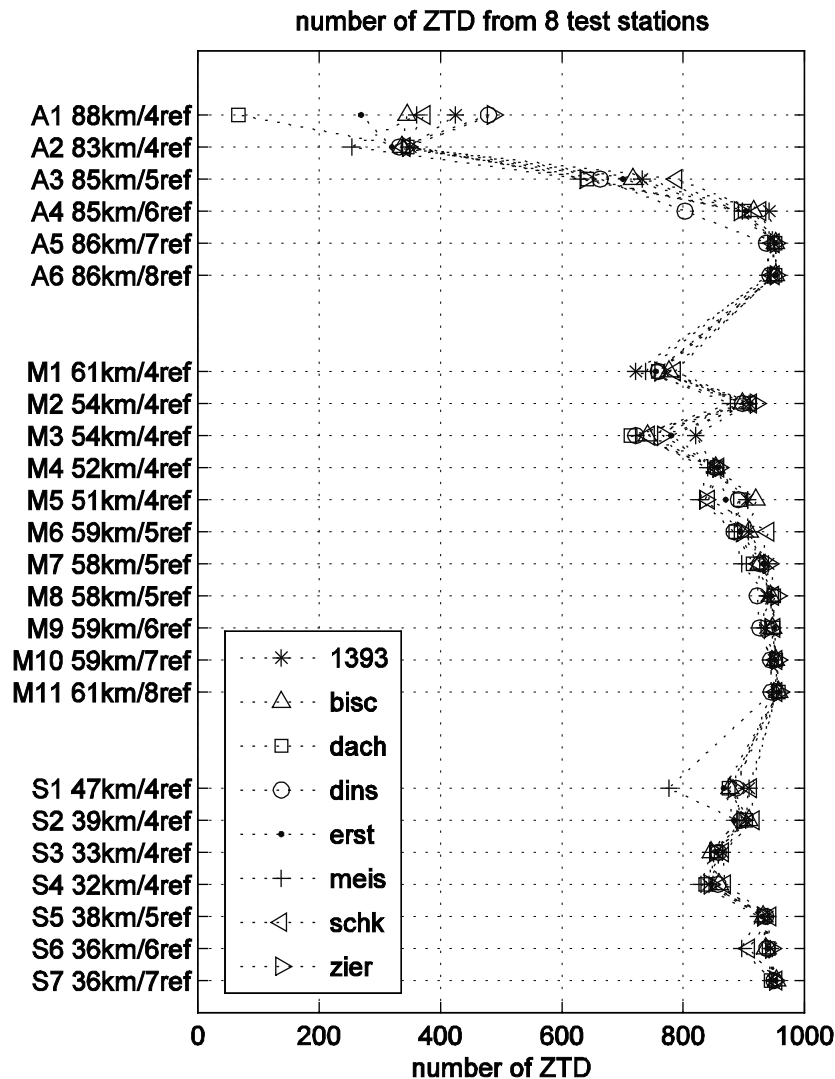


Figure 4.22: Numbers of the estimated ZTDs from the SF data for each test station in the 24 densification scenarios. The Y-axis shows the densification scenarios with the number of reference stations and the average distance from the test stations to the references stations. The X-axis shows the number of ZTDs estimated.

In the group ‘large’ the biases of the ZTD differences of the last three scenarios grow from 2 mm to 3 mm (**Figure 4.23**). The ZTD bias increases slightly with the number of reference stations. In contrary, the RMS values decreased. Because the dL_4 observation is only partly modeled in such large densification scenarios, the remaining ionospheric errors are absorbed by the ZTD parameters. The ZTDs retrieved from SF data have positive biases as compared to those retrieved from DF data. More reference stations can reduce the effects of ionospheric observations corrupted by large noise, multipath effects and data gaps. The retrieved ZTDs from the SF data converted with more reference stations have better accuracy. The other two groups show no significant trend of ZTD biases. To avoid this type of bias the mean distance of the SF station to the reference station should be kept smaller than 80 km.

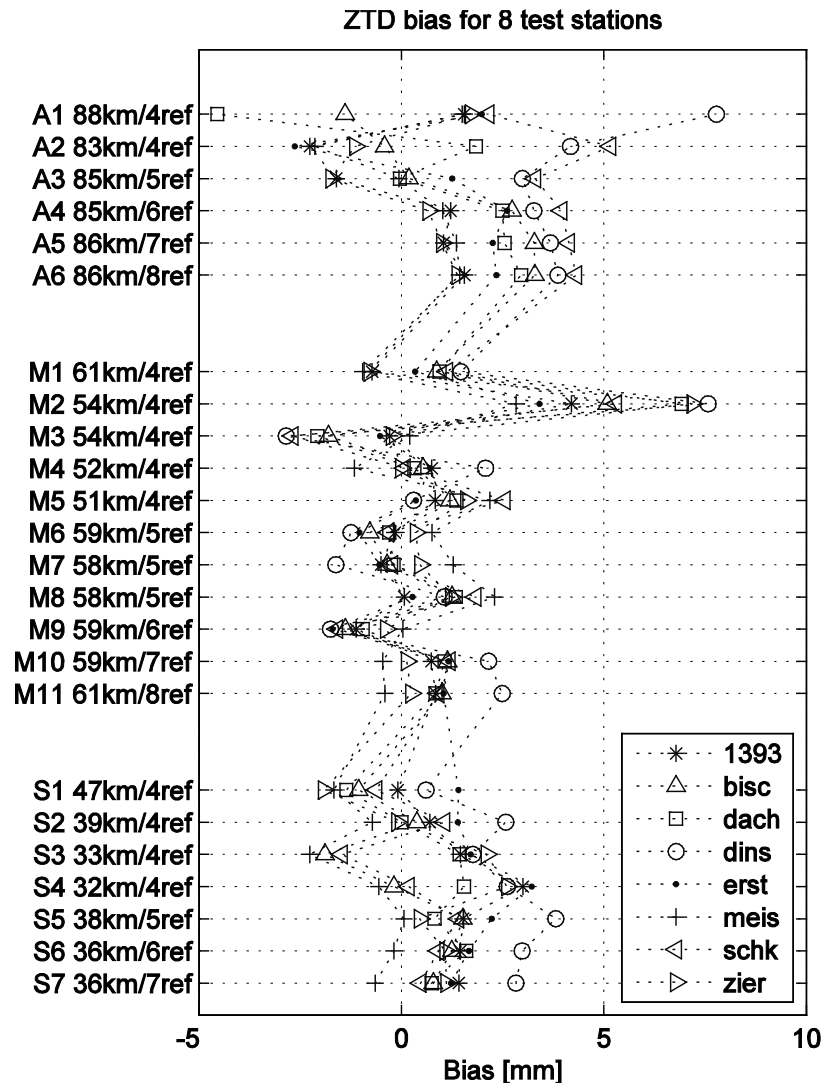


Figure 4.23: Biases of the ZTD differences for each test station in the 24 densification scenarios. The Y-axis shows the densification scenarios with the number of reference stations and average distances from the test stations to reference stations. The X-axis shows the bias in the ZTD differences.

Conclusion

24 densification scenarios with different reference station densities were defined and investigated in order to study the accuracy and reliability which can be obtained for retrieving ZTDs from SF data using the SEID model. The RMS of the ZTD differences increases with growing reference station separation, while the reliability increases with a growing number of reference stations.

The results verify that ZTDs with an RMS better than 6 mm can be obtained from SF data, if the average inter-station distance between the reference stations and the SF station is below 60 km. Inter-station distances above 80 km can lead to a positive ZTD bias. More than 6 reference stations should be available to get reliable ZTD estimates.

4.3 Observation of MSTID with dL_4

In the previous section it was shown that dL_4 can be interpolated with high-precision from small GPS networks. As dL_4 is proportional to the STEC variation $d\text{STEC}$, it is possible to monitor ionospheric variations with dL_4 maps from a large GPS network.

The Medium-Scale Traveling Ionospheric Disturbances (MSTIDs) are wave-like perturbations of the ionospheric plasma, which cause the most common ionospheric disturbances in mid-latitude regions. Generally the MSTIDs have velocities of several hundred meters per second and wavelengths of several hundred kilometers (Davies, 1990). They make it difficult to resolve ambiguities of SF and DF data even on baselines shorter than 10 km. Coordinate errors from SF data can exceed 10 ppm of the baseline length (Wanninger, 1995). Here, the possibility of detecting and modeling MSTIDs over Germany with dL_4 observations is shown.

4.3.1 Estimating the parameters of MSTID

Generally, a MSTID can be approximated by a planar longitudinal traveling wave that propagates in an ionospheric patch of the network of IPPs associated to a given satellite (Hocke and Schlegel, 1996; Memarzadeh, 2009). For a planar MSTID wave the amplitude depends on position. The wave equation can be described by:

$$A(t, \mathbf{r}) = A_0 \sin(\omega t - \mathbf{k} \cdot \mathbf{r} + \varphi_0), \quad (4.27)$$

where $A(t, \mathbf{r})$ is the STEC value of a MSTID wave at time t and position \mathbf{r} ; A_0 is the amplitude of the MSTID wave; ω is the angular frequency of the MSTID; \mathbf{k} is the wave vector; and φ_0 is the phase shift. The STEC variation due to a MSTID wave is given as total derivative:

$$\begin{aligned} dA(t, \mathbf{r}) &= \frac{\partial A}{\partial t} dt + \frac{\partial A}{\partial \mathbf{r}} d\mathbf{r} \\ &= A_0 \left[\omega \cos(\omega t - \mathbf{k} \cdot \mathbf{r}) dt - \mathbf{k} \cos(\omega t - \mathbf{k} \cdot \mathbf{r}) d\mathbf{r} \right] \\ &= A_0 (\omega \cdot dt - \mathbf{k} \cdot d\mathbf{r}) \cdot \cos(\omega t - \mathbf{k} \cdot \mathbf{r}). \end{aligned} \quad (4.28)$$

$dA(t, \mathbf{r})$ describes the STEC variation after a short period of time dt and a small displacement $d\mathbf{r}$. For two subsequently observed epochs dt and $d\mathbf{r}$ are identical for all IPPs from a regional GPS network. The term $A_0 (\omega \cdot dt - \mathbf{k} \cdot d\mathbf{r})$ is the amplitude of the $d\text{STEC}$ value of the MSTID wave (between 0-2 times A_0 , that depends on the velocity of the wave, the velocity of the satellite and the sampling rate). $dA(t, \mathbf{r})$ is a plane wave with the same frequency and wavelength as the original MSTID wave, but with a phase shifted by $\pi/2$.

In **Figure 4.24** two $d\text{STEC}$ profiles of a MSTID wave are shown. It is assumed that the wave has a westward motion with an angular frequency of ω , and the IPP has an eastward velocity of V_{IPP} . At time t the wave and satellite are plotted with a solid line; after a short time dt the wave and satellite are plotted with a dashed line. The total variation $d\text{STEC}$ of the STEC is dependent on the motion of the wave and the satellite.

When the wave has the same velocity as the IPP, no signature of the wave can be detected.

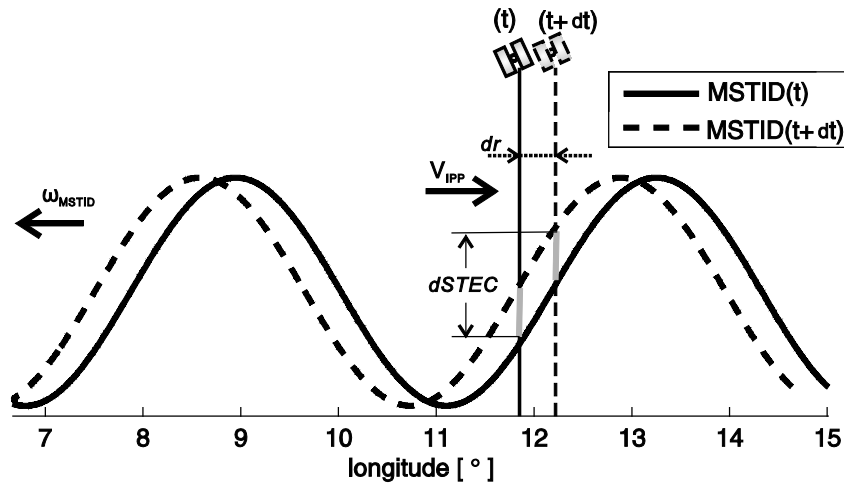


Figure 4.24: The schema of the $dSTEC$ variation caused by a longitudinal MSTID wave: the solid sinus wavelike line is a STEC profile of a MSTID wave at time t ; ω is the angular frequency of the MSTID; the dashed sinus wavelike line is the STEC profile at time $t + dt$; dr is the IPP displacement caused by the satellite motion in time dt .

To study the $dSTEC$ pattern more than 300 DF GPS stations in and near Germany are used (**Figure 4.25**). The dL_4 observations from the satellite PRN 9 of DOY 270 in 2009 are converted to $dSTEC$ values using the function (1 TECU \approx 10.5 cm at L_4):

$$dSTEC = \frac{dL_4}{-\alpha \cdot \left(\frac{1}{f_1^2} - \frac{1}{f_2^2} \right)}. \quad (4.29)$$

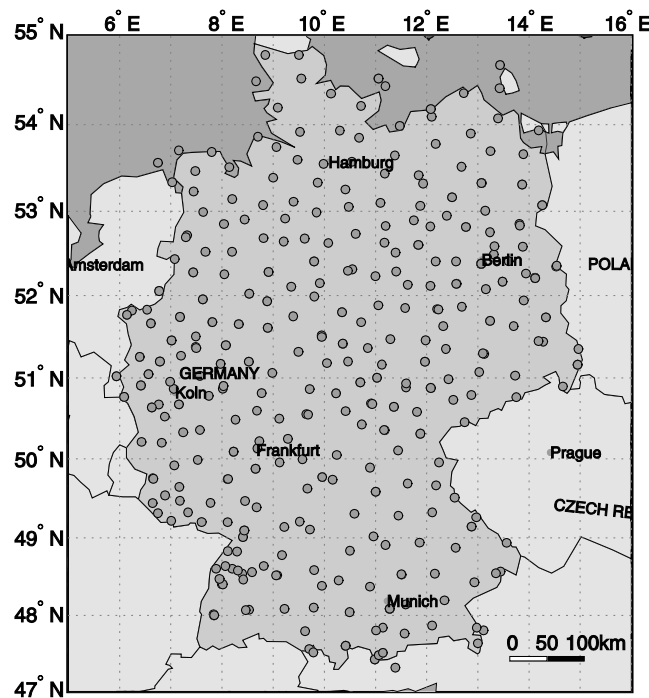


Figure 4.25: DF GPS stations (most are SAPOS stations), which are used to generate dL_4 maps.

Firstly, the IPPs of all the DF stations for the satellite PRN 9 are calculated for each epoch. To obtain homogeneous $d\text{STEC}$ maps the observed dL_4 data are interpolated by Delaunay triangulation. A Delaunay triangle network is generated (**Figure 4.26** right panel) and the corresponding dL_4 observations are interpolated using the linear interpolation method (described in **Figure 4.9**).

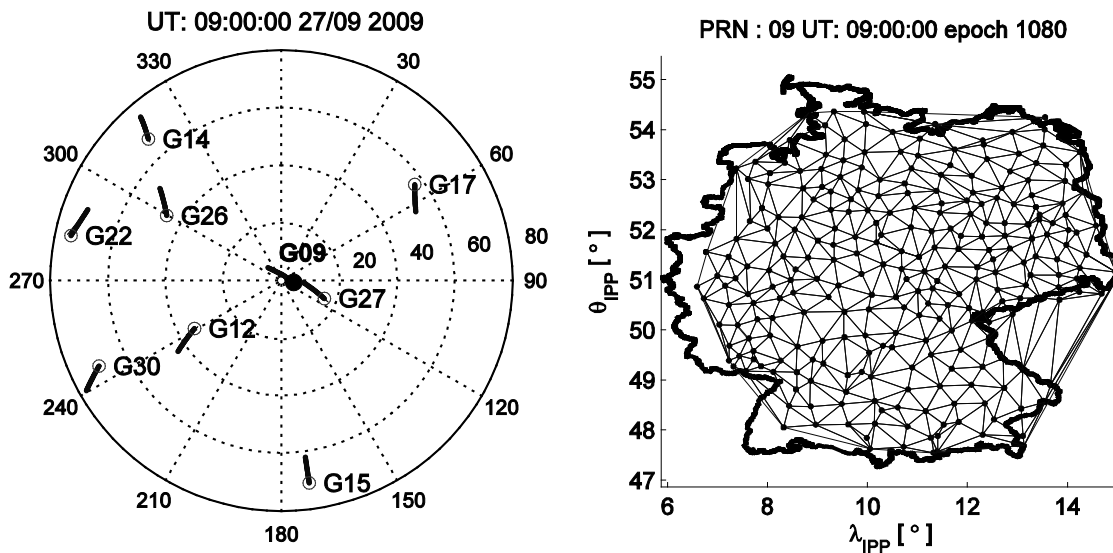


Figure 4.26: Directional tracks of the satellites labeled by satellite number at the end of each track for UTC 09:00:00 (left panel) on September 27th, 2009 (DOY 270). On the single layer a Delaunay triangulation network is generated associated to the IPPs of the reference stations for the satellite PRN 09. Each point is the location of an IPP on the single layer.

Two consecutive $d\text{STEC}$ maps over Germany are compared for 09:00:00 UT (11:00:00 AM, local time, **Figure 4.27** left panel) and 09:03:30 UT (11:03:30 am, local time, **Figure 4.27** right panel) on September 27th, 2009 (DOY 270). The elevation of satellite PRN 9 was about 85° (**Figure 4.26** left panel). The GPS satellite PRN27 was very close to PRN 9, and observed a similar structure of the MSTID as PRN 9. The MSTID wave moving from East to West across Germany can be observed. To show the wave form two $d\text{STEC}$ profiles (bottom panel) are generated at latitude of 51° , where the $d\text{STEC}$ s vary between 0 and 0.08 TECU (corresponding to 0 – 8.4 mm in L_4). In **Figure 4.28** the $d\text{STEC}$ profiles are generated from latitude 48° to 54° with a 1° interval. For better presentation each profile is shifted by 0.04 TECU.

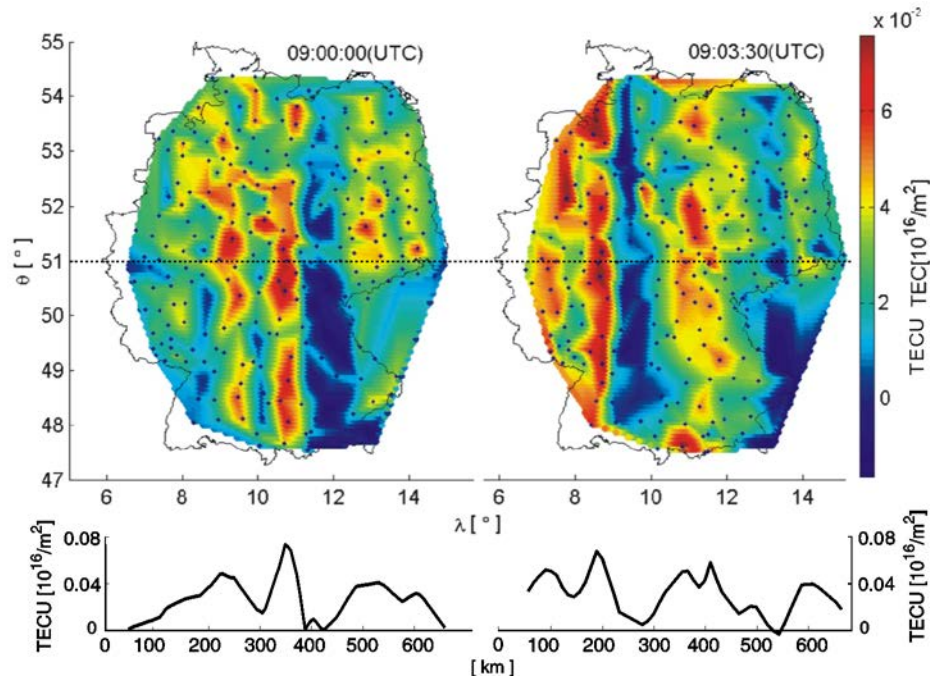


Figure 4.27: *dSTEC* distribution for GPS satellite PRN 9 on the single layer for one epoch of DOY 270 in year 2009. The dark blue dots are the intercept pierce points of the line-of-sight with the ionospheric layer at 350 km. Two *dSTEC* profiles (bottom panel) are generated at a latitude of 51° according to the dashed line in the top panel.

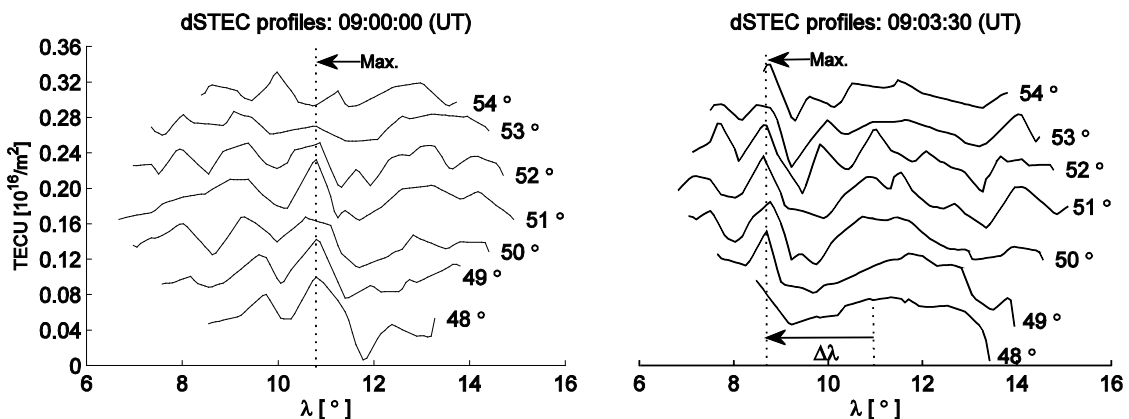


Figure 4.28: *dSTEC* profiles are generated from 48° to 54° latitude with a 1° interval according to the top panel of **Figure 4.27**.

The two profiles at 51° latitude are longer than those at other latitudes. To estimate the velocity of the MSTID motion the correlation coefficients $R_{Corr.}$ of the two profiles are calculated (**Figure 4.29** top panel) with:

$$R_{Corr.}(m) = \frac{1}{N} \sum_{n=1}^{N-m+1} y(n)x(n+m-1), \quad (4.30)$$

where y and x are the *dSTEC* profile at 09:00:00 and 09:03:30(UT), respectively; N is the record length. The maximum correlation coefficient is 0.86 at $\Delta\lambda = 2.025^\circ$. After 3.5 minutes the MSTID wave moved 2.025° westwards. In the bottom panel of **Figure 4.29** the *dSTEC* profile at 09:03:30 (UT) is shifted 2.025° eastwards, which is plotted (dashed line) together with the profiles at 09:00:00 (UT) (solid line). The variation of both profiles is very similar.

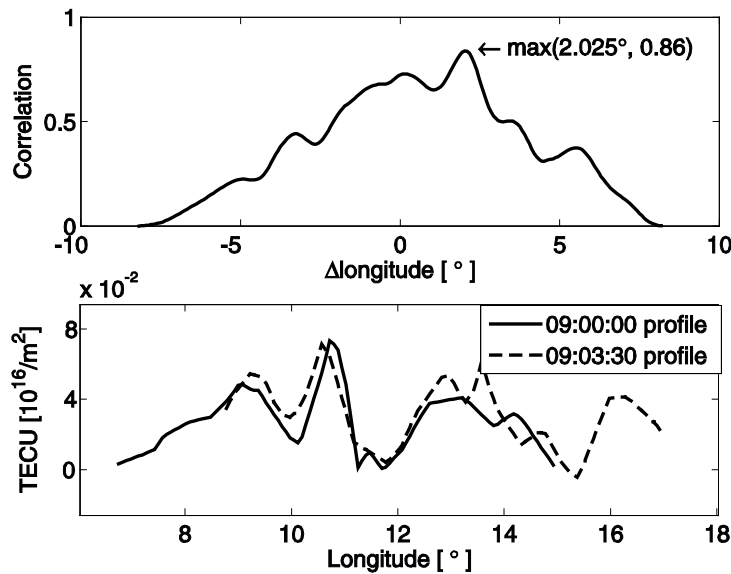


Figure 4.29: The correlation of the two $dSTECH$ profiles at 51° latitude (top); the $dSTECH$ profile at 09:00:00 (UT) and the $dSTECH$ profile at 09:03:30 (UT) shifted westward by 2.025° (bottom).

A displacement of 2.025° at latitude of 51° is equivalent to a distance of about 150 km on the single layer. With the time interval of 3.5 minutes between the two $dSTECH$ profiles the velocity of the MSTID wave can be estimated to about 700 m/sec on the single layer.

Furthermore, the power spectrum of the two profiles was analyzed (**Figure 4.30**) using a Fourier transformation, which shows that the power maximum of both profiles is at the same wavelength of 4.087° . This corresponds to a wavelength of the MSTID wave of about 300 km the single layer at 350 km height. With the velocity of the wave the period can be calculated to about 7 minutes. Regarding the velocity of the IPP V_{IPP} (maximum about 70 m/sec near zenith) the factor of $\omega \cdot dt - \mathbf{k} \cdot d\mathbf{r}$ is about 0.5. The amplitude of $dSTECH$ is about 0.02 TECU, and the original MSTID wave has an amplitude of about 0.04 TECU (about 6.4 mm effect in L_1)

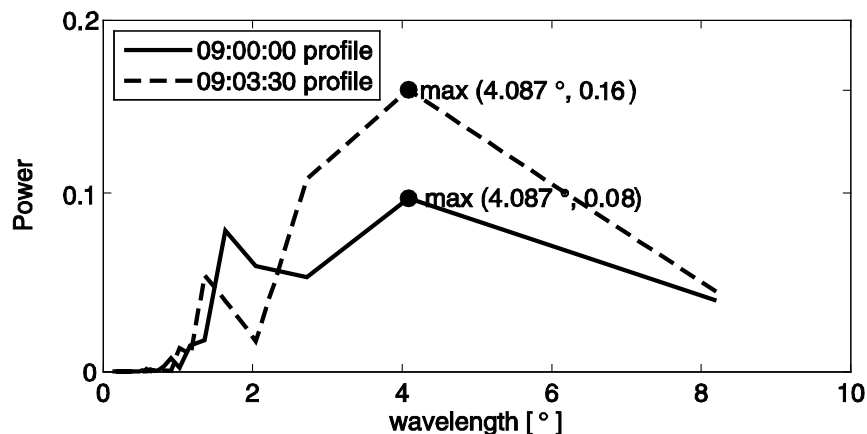


Figure 4.30: The spectral analysis of both profiles from **Figure 4.29**, both maximum appear at the same wavelength of 4.087° .

It was therefore possible to estimate the frequency, the wavelength, the phase velocity and the amplitude of the MSTID wave by analyzing dL_4 data from a large dense GPS network.

4.3.2 Comparison with TEC-DEIN

Using GPS data of the IGS, the EPN⁵, and EPN regional network, TEC-DEIN⁶ maps of the European region of -10° to 30° east and 35° to 70° north are generated by Tsugawa (<http://www2.nict.go.jp/y/y223/member/tsugawa/TEC-DEIN/>). The maps detrended with one-hour window, have a spatial resolution of $0.75^{\circ} \times 0.75^{\circ}$ in latitude and longitude ($0.15^{\circ} \times 0.15^{\circ}$ with 5×5 pixel smoothing) and a temporal resolution of 30 seconds, which is smoothed temporally with a running average of 10 minutes (Tsugawa et al., 2007).

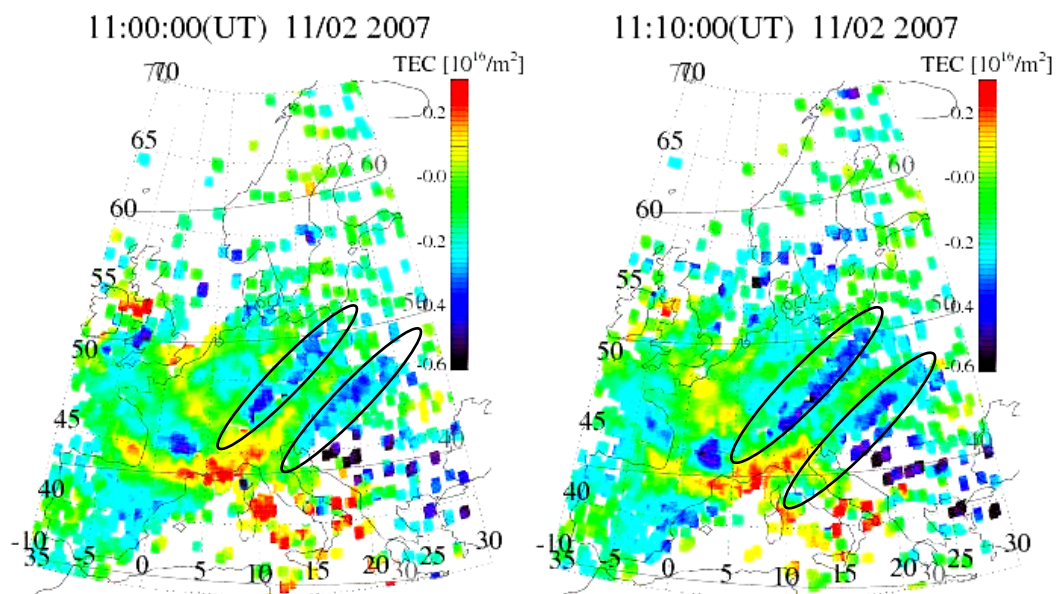


Figure 4.31: The detrended TEC-DEIN maps for Europe at 11:00:00 (UT) (left panel) and 11:10:00 (UT) (right panel) on Nov. 02, 2007; two wave minima are marked with the ellipses.

In **Figure 4.31** two detrended TEC-DEIN maps with a time separation of 10 minutes show MSTID waves over Europe. The ellipses show that the MSTID waves were located in south-eastern Europe. The wave front reached from north-east to south-west and the wave propagated in south-eastern direction. Within 10 minutes the wave did not change significantly. The same MSTID patterns are to be found in the dL_4 maps.

The left panel of **Figure 4.32** shows directional tracks of the visible satellites at UT 11:10:00 on Nov. 02, 2007; after 10 minutes the satellite G24 rose from south-east. In total 12 satellites were observed (**Figure 4.32** right panel). The satellites G09 and G24 in the south-eastern part of Europe observed patterns that could be attributed to the MSTID waves. The dL_4 maps for satellite G09 are shown in **Figure 4.33**.

⁵ EUREF Permanent Network

⁶ Total Electron Content - Data of European Integrated GPS Network

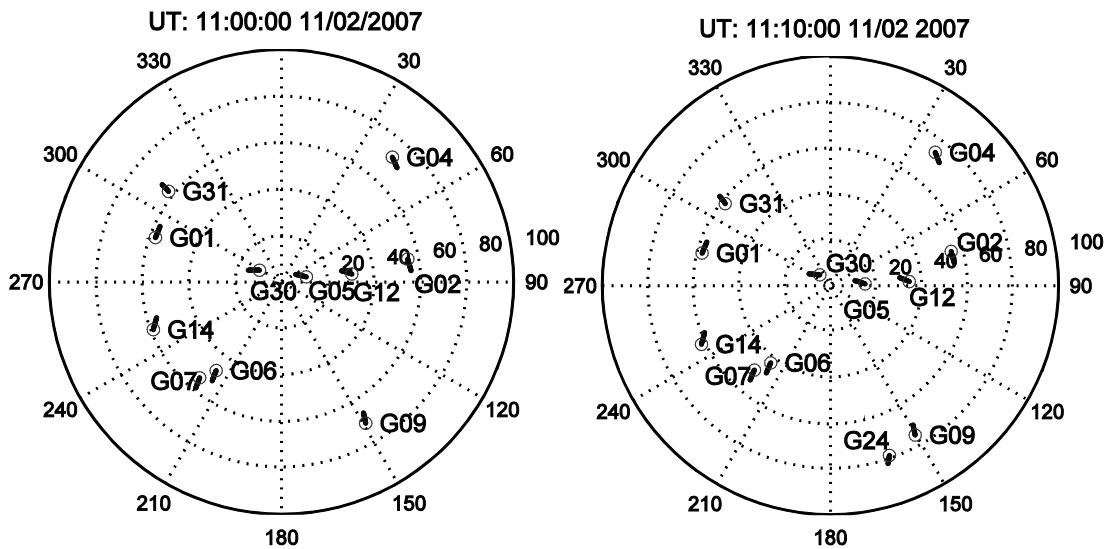


Figure 4.32: Directional tracks of the satellites labeled by satellite number at the end of each track for UTC 11:00:00 (left panel) and 11:10:00 (right panel) on Nov. 02, 2007 (DOY 306).

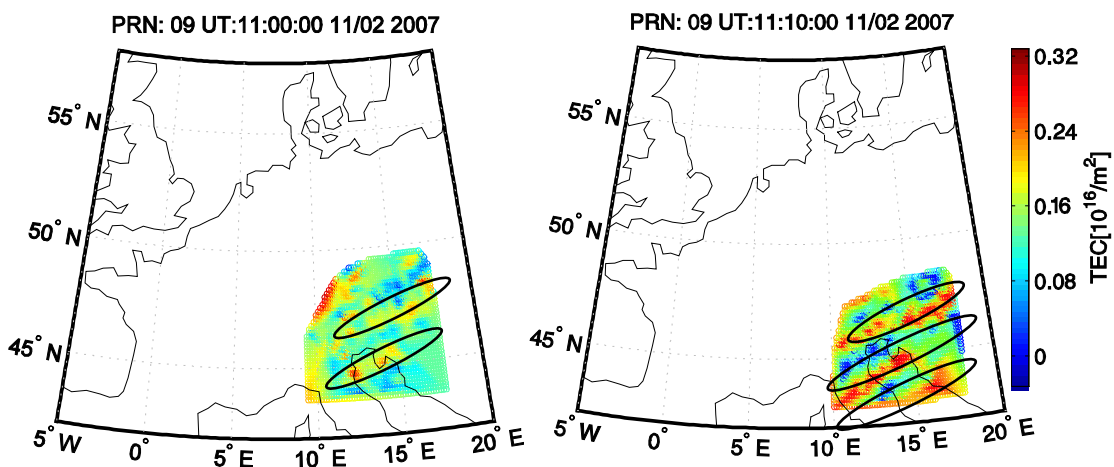


Figure 4.33: dL_4 map for satellite G09 at 11:00:00 (left panel) and 11:10:00 (right panel) on Nov. 02, 2007.

The two dL_4 maps of the satellite G09 show the same signatures of the MSTID wave. The location of the wave in the dL_4 maps are the same as in the detrended TEC-DEIN maps. The movement of the MSTID is slow within the 10 minutes. In addition, the wave front of the MSTID points in the same direction. However, the dL_4 amplitude of the MSTID cannot directly be compared with the MSTID amplitude from the detrended TEC-DEIN maps, since it depends on several factors, e.g., the time interval between epochs, the velocity of the MSTID and of the satellite. The dL_4 map for the satellite G24 shows a pattern that could be a MSTID structure. Its dL_4 amplitude is much larger than that from other satellites (**Figure 4.34**). It is worth to note that the maximum and minimum are not at the same location, this is mainly due to the fact that the satellite G24 moved northwestwards and satellite G09 moved in the opposite direction. As a result the $\omega \cdot dt - \mathbf{k} \cdot \mathbf{dr}$ factors of the two satellites are opposite for both dL_4 maps. The blue area in the dL_4 map of the satellite G24 appears red in the dL_4 map of the satellite G09.

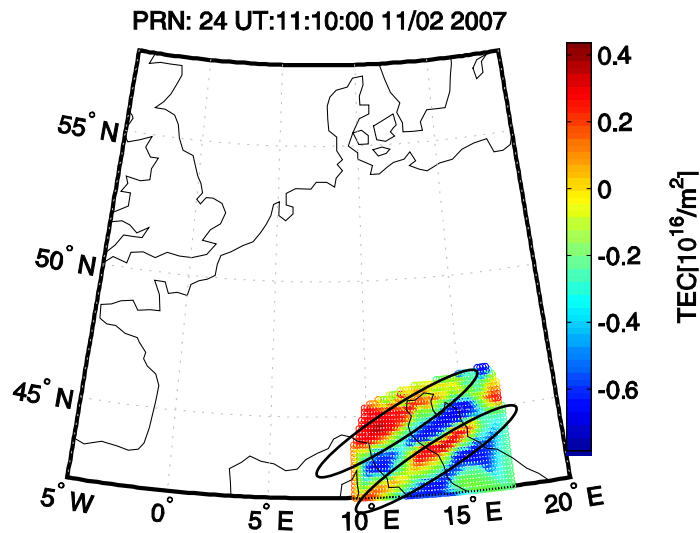


Figure 4.34: dL_4 map of the satellite G24 at 11:10:00 on Nov. 02, 2007.

The dL_4 maps of the satellites G09 and G24 show similar signatures of the MSTID wave as the detrended TEC-DEIN maps. The dL_4 maps can be a powerful new tool to investigate MSTIDs. Further work is needed to fully explore their relation, but this is out of the scope of this dissertation.

4.3.3 Interpolation error under MSTID

Under normal ionospheric conditions the epoch-differenced ionospheric delays can be modeled with an accuracy of about 5 mm (Deng et al., 2009). The SEID model uses a plane or low-order surface to model ionospheric variations between two epochs. However, under rapid ionospheric variations, e.g., MSTIDs, dL_4 observations cannot be modeled very well. To study the impact of such a situation the data in **Figure 4.15** are used. The \tilde{L}_2 observations of station 0527 are generated using 10 surrounding reference stations (**Figure 4.14**) and are compared with the real L_2 observations. **Figure 4.35** shows the differences between \tilde{L}_2 and real L_2 observations for satellite PRN 18. The L_2 differences vary up to 4 cm between 20:00:00 and 22:00:00, which might be caused by a MSTID event. Within this period the dL_4 observations from the 11 stations varied from -2 cm to 1 cm (**Figure 4.14**).

To show the ionosphere state, the dL_4 observations from 298 GPS stations in and near Germany are plotted for satellite PRN 18 in **Figure 4.36** at the epochs 20:46:30 and 21:06:30 on DOY 225 in 2007, which correspond to the two large errors A and B in **Figure 4.35**. The elevation of the observations was about 32° . The colors of the grid pixels indicate the $dSTE C$ values, which are interpolated from the three closest IPPs using a linear interpolation method described in Eq. (4.8). The circles in **Figure 4.36** indicate the IPPs locations of 11 test stations on the single layer.

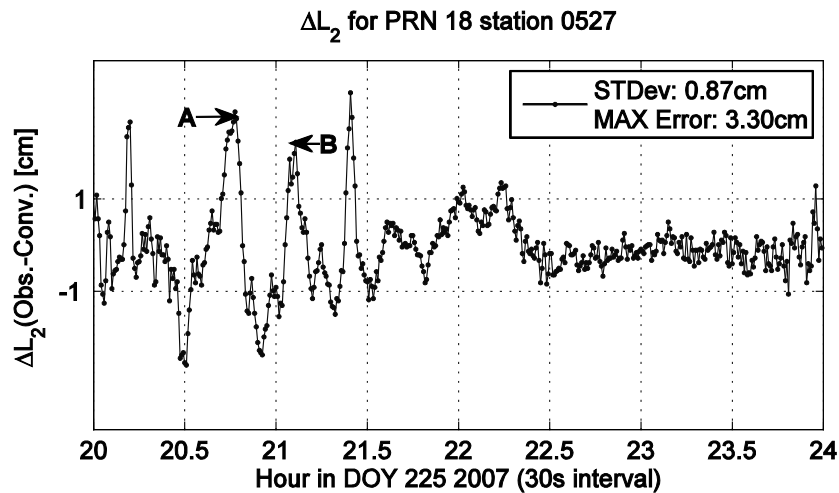


Figure 4.35: Differences between observed and converted L_2 observations of station 0527 (with the closest ten reference stations) for the GPS satellite PRN 18 on DOY 225 in 2007. A and B are two maximum errors.

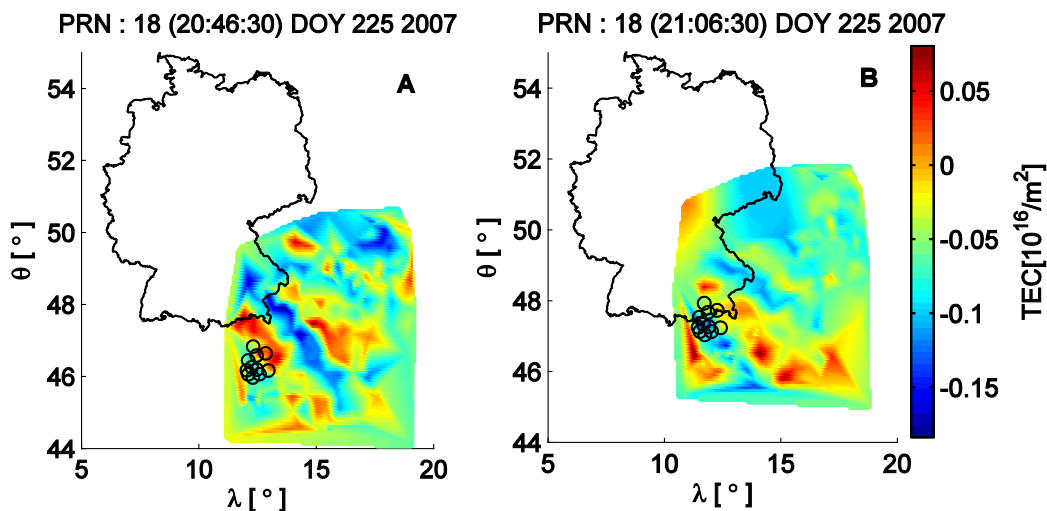


Figure 4.36: $dSTEC$ distribution for the GPS satellite PRN 18; the circles are IPP locations of the 11 test stations on the single layer.

Figure 4.36 shows that the $dSTEC$ observations varied from about -0.18 to 0.8 TECU during the MSTID wave, the movement of the wave is southwestward. Its wavelength is about 200 km. In both figures the IPPs of the 11 stations are located between blue (decreasing STEC) and red (increasing STEC) structures, where the STEC values reached a trough of a MSTID wave. The dL_4 observations from the ten reference stations were fitted to a plane with a diameter of about 100 km, which is half of the MSTID wavelength. Using a simple plane the dL_4 observations are difficult to be modeled accurately.

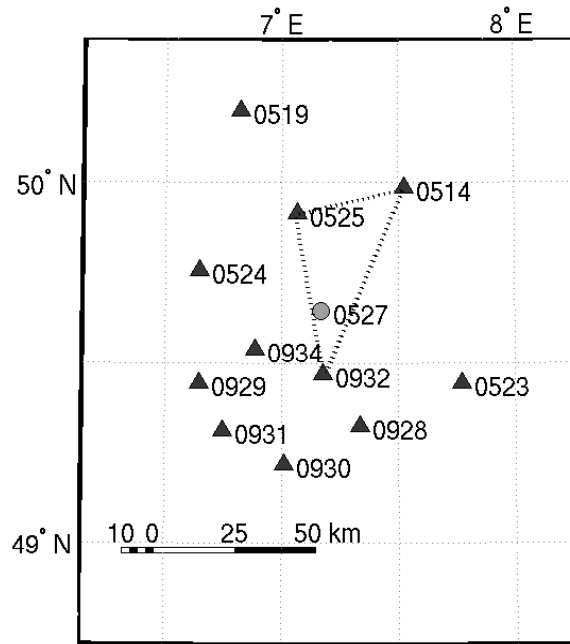


Figure 4.37: The sub-network is used to study the impact of the MSTID on the interpolation error. Station 0527 is assumed to be a SF stations.

The differences between \tilde{L}_2 (with ten reference stations) and L_2 observations of the station 0527 show oscillations during the MSTID event. To reduce the oscillation effects a smaller reference network should be used. The three closest stations 0514, 0525 and 0932 form a smaller reference network with a separation of about 50 km (Figure 4.37).

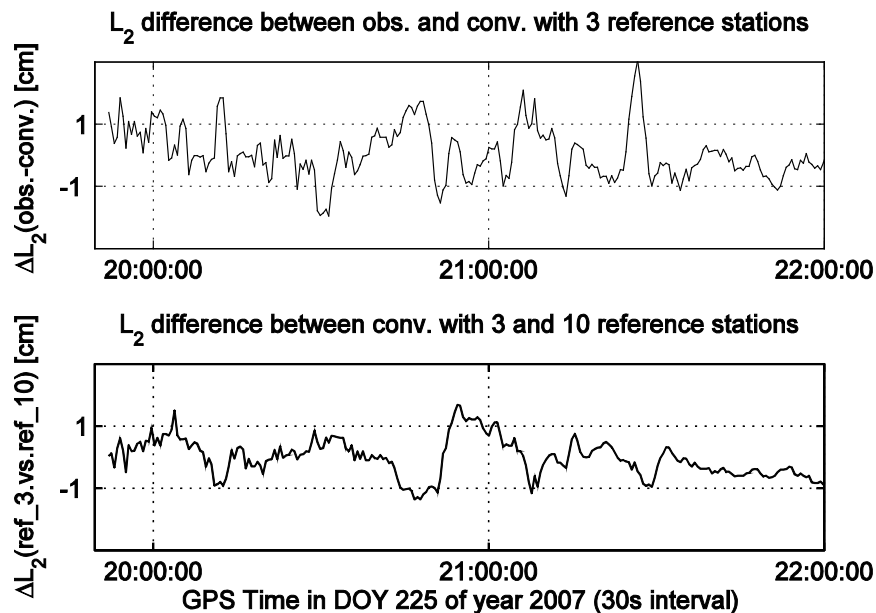


Figure 4.38: The differences between the observed and converted L_2 observations obtained with the three closest reference stations (top panel); the difference between two converted L_2 observations obtained with the three and the ten closest reference stations (bottom panel).

The L_2 differences of for the satellite PRN 18 are plotted at the top panel of

Figure 4.38, the bias is removed. The standard deviation and the maximum error are 0.61 cm and 2.91 cm respectively. The largest differences appear between 20:00:00 and 22:00:00, where the MSTID is observed from the reference stations. In such a situation it is still difficult to interpolate dL_4 precisely. The bottom panel of **Figure 4.38** shows the differences between the \tilde{L}_2 observations converted with three reference stations and those with ten reference stations. The \tilde{L}_2 errors caused by the MSTID are reduced using smaller reference network.

To study the interpolation error caused by the MSTID the number of the reference stations is increased from three to ten (**Table 4.7**):

Group name	reference stations
G1	0525 0932 0934
G2	0525 0932 0514
G3	0523 0931 0919
G4	0525 0514 0932 0527
G5	0525 0514 0932 0934
G6	0525 0514 0932 0934 0527
G7	0525 0514 0932 0934 0524
G8	0525 0514 0932 0934 0524 0523
G9	0525 0514 0932 0934 0524 0523 0928
G10	0525 0514 0932 0934 0524 0523 0928 0929
G11	0525 0514 0932 0934 0524 0523 0928 0929 0931
G12	0525 0514 0932 0934 0524 0523 0929 0928 0931 0930

Table 4.7: The 12 reference networks with the names of the reference stations.

All test results can be found in the Appendix. **Figure 4.39** shows the standard deviations and maximum errors of the L_2 differences for the 12 densification reference networks. When the station 0527 is included as a reference station, the error caused by the MSTID wave is about 4~5 mm, which is smaller than found in the other tests. The results indicate that the dL_4 variations caused by the MSTID wave cannot be modeled well even with reference stations with a separation of 50 km.

Reference stations	0525	0514	0932	0527	
Post-fit residuals [mm]	1.0	0.2	1.9	3.1	
Reference stations	0525	0514	0932	0934	0527
Post-fit residuals [mm]	1.3	0.7	2.0	4.9	3.1

Table 4.8: The standard deviation of the post-fit residual of the dL_4 observations for the reference groups with the station 0527.

For two densification groups, G4 and G6, with the station 0527 as a reference station, **Table 4.8** shows the statistics of the post-fit residuals of the dL_4 observations in millimeters. In the two groups the station 0514 has smaller standard deviation than other groups. The additional station 0934 does not improve the accuracy of the interpolation.

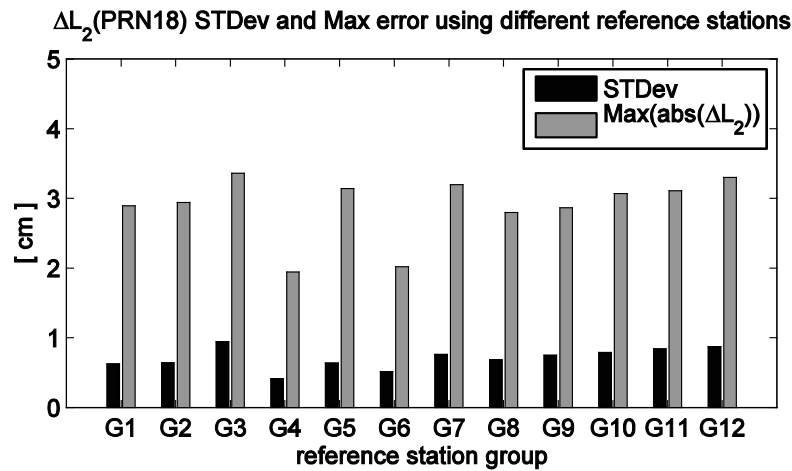


Figure 4.39: dL_2 statistics of the ten reference groups with increasing number of reference stations using a plane.

The dL_2 statistics of 10 groups with different reference stations show that the increased number of reference stations cannot reduce the error caused by the MSTID. The dL_4 observations during this strong MSTID event cannot be modeled with a plane very well. To improve the interpolation the linear model was extended to:

$$dL_4 = a_0 + a_1\lambda + a_2\theta + a_3\lambda\theta$$

and

$$(4.31)$$

$$dL_4 = a_0 + a_1\lambda + a_2\theta + a_3\lambda\theta + a_4\lambda^2 + a_5\theta^2.$$

Figure 4.40 and **Figure 4.41** show the results for the two extensions respectively. The interpolation errors caused by the MSTID event cannot be reduced significantly with the two low-order surfaces.

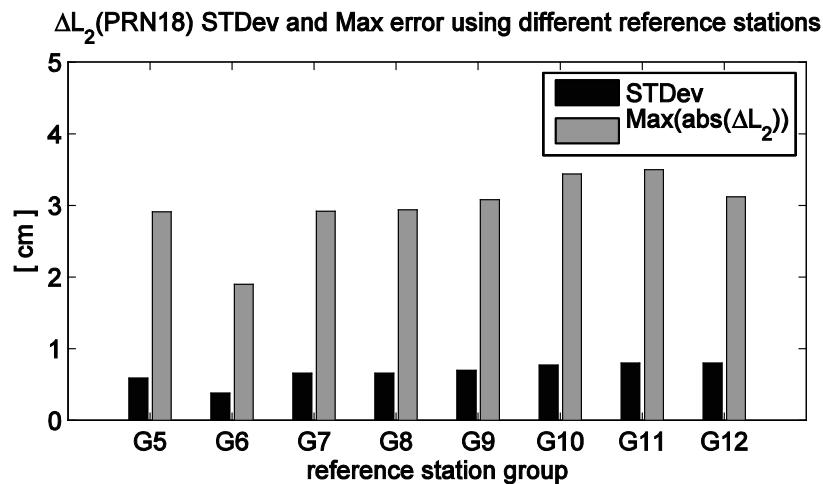


Figure 4.40: dL_2 statistics of eight groups with an increased number of reference stations (4 to 10 reference stations) using a hyperbolic paraboloid for interpolation.

However, in the data pre-processing or the data-cleaning of the EPOS such large errors can be identified, and excluded from the ZTD parameter estimation. Both, SF (\tilde{L}_2 are converted with 10 reference stations) and DF data of the station 0527 were processed using EPOS software. For the MSTID period the ZTDs retrieved from the converted DF data differ by only 2 mm from the ZTD retrieved from the real DF data.

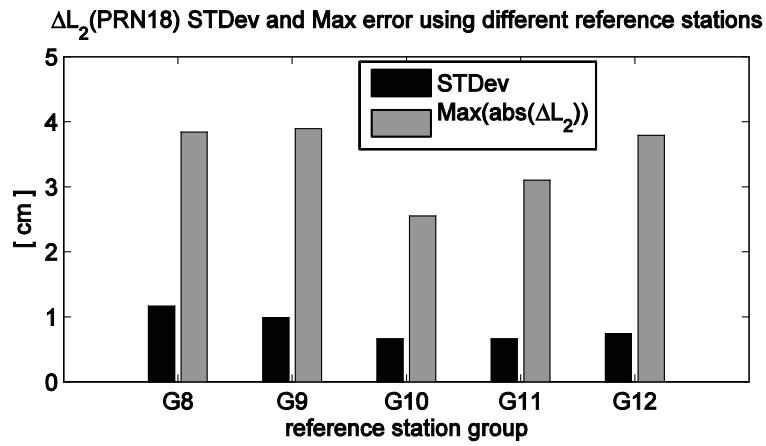


Figure 4.41: dL_2 statistics of five groups with an increased number of reference stations (6 to 10 reference stations) using a quadratic surface for interpolation.

5 Single frequency GPS analysis results and validations

In this chapter the results from two meteorological SF studies are given and discussed. In the first study GPS data from a small dense GPS network are analyzed. The dense GPS network was set up with 17 SF and DF receivers in Germany during the Lindenberg Upper-Air Method Inter-comparison (LUAMI) campaign between DOY 300 and 360 in 2008. In the second study the observations of a large geodetic network are used to simulate observations of SF receivers embedded in an existing DF network. The average inter-station distance of the DF stations is about 40 km. GPS data of 11 days (DOY 220 to 230 in 2007) were analyzed. The available tropospheric products from the SF data processing, e.g., ZTD STD and SWV are validated against the results from DF data, numerical weather models and a water vapor radiometer (WVR).

5.1 LUAMI single frequency analysis results

LUAMI was a campaign taking place at the Meteorological Observatory Lindenberg (MOL) of the German Weather Service (DWD) in Germany. The primary objective of the campaign was to improve the understanding of remote sensing and in-situ methods of measuring the basic atmospheric variables, with focus on humidity measurements.

5.1.1 LUAMI and the related GPS network

During LUAMI the suitability of various methods of measuring humidity was tested. The methods used in the campaign were classified into remote sensing, air-borne, and balloon sounding. Between 4th Nov and 22nd Nov 2008 the in-situ and remote sensing instruments were operated as continuously as possible to provide observations with large redundancy. In addition, the aerosol, clouds and water vapor over Lindenberg were measured at 17th and 18th October with two flights of the research aircraft Falcon of DLR (Deutsches Zentrum für Luft- und Raumfahrt). The aircraft was equipped with a Differential Absorption LIDAR. For the remote sensing study GFZ installed a small-scale network of 17 GPS receivers in the area around Lindenberg with a dimension of about 10 km x 15 km (**Figure 5.1** left panel). The LUAMI GPS network consisted of 6 SF stations with internet connection (red points), 7 SF stations without internet connection (blue points) and 2 DF stations with internet connection (yellow points). Together with two permanent GPS stations at Lindenberg 13 SF and 4 DF receivers provided ZTD and slant delay observations for about two months.

GPS network

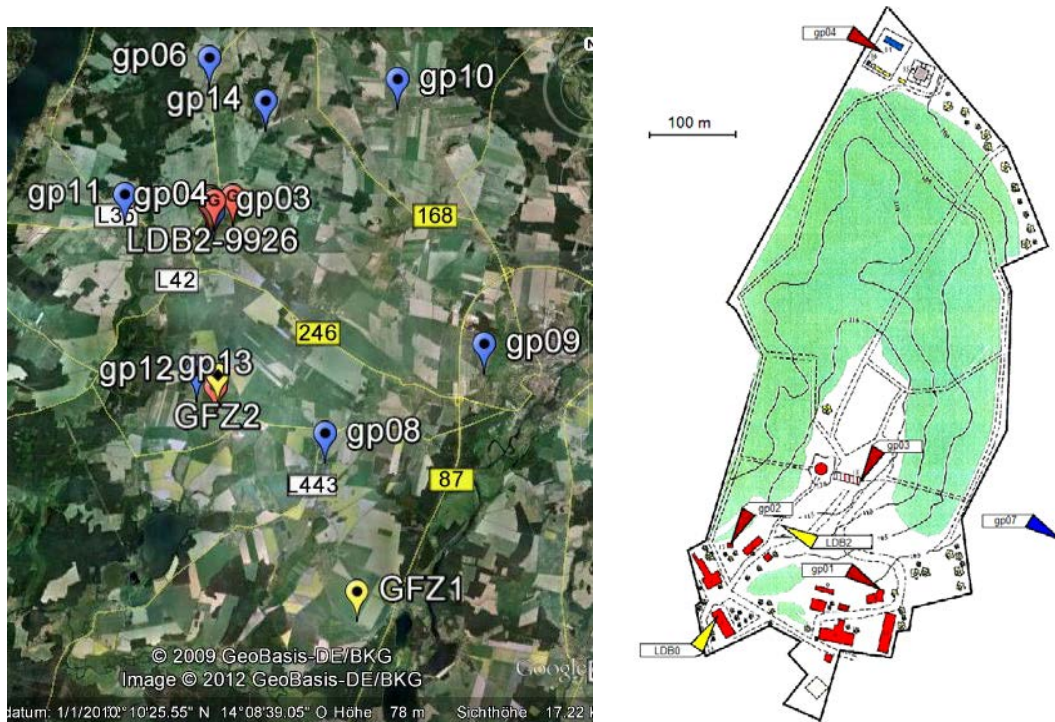


Figure 5.1: Left panel: LUAMI GPS network with 13 SF (blue and red marks) and 4 DF (yellow marks) stations. Right panel: Map of the Lindenberg observatory with 5 SF stations (4 online with red triangles, 1 offline with blue triangle) and 2 DF stations (online with yellow triangle).

To monitor the water vapor distribution during the LUAMI campaign, the GPS stations had to be placed in and near Lindenberg and operated continuously for the entire period. All the temporal stations were set up with visibility to GPS satellites as far as possible. To reduce the movement of the GPS antennas the GPS stations were established on stable devices or buildings. The power consumption of the SF receivers is rather low. However, they cannot run on battery power for one month. To operate the network for the entire campaign the SF GPS stations had to have permanent power supply. Most stations were set up in gardens of the DWD employees. 8 stations had access to the internet, and the received GPS data was transferred to GFZ each hour. The measured GPS data of the offline stations were stored on a mini-computer for subsequent computation. With two permanent DF GPS stations (LDB0 and LDB2) a total number of 7 stations were available within $300 \text{ m} \times 600 \text{ m}$ at the Meteorological Observatory Lindenberg (Figure 5.1, left panel). The hardware of the LUAMI GPS stations is listed in Table 5.1. The coordinates of the 17 stations are given in Table 5.2; the maximum height difference between the stations is about 85 meters between the station GP02 and the station GFZ2.

Name	Receiver		Antenna		L1/L2
GP01–GP13	NOVATEL	SMART-V1	NOVATEL	SMART-V1	L1
GFZ1	TRIMBLE	4000SSE	TRM14532.00	NONE	L1/L2
GFZ2	TRIMBLE	4000SSE	TRM14532.00	NONE	L1/L2
LDB0	AOA BENCHMARK ACT		ASH700936D_M	NONE	L1/L2
LDB2	JPS LEGACY		TPSCR3_GGD	CONE	L1/L2

Table 5.1: Hardware list of the LUAMI GPS stations.

Name	Longitude [°]	Latitude [°]	Height [m]
GP01	14.1198047	52.2080775	115.956
GP02	14.1199427	52.2096546	135.573
GP03	14.1215724	52.2086853	126.701
GP04	14.1287457	52.2097699	106.092
GP05	14.1228795	52.1663925	76.867
GP06	14.1191643	52.2429328	100.947
GP07	14.1214164	52.2060927	97.251
GP08	14.1645705	52.1532013	60.915
GP09	14.2239104	52.1727074	52.004
GP10	14.1990111	52.2372635	76.185
GP11	14.0868539	52.2101167	75.194
GP12	14.1147522	52.1679117	72.562
GP13	14.1223056	52.1647215	75.745
GFZ1	14.1228487	52.1670638	78.717
GFZ2	14.1787491	52.1147380	51.042
LDB0	14.1184748	52.2096260	120.623
LDB2	14.1209245	52.2091242	119.620

Table 5.2: Coordinate list of the LUAMI GPS stations in the IGS05 reference frame.

SF station

Figure 5.2 shows the hardware components of the SF stations: the SF GPS receiver NovAtel SMART-V1 with integrated antenna, a control mini-computer and an uninterruptible power supply (UPS). The mini-computer and the UPS are housed in a robust plastic box to protect the equipment against the environmental elements rain, dust and damage (**Figure 5.3**).

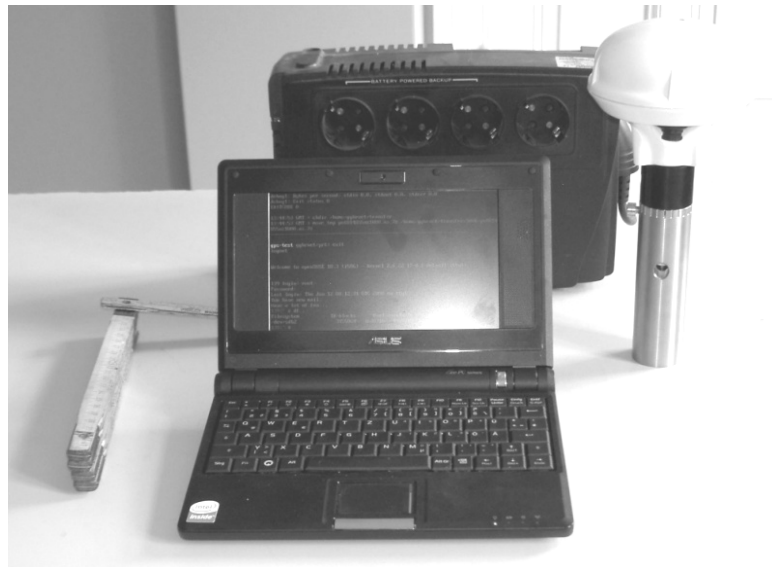


Figure 5.2: The hardware components of the LUAMI SF stations: GPS antenna with integrated receiver, a mini-computer and an uninterruptible power supply. The total cost is about 1,300 Euro (status 2008).

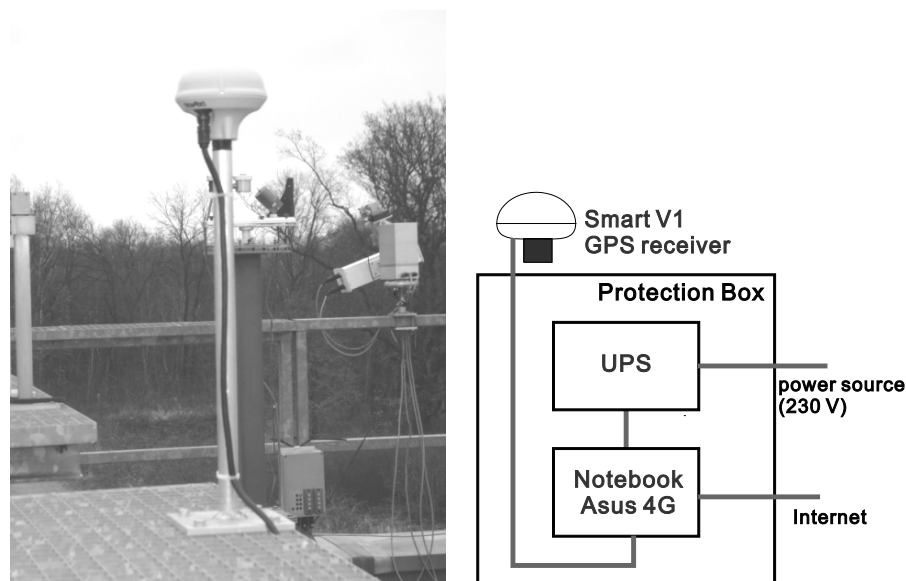


Figure 5.3: SF station (GP03) setup at Lindenberg (left panel); mini-computer and UPS housed in a robust plastic box (right panel).

A SUSE Linux system was installed on the mini-computers equipped with a 4 Gbyte solid state drive. After the system installation about 0.9 Gbyte free disk space was available, and was sufficient to store the received GPS data for the whole campaign. The mini-computer controlled and monitored the SF GPS receiver. The data sampling interval was 30 seconds, and an elevation cut-off angle of 5° was applied. Every hour a new data file was generated by the mini-computer and sent to a GFZ FTP server if the station had internet connection, otherwise the files were saved for post-processing. At GFZ the data files were first converted to standard RINEX files, and later saved on a data server.

Data set

The GPS receivers were installed in the time period between October 16 and November 5, 2008 (DOY 290-310). During the campaign (DOY 310-350) most of the receivers measured continuously (**Figure 5.4**). The data gaps of the SF stations were mostly caused by the interrupted connection between the GPS receiver and the mini-computer.

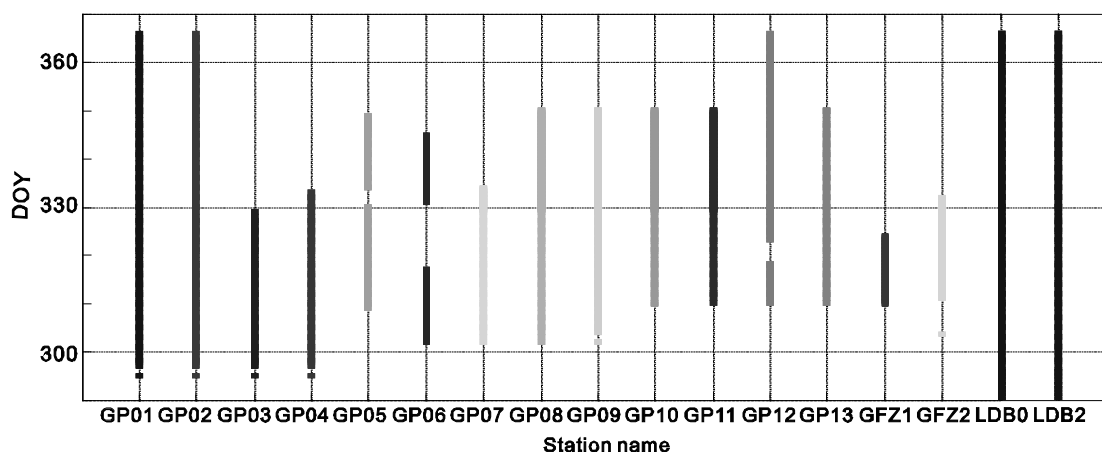


Figure 5.4: LUAMI GPS data collection from the 13 SF and 4 DF stations.

Reference stations

Before the data processing the received GPS data from the 13 SF stations were converted into DF data using the SEID model. The ionospheric corrections were generated from the 5 surrounding DF SAPOS reference stations, which have distances of about 52 km (**Figure 5.5**).

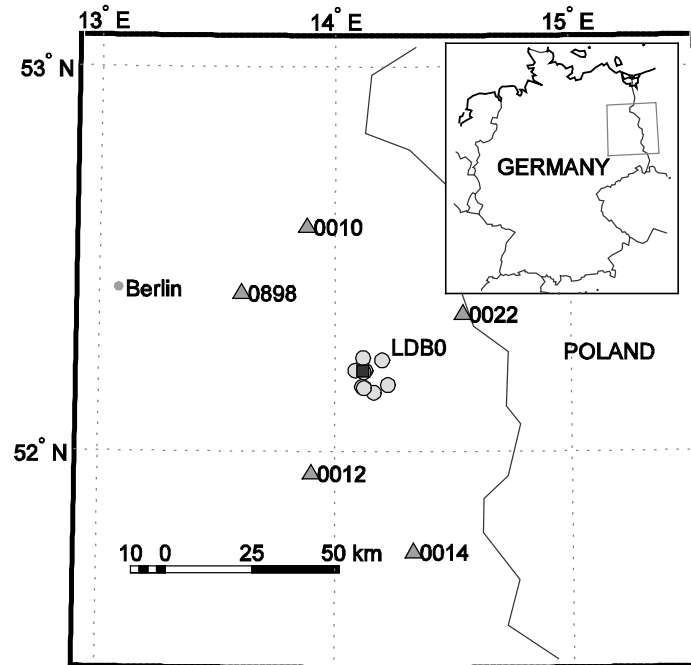


Figure 5.5: Five SAPOS stations (triangles) served as reference stations for the ionospheric correction; LDB0 (black diamond) is equipped with a DF receiver; the 13 SF stations are marked with circles.

The five reference stations are SAPOS stations, which are equipped with geodetic GPS receivers. The receiver and antenna types of the 5 stations are listed in **Table 5.3**. Three different antenna and receiver types were used within these five reference stations. The DF station LDB0 is operated by GFZ. In the study it is also processed like a SF station to test the accuracy of the ionospheric correction. Using the SEID model the ionospheric corrections were generated for the control station LDB0 and the other 13 SF stations. The L_2 and P_2 observations were generated, and the SF data was processed together with the DF data using the EPOS software (see Chapter 2). 60 days of data from the DF and SF stations were processed together with the same orbits and clock products.

Name	Receiver	Antenna
0010	LEICA GRX1200GGPRO	LEIAT504GG LEIS
0012	LEICA GRX1200GGPRO	LEIAT504GG LEIS
0014	TPS NETG3	TPSCR.G3 TPSH
0022	TPS NETG3	TPSCR.G3 TPSH
0898	JPS EGGDT	LEIAR25 LEIT

Table 5.3: Hardware list of the five LUAMI reference stations (SAPOS stations).

5.1.2 Coordinate results from single frequency data

The repeatability of the station coordinates can be used as an indicator for the quality of a GPS receiver, and also of the impact of site-dependent effects. The coordinates of the stations were estimated daily using the PPP mode with IGS final products. **Figure 5.6** shows the estimated daily coordinate variations of the stations GP01 and LDB0. The estimated coordinates from the SF station GP01 has a standard deviation of 5, 6 and 7 mm in the North, East and Up components, respectively, while the DF station LDB0 has a standard deviation of 4 mm, 5 mm and 5 mm. The station GP01 has almost the same repeatability of coordinates as the DF station LDB0. The results of the L1_LDB0 were calculated from the L1 observations of the station LDB0 with the SEID method.

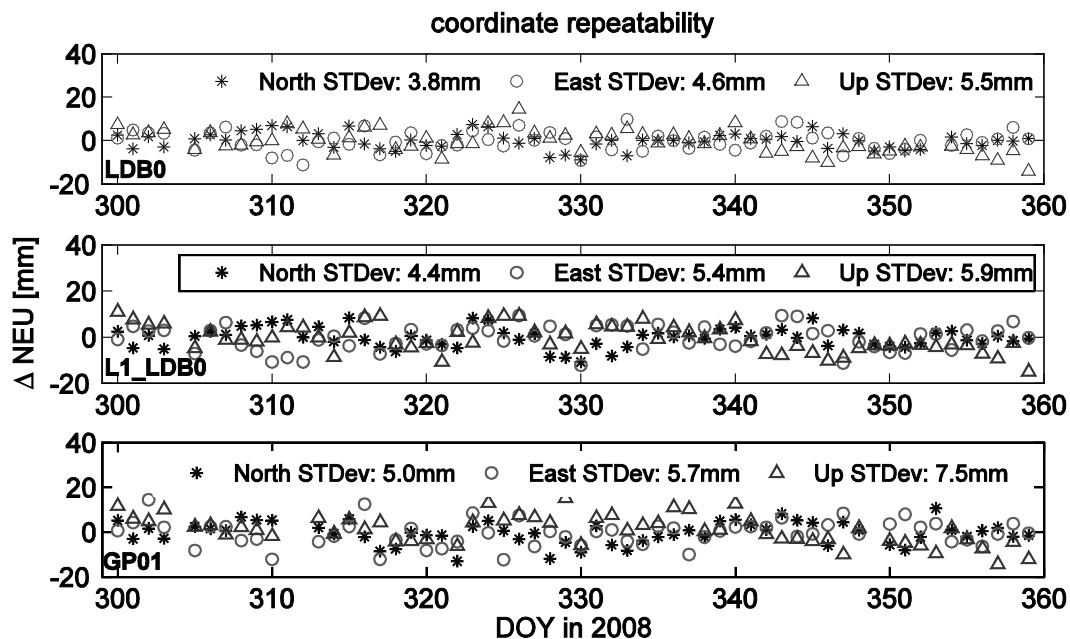


Figure 5.6: The estimated daily coordinate variations of the stations LDB0 (top), L1_LDB0 (middle) and GP01 (bottom) in the North, East and Up components (NEU).

The coordinate repeatability of the 13 SF stations and the two DF stations is given in **Figure 5.7**. The repeatability of the SF station coordinates is less than 8 mm RMS in their horizontal components, and less than 9 mm in the vertical component; the coordinate repeatability of the two DF stations is 5 mm and 6 mm respectively. The coordinate results are encouraging and show that the SF receivers are almost of the same high-quality as DF receivers.

In Zou et al. (2010), the SEID model has been adapted for a deformation monitoring study. Four densification studies with averaged reference station distances between 64 and 168 km demonstrated the effectiveness of the SEID model for deformation monitoring with SF receivers. For a densification with mean reference station distances below 90 km the repeatability of the SF station coordinates is comparable with those of the DF stations. With growing reference station separation the repeatability is reduced, especially in the up direction. Based on these results the densification of existing geodetic networks with SF receivers can be realized.

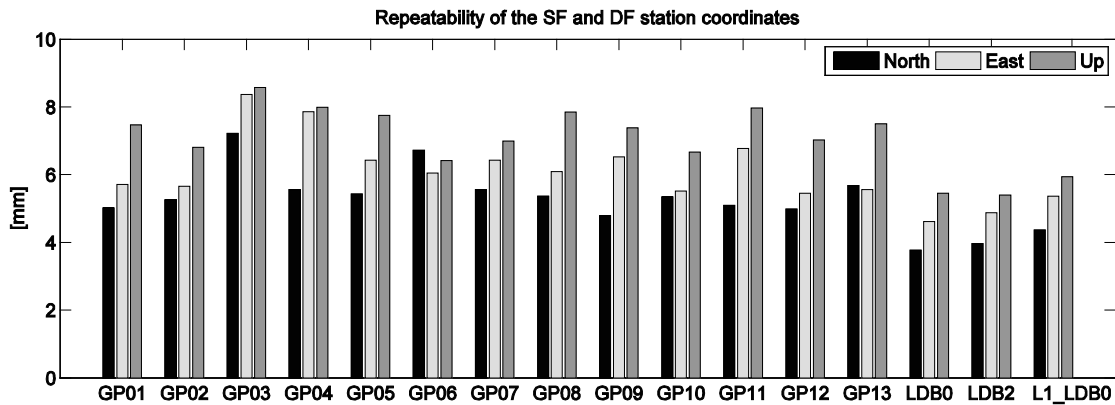


Figure 5.7: The repeatability of the LUAMI SF and DF station coordinates in the North, East and Up directions, DOY 300 – 360 in the year 2008.

5.1.3 ZTD and IWV results

Generally the ZTD is in the order of 2.5 m at sea level and shows variations up to 10 % mainly caused by the atmospheric humidity. Gendt et al. (2004) and Haase et al. (2003) showed that ZTDs, derived from DF data have an accuracy of 6 – 13 mm, when compared to weather models and radiosonde observations. Below, the ZTDs derived from the SF data are compared to the ZTDs derived from DF data, the differences are investigated.

In the whole period the variations of the ZTDs retrieved from the DF and SF stations are almost identical. Usually the weather in Germany is relative dry in November and December. Fortunately there was a strong weather front on DOY 319 (November 14th) in 2008. Weather fronts are important meteorological phenomena, which are caused by the clash of different wind patterns, temperatures and humidities, and bring a rapid change in weather. The weather fronts can cause rapid variations in the ZTD, and such rapid variations can introduce a systematic error in the estimated GPS station coordinates especially in height (Gregorius and Blewitt, 1998). During the weather front's approach on DOY 319, the ZTD increased by about 10 cm in 15 hours. In the first ten hours of DOY 320 the ZTDs decreased by about 7 cm. Then another small weather front passed the LUAMI network and caused the rapid variations in the ZTDs.

In **Figure 5.9** the thick blue line indicates the ZTDs retrieved from the DF station LDB0. For the data of the assumed SF station L1_LDB0 the ZTD results are plotted with a red line, which is nearly covered by the thick blue line. The ZTD from SF data have almost the same trend as from the DF data. The differences of the ZTDs from each station are correlated with the station height. The station altitudes are given in the legend. The stations at lower altitudes show larger ZTDs because of the higher atmospheric pressure. During the LUAMI campaign the ZTD gradient caused by the altitude is about -2.7 mm per 10 meter, which is larger than that calculated from the Saastamoinen model -2.9 mm per 10 meter. The ZTD gaps in the SF data during the first hour of DOY 320 were caused by data gaps of the reference stations.

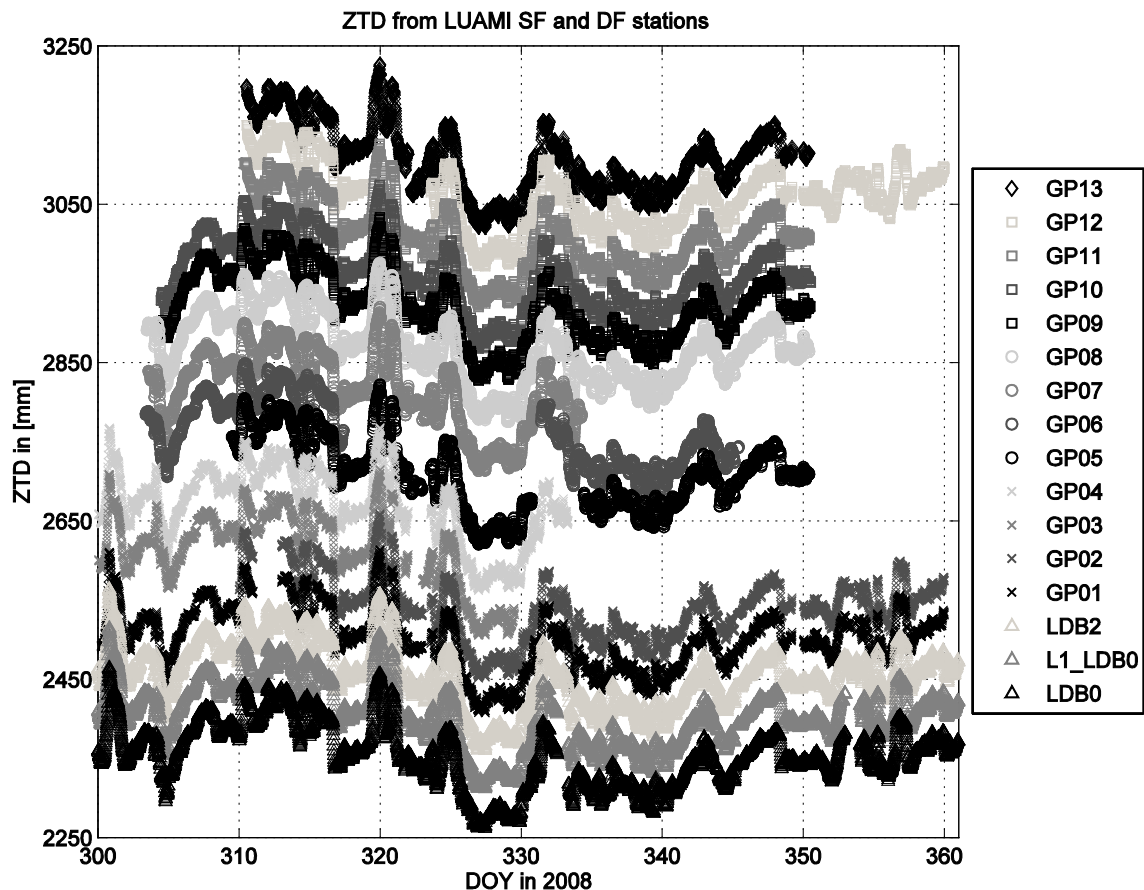


Figure 5.8: ZTDs derived from the LUAMI GPS data set for DOY 310–360 in 2008. The ZTDs from the SF data match those from the DF stations LDB0 and LDB2 almost perfectly.

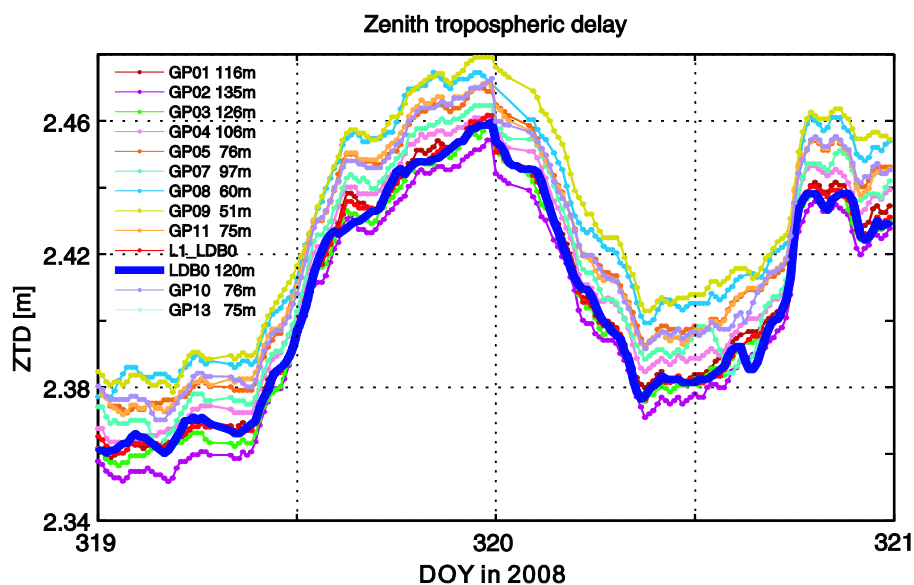


Figure 5.9: Variations of ZTDs from the SF stations and the test station LDB0 for DOY 319 (Nov. 14) and 320 (Nov. 15) in 2008.

The two SF stations GP01 and GP02 were collocated with the LDB0 station within

200 m distance. The ZTDs from the converted DF data at the stations GP01, GP02, and L1_LDB0 are compared with those from the observed DF data at LDB0. Since the station heights of the GP01 and GP02 are different to LDB0, the ZHD corrections of station height are applied with the Saastamoinen model and surface pressure. The ZTD differences are calculated for 60 days as:

$$\Delta ZTD = ZTD_{SF} - ZTD_{DF} \quad (5.1)$$

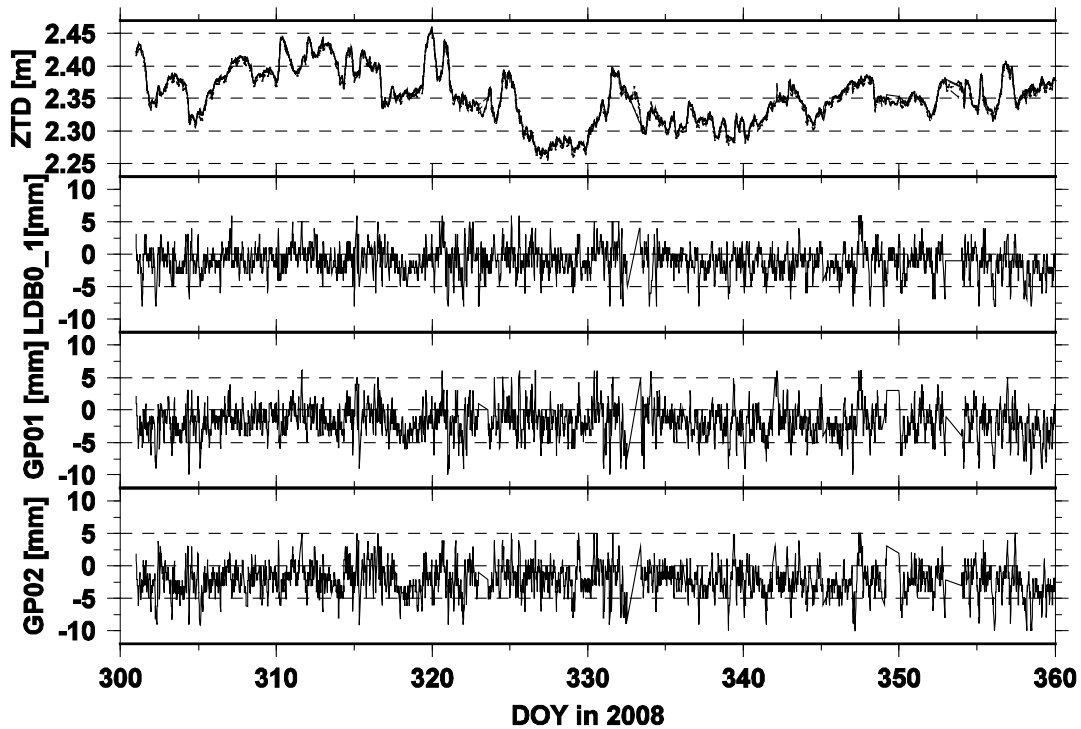


Figure 5.10: ZTDs derived from DF data at LDB0 in meter (top), and the differences to the ZTDs at L1_LDB0, GP01, and GP02 (bottom three plots).

The ZTDs derived from the station LDB0 are plotted in **Figure 5.10** (top). They varied between 2.25 m and 2.45 m in the 60 days. The ZTD differences between the observed DF data at LDB0 and the converted DF data at LDB0, GP01, and GP02 are shown in **Figure 5.10** (bottom), and agree within ± 5 mm.

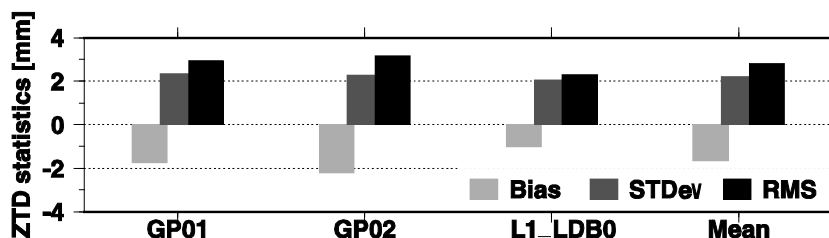


Figure 5.11: Bias, standard deviation (STDev), and RMS from the ZTD differences at the three LUAMI stations GP01, GP02, L1_LDB0 and the total differences.

The bias, standard deviation, and RMS from the ZTD differences of the three comparisons are given in **Figure 5.11**. The L1_LDB0 has a smaller bias and RMS than GP01 and GP02. Since the accuracy of the ionospheric correction is the same for all three stations, the larger ZTD RMS of the real SF stations GP01 and GP02 are caused by the lower performance of low-cost receiver antennas or further station-dependent

effects. The bias, standard deviation and RMS of the ZTD differences are -1.6 mm, 2.2 mm, and 2.8 mm, respectively. The ZTD RMS of the real SF receivers is below 3 mm, which is significantly smaller than the accuracy of DF ZTDs (6–13 mm) (Gendt et al., 2004). The systematic negative ZTD bias could be an effect of the inaccurate PCV corrections of the reference stations.

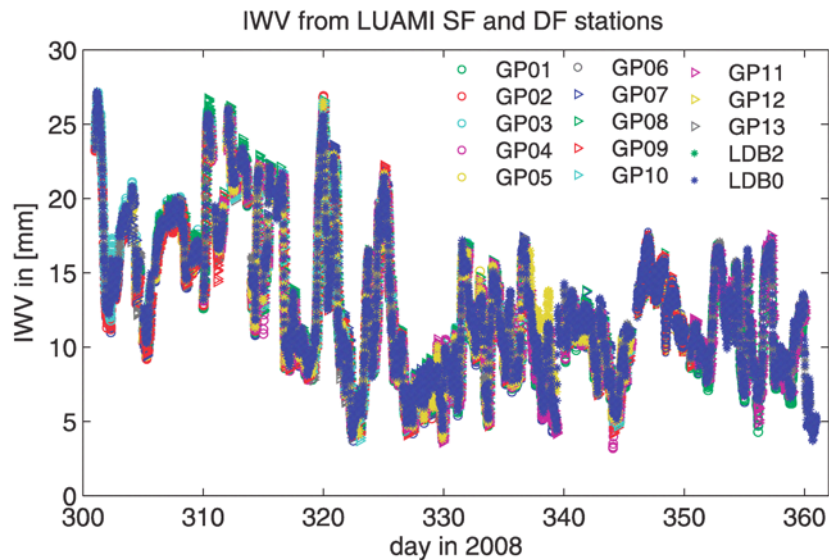


Figure 5.12: Retrieved IWV observations from DF and SF data during the LUAMI campaign.

Furthermore, the estimated ZTDs from the LUAMI network were converted to IWV data using linearly interpolated meteorological observations, i.e., pressure and temperature from surrounding SYNOP stations (Gendt et al., 2004). The retrieved IWV from the LUAMI network is plotted in **Figure 5.12**. In general the IWVs from DF and SF data agree very well in the 60 days. The ZTD comparison results show that the ZTD accuracy of the SF data is about 3 mm; with the conversion factor $\Pi^{-1} = 6.45$ the IWV retrieved from SF data has an accuracy of about 0.5 mm.

5.1.4 GPS Tomography for LUAMI

The atmospheric corrections estimated by the GPS data processing systems provide considerable information about the atmospheric state. In particular the STD, i.e., the GPS signal delay due to the neutral atmosphere, is mainly caused by the lower few kilometers of the atmosphere and can be used to estimate the spatial distribution of the refractivity or humidity in the troposphere (up to ~10 km). As the STD is a quantity integrated along the GPS signal path, a large number of intersecting STD observations from dense ground networks are required to obtain spatially resolved fields. This can either be achieved by assimilating the STDs to numerical weather models or by tomographic reconstruction techniques.

With a water vapor tomography system developed at GFZ (Bender et al., 2010) several tomographic reconstructions were carried out using the STD/SWD observations from the combined SF/DF receiver network available during the LUAMI campaign. While the network dimensions of 10 km × 15 km around the observatory were rather small a considerably larger region of about 88 km × 95 km was used for the tomographic

reconstruction. The increased dimensions of the 3D grid used by the tomography have the advantage that all slant paths from the LUAMI network remain within this grid even at low elevations of 5° . In case of a smaller grid much of these low elevation STDs would not reach the upper grid level at 10 km and would either be rejected or truncated. Another reason for extending the region is the rather low atmospheric variability within a radius of ~ 10 km leading to almost homogeneous horizontal distributions which can hardly be separated from the tomographic uncertainties. Within the extended grid the spatial and temporal atmospheric variations can clearly be identified.

A regular latitude/longitude grid with a horizontal resolution of about 7 km (E-W: 88 km, 12 cells, N-S: 95 km, 14 cells) and a vertical resolution between 200 m and 300 m reaching up to 10 km above sea level (ASL) was used for the tomography. The wet refractivity within these 5,600 – 8,400 grid cells (voxels) was reconstructed using about 2,000 – 3,500 SWDs provided by 24 stations within 30 minutes. The SWDs were computed from the STDs and the SHDs estimated using the Saastamoinen model and surface meteorological observations. The initial field was taken from the German weather model (COSMO) or filled with an exponential vertical profile without any horizontal structure. In both cases reasonable results could be obtained but the initialization with the COSMO field leads to vertical profiles which show smaller discrepancies to the radiosonde profiles. Most reconstructed fields show several artifacts from the tomographic reconstruction leading to a clearly over/underestimated humidity in some isolated voxels. However, it must be pointed out that the problem is considerably underdetermined in most regions of the grid since 5,600 – 8,400 unknowns have to be determined from 2,000 – 3,500 observations which are very inhomogeneously distributed.

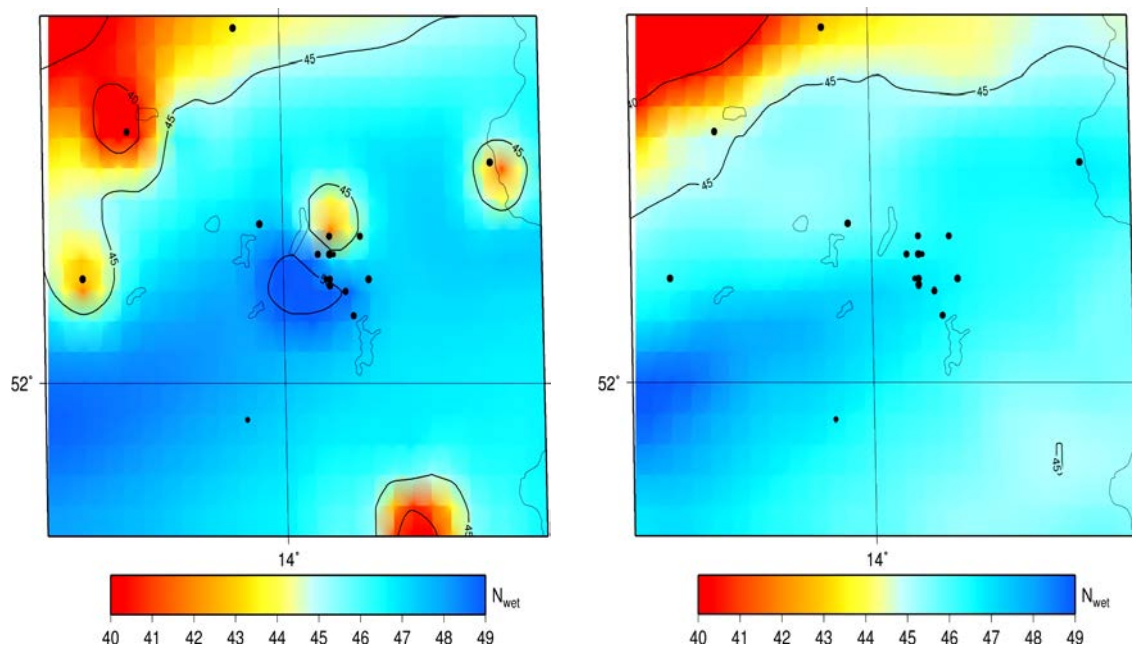


Figure 5.13: 17:30 UTC on November 9, 2008: horizontal distribution of the “wet” refractivity at 609 m ASL from the tomography (left panel); horizontal distribution of the “wet” refractivity at 609 m (ASL) from COSMO-DE (right panel). A dry front (red color) propagated from NW through the reconstruction area.

A horizontal layer of a typical tomographic reconstruction is shown in **Figure 5.13** (left panel). At 17:30 UTC on November 9, 2008, the rather wet air (blue) within the reconstructed region is replaced by dry air (red) approaching from northwest. The

609 m ASL layer (about 500 m above ground) clearly shows the dry front but also some dry artifacts around several stations (black dots in **Figure 5.13**).

The results of the tomographic reconstructions were compared with the 3D fields of COSMO analyses and with radiosonde profiles. **Figure 5.13** (right panel) shows the COSMO field interpolated to the 609 m layer together with the reconstruction (left panel in **Figure 5.13**). Except for the artifacts both fields are rather similar but the dry front within the model is about two hours delayed. Radiosonde profiles from three soundings at 12:00, 18:00 and 0:00 UTC on November 9/10, 2008 and tomography profiles are shown in **Figure 5.14**. The 3D tomography field was interpolated on the radiosonde positions and is in rather good agreement with the RS observations. The tomography clearly reconstructs the vertical structures but leads to much smoother profiles as the vertical resolution of the grid is lower than the observed profiles. In some cases the reconstruction algorithm over-compensates the vertical variations or leads to oscillations as, e. g., in the 0:00 UTC profile (**Figure 5.14**, right panel).

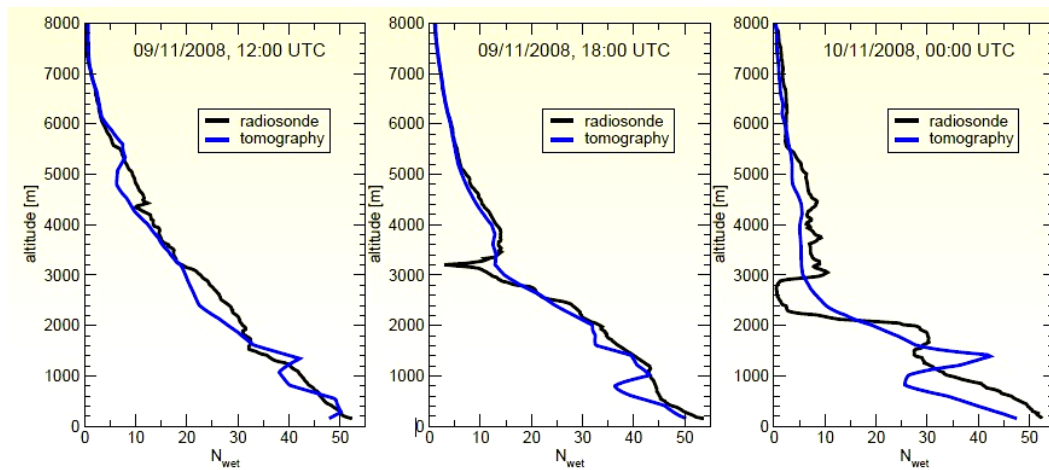


Figure 5.14: Vertical N_{wet} profiles observed from radiosonde and tomography on November 09/10 2008, 12:00, 18:00 and 00:00 UTC.

5.1.5 Long-term stability of single frequency data

The station GP01 is installed at the Lindenberg observatory of the DWD (**Figure 5.1**). After the end of the LUAMI campaign the station GP01 continued operation for long-term validations. Another SF station (GP00) was mounted on the roof of the geodetic institute (A17 building) of GFZ in September 2008 (**Figure 3.4**). The long-term stability of the SF receivers is compared to collocated DF receivers and is investigated below.

SF station GP00 at GFZ

The GPS station POTS is an IGS permanent station, which is located about 2 meters east of GP00. On DOY 046 in 2011 the hardware of the station POTS was updated. The old receiver (antenna) AOA_SNR-8000_ACT (AOAD/M_T) was replaced with a JAV_RINGANT_G3T (JAVAD TRE_G3TH). The estimated tropospheric products of the station POTS are the reference solution to validate the collocated SF station GP00. For ionospheric corrections 5 surrounding SAPOS stations serve as reference stations to

apply the SEID method. The mean distance between the reference stations and GP00 is about 32 km (**Figure 5.15**).

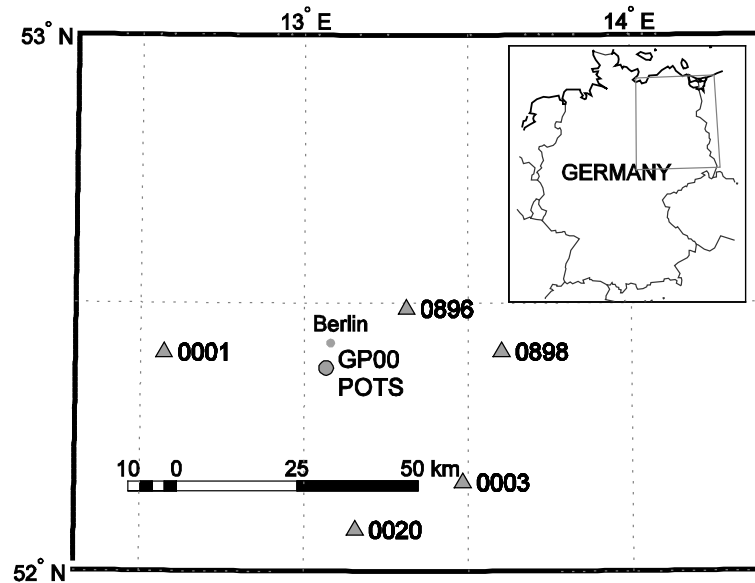


Figure 5.15: Five SAPOS stations serve as reference stations for ionospheric correction (triangles); GP00 is a SF station (circle), collocated with the IGS station POTS.

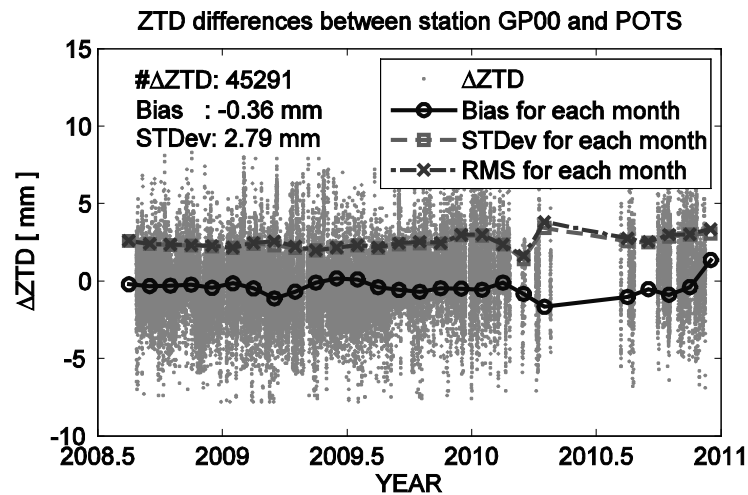


Figure 5.16: ZTD differences between the SF GPS station GP00 and the DF station POTS; the bias, standard deviation and RMS are generated for each month.

Each hour the received GPS data from GP00 are saved in a binary file, and sent to a GFZ data server. Firstly the binary file is converted to RINEX format, before the file is archived in a RINEX data server. To avoid data gaps caused by the latency of the data from the GPS stations, a post-processing of the SF data conversion is applied with one day latency. The SF station GP00 worked rather reliable since DOY 239 in 2008. There is a big data gap (between March and June) in 2010, which was caused by the interrupted connection between the GPS receiver and the mini-computer. The station GP00 provided 571 days of almost continuous GPS data in the 2.5 years. Together with the station POTS the converted DF GPS data of GP00 were processed in post-processing mode using the EPOS software. The ZTD observations of the stations GP00 and POTS are compared in **Figure 5.16**.

In **Figure 5.16** the circles, squares and crosses indicate the bias, standard deviation and RMS of the ZTD differences generated for each month. The accuracy of the ZTD derived from the SF data is almost constant over the period when compared to DF results. The large RMSs are caused by the data gaps. The bias of the total ZTD differences between GP00 and POTS is about -0.4 mm and the standard deviation is 2.8 mm, which is consistent with other test results. In addition, there is no significant effect of seasonal variations; the large differences in monthly biases are mostly caused by missing data. However, the data period is only about 2.5 years, which should be extended to a larger period.

Since the two stations have a distance of only about 2 meters and have 22 cm height difference, the STDs retrieved from GP00 should be very close to the STDs from the station POTS. About 2.2 million STDs from the two stations were compared:

$$\Delta\text{STD} = \text{STD}_{SF} - \text{STD}_{DF} . \quad (5.2)$$

The results are plotted in **Figure 5.17** and **Figure 5.19**.

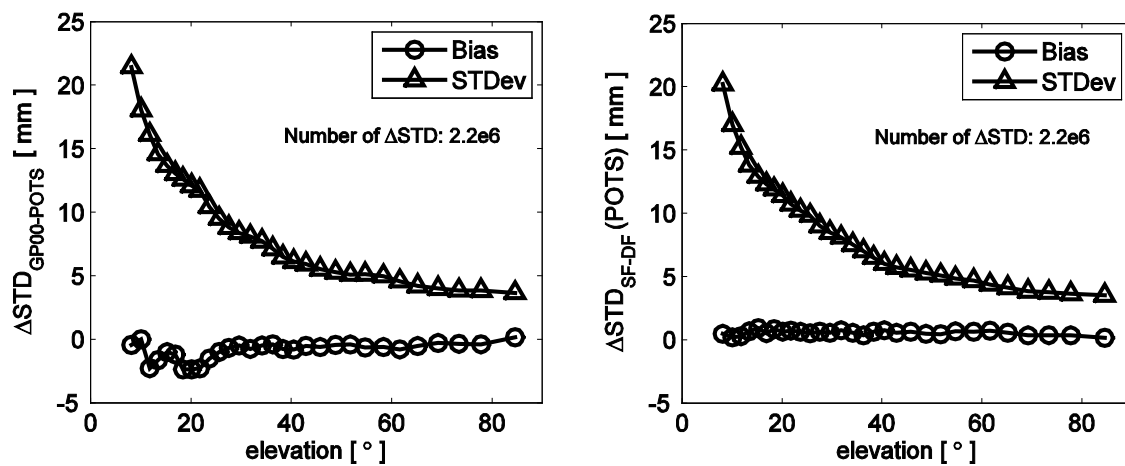


Figure 5.17: STD differences between the SF GPS station GP00 and DF station POTS versus the elevation angle (left panel); the STD differences between the SF and DF POTS (right panel).

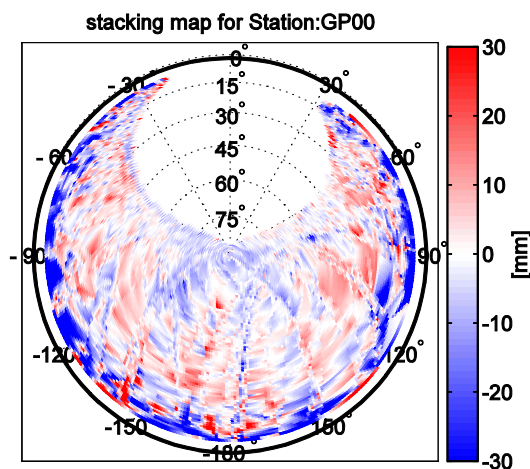


Figure 5.18: The stacking map of the SF station GP00 for DOY 110–128 in 2007 shows multipath effects at low elevations.

The bias and standard deviation were calculated with a running window of about 0.7 million STD differences (**Figure 5.17**, left panel). Close to zenith they are 0.1 mm and

3.6 mm, respectively, and increase to 0.4 mm and 21 mm at elevations close to 7° , since the observations at lower elevations have larger noise than at high elevations. Comparing the statistics of the STD differences between the assumed SF station POTS and the DF station POTS (**Figure 5.17**, right panel), multi-path effects can be detected at the station GP00 for elevations below 20° (**Figure 5.18**).

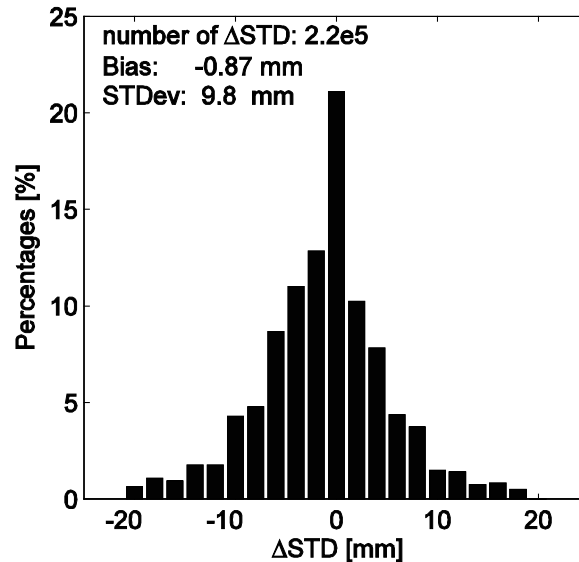


Figure 5.19: Histogram of the STD differences between GP00 and POTS.

Figure 5.19 shows the histogram of the STD differences. The total STD differences have a bias of -0.87 mm and a standard deviation of 9.8 mm.

SF station GP01 at Lindenberg

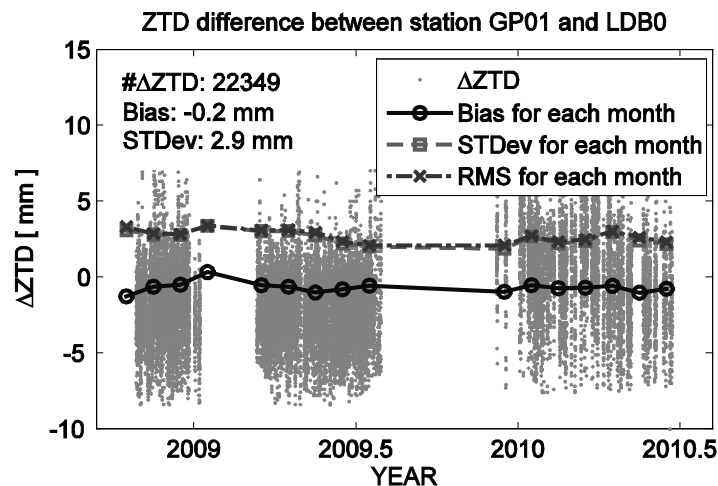


Figure 5.20: ZTD differences between the SF GPS station GP01 and the DF station LDB0; the bias, standard deviation and RMS are generated for each month.

The data from the SF station GP01 at Lindenberg have more gaps than the SF station GP00, which are caused by interruption of the connection between receiver and mini-computer. The ZTD differences between GP01 and LDB0 are given in **Figure 5.20**. Similar to **Figure 5.16** the circle, square and cross represent the bias, standard deviation and RMS for each month. The RMS of the total ZTD differences is below 3 mm, which is consistent with the results of LUAMI.

5.2 Densification of the German GPS network

Since so far a SF GPS network has not been established in Germany, a simulation study was conducted in order to estimate the potential of a large SF network embedded in the existing DF network. The data of 258 German GPS stations (**Figure 5.21**) were processed from day 220 to 230 (August 8 – 18) in 2007. Most stations belong to SAPOS but data of other providers such as EUREF, BKG or GFZ were also available. The selected time interval is part of the COPS (see sec. 4.2.3). The main objective of COPS is to identify the physical and chemical processes responsible for the deficiencies in quantitative precipitation forecasting over low-mountain regions. In COPS a large number of meteorological instrumentation was operated, partially combined for the first time, e.g., GPS, advanced LIDAR and radar systems. For the COPS experiment, a region in south-western Germany/eastern France has been selected, where severe thunderstorm activity is frequent in summer with significant amounts of precipitation and risk of flash flood events. In the selected region a dense GPS network (10 km horizontal resolution in a 50 km² area) was set up for the meteorological study. All stations are equipped with geodetic DF receivers.

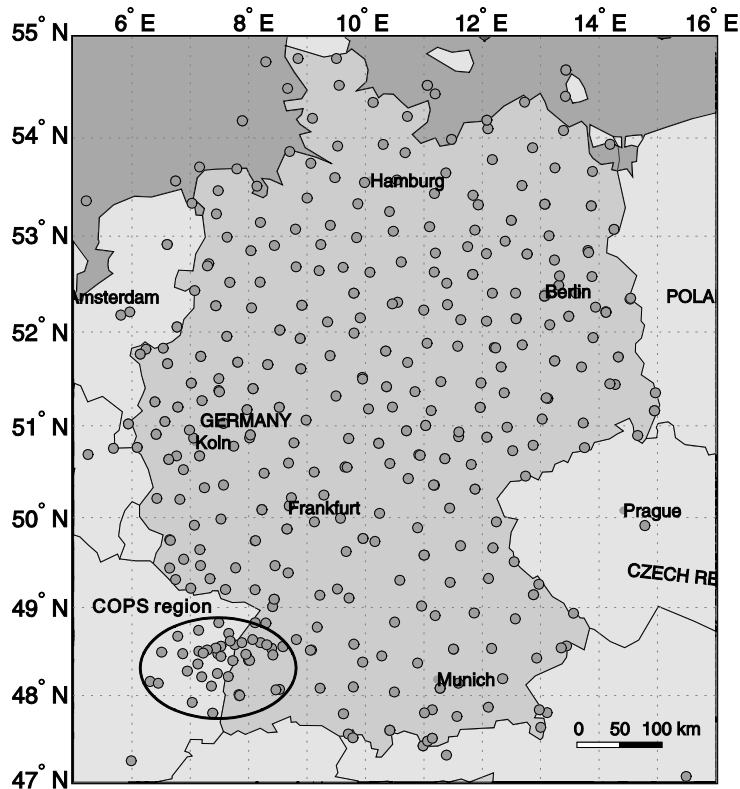


Figure 5.21: Available DF GPS stations in and near Germany in DOY 220 – 230, 2007; the location of the COPS network is marked with an ellipse.

The data of the GPS stations were processed in two different ways: At first, the L_1 and L_2 observations from DF stations were used to derive tropospheric products, which were subsequently used as a reference. Second, only the L_1 observations from DF stations were used, the L_2 observations were generated using ionospheric corrections from surrounding DF stations. In this way each station was regarded as a hypothetical SF station embedded in the currently existing DF network. The application of SEID requires a minimum of three DF reference stations to estimate the three parameters a_i of

the ionospheric correction. More reference stations will improve the reliability and avoid problems caused by missing data. In this study a minimum of 6 and a maximum of 10 reference stations within a radius of 100 km around the hypothetical SF station were required to model the epoch-differenced ionospheric delay. Both the converted and observed data sets were processed with EPOS in post-processing mode. The SF data from 258 stations out of the 279 available stations could be processed successfully using the SEID method and EPOS. The L_2 signal of the 21 remaining stations could not be determined in this way as the up to 85% L_2 observations of the surrounding DF are missing. Finally, two sets of tropospheric products were available: STDs (ZTDs) retrieved from DF data and STDs (ZTDs) retrieved from simulated SF data. These tropospheric products were compared with each other and with independent data from a numerical weather model and a water vapor radiometer (Deng et al., 2011).

5.2.1 Comparison of tropospheric products from assumed SF and real DF stations

All test GPS stations are equipped with geodetic quality DF receivers and antennas. The ZTDs and STDs derived from DF stations have the best accuracy and are used as reference solution. The assumed SF stations have the same L_1 observations as the DF stations, only their L_2 observations are generated with the SEID model. The direct comparison of the tropospheric products, e.g., ZTDs and STDs retrieved from the SF and DF data shows the efficiency of the SEID model under different configurations.

ZTD Validation

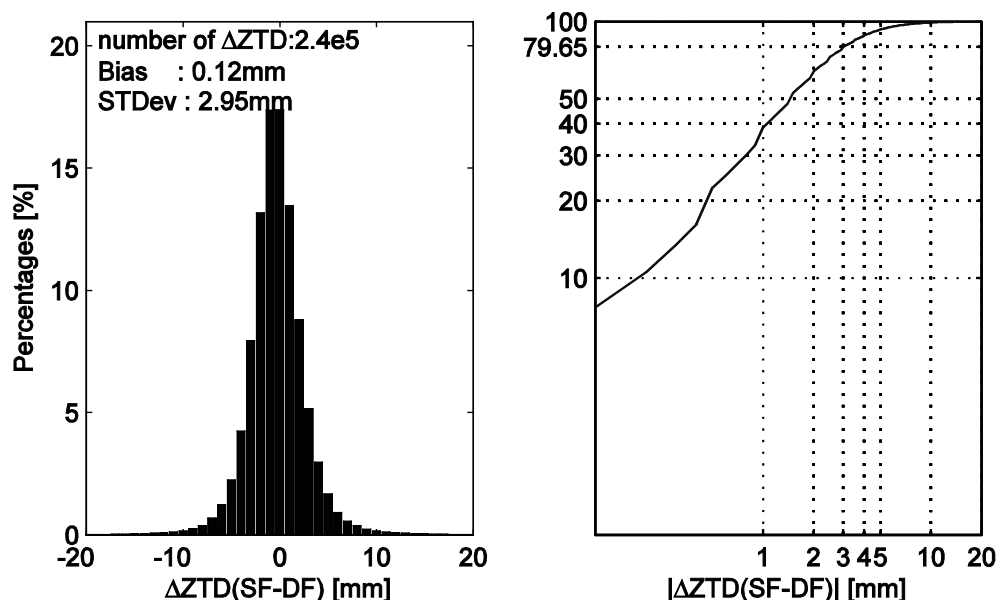


Figure 5.22: Histogram of the ZTD differences (left panel) and cumulative distribution of the absolute ZTD differences (right panel) between 258 SF and DF stations as computed for each station in DOY 220 – 230 in 2007.

After the data processing about 240,000 ZTDs from SF and DF stations were compared. The bias is as small as 0.1 mm and the standard deviation is 2.9 mm (Figure 5.22 left panel). 79.65% absolute ΔZTD are smaller than 3 mm (Figure 5.22 right panel). In

essence the deviation between SF and DF retrieved ZTDs is significantly smaller than the accuracy of DF ZTDs (6-13 mm). The ΔZTD histogram shows a rather narrow distribution with very few differences above 5 mm. This is consistent with earlier results presented by Deng et al. (2009).

In the following, some reasons for the discrepancies are analyzed. There are the geographic distributions of large ZTD RMS for some stations; the reasons could be data missing at reference stations, possible higher ionospheric activity and unbalance distribution of the reference stations.

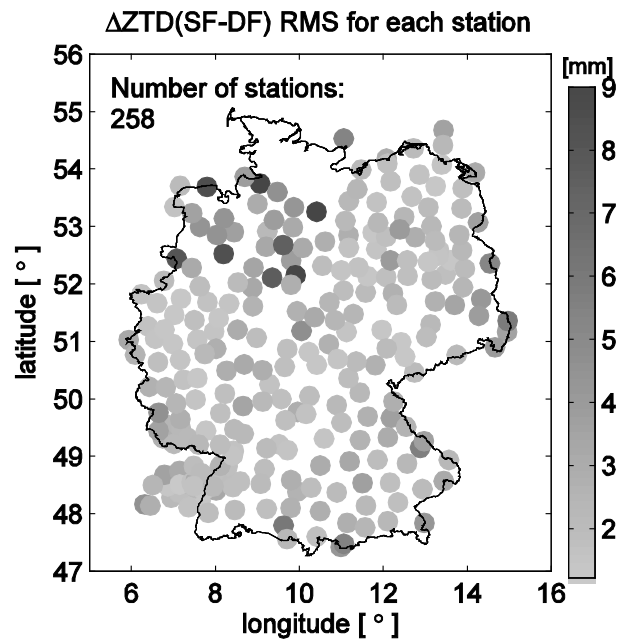


Figure 5.23: RMS of the ZTD differences between 258 SF and DF stations as computed for each station in DOY 220 – 230 in 2007.

The geographic distribution shows that the larger differences are mainly caused by some stations with a large RMS above 5 mm (**Figure 5.23**). Most of them are located at the outer boundaries of the network and it can be assumed that the quality of the ionosphere correction with the SEID method was affected by the unbalanced distribution of the nearby DF stations. The map of the station RMS also shows that the RMS is rather small in regions of high station density, e. g., in the south-western part, and larger in less dense regions, e.g., in the north-western part. 8 stations in north-western Germany show an RMS above 6.5 mm. In addition, during the selected data period some reference stations in northwest Germany had an unusually large number of missing data, which caused additional ambiguities in the converted \tilde{L}_2 signal of the 8 stations and corrupted the tropospheric products.

The number of the available dL_4 observations between DOY 220 – 230 in 2007 is calculated for each station. In **Figure 5.24** the gray shade of the dots denotes the number of the dL_4 observations; some stations in northwest Germany have less dL_4 observations than other stations. In such situations more reference stations are needed to model dL_4 ; and those stations should be excluded from the set of reference stations. Exemplarily the situations of two stations (LDB0 and 0668) are discussed.

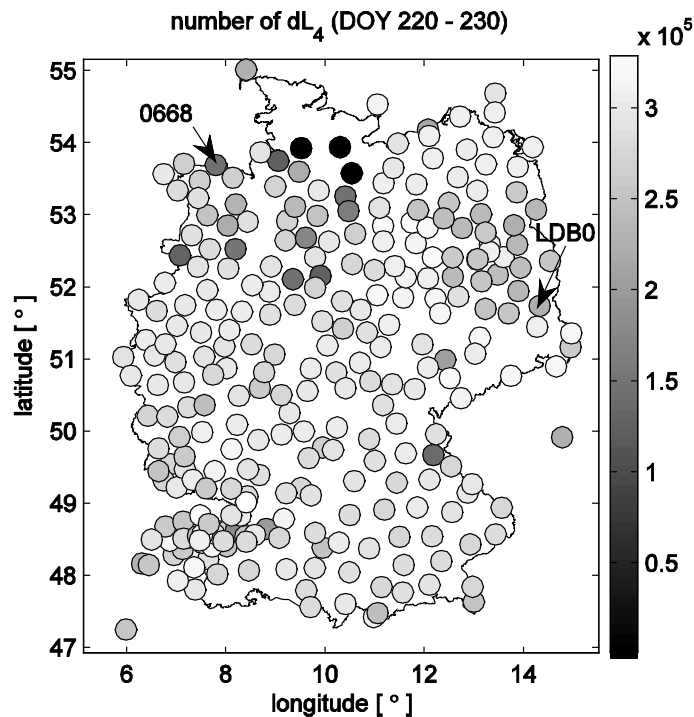


Figure 5.24: The number of dL_4 observations for each DF station in DOY 220 – 230, 2007.

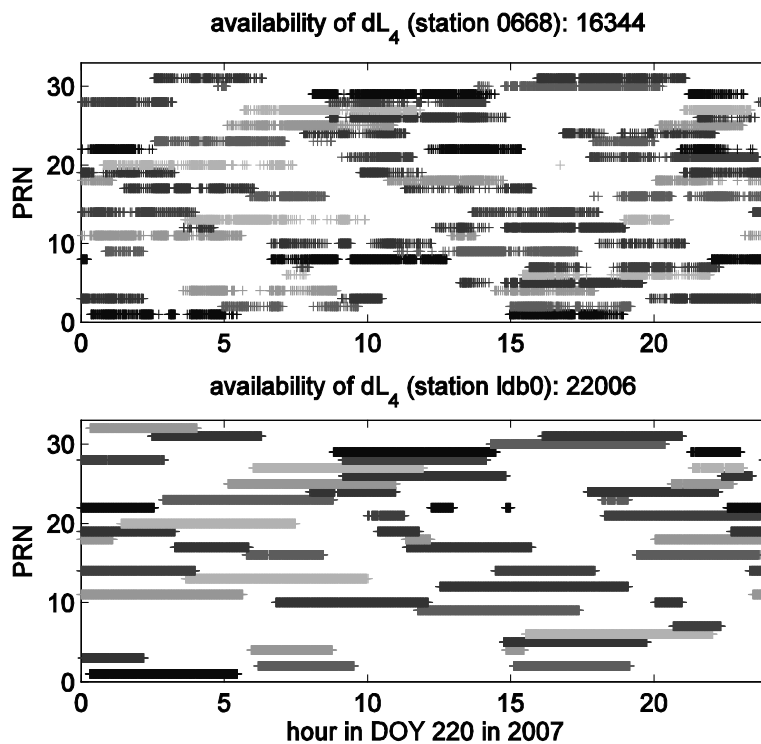


Figure 5.25: dL_4 availability of station 0668 (top), which is located in the north-west part of Germany; dL_4 availability of station LDB0 (bottom), which is located in the eastern part of Germany. The dL_4 time series of the station 0668 has more gaps and fewer observations than those of the station LDB0.

The station 0668, which is located in the northwest part of Germany, has 16,344 dL_4 observations, and the station LDB0 in the east part of Germany has 22,006 dL_4

observations (**Figure 5.24**). For both stations the availability of the dL_4 observations on DOY 220 from each satellite are plotted in **Figure 5.25**. The station 0668 has more missing epochs than the station LDB0. The missing epochs are caused by data gaps, outliers or new ambiguities that have to be set up. Compared to LDB0 the number of dL_4 observations from 0668 is smaller and the data show more ambiguities. The missing dL_4 observations of the reference stations can cause instable ionospheric corrections for the SF GPS data. In extreme cases the available dL_4 observations from the reference stations in one epoch can be fewer than three, which causes a discontinuous ionospheric correction for the SF GPS data. For the discontinuous epoch, a manual cycle slip has to be inserted in the converted \tilde{L}_2 data. The additional cycle slips can corrupt the accuracy of the ZTD parameter estimation.

Since the accuracy of the ionospheric correction from the SEID model can be reduced under high ionosphere activity, the ionosphere activity above Germany between DOY 220 and DOY 230 in 2007 was studied using European TEC data provided by the DLR. The TEC data have a spatial resolution of 2.5° (EW) \times 5° (NS), and a temporal resolution of 30 minutes. In the 11 days there are 528 TEC maps available. To detect the activity of the ionosphere during the 11 days, the mean values and standard deviations of the 528 maps are calculated, and the results are plotted in **Figure 5.26**.

In the 11 days the mean TEC in North West Europe was larger than in South East Europe (**Figure 5.26** left panel). From the right panel of **Figure 5.26** it can be seen that the TEC in the Southwest of Europe varied more significantly than in the Northeast. However, the accuracy of such TEC maps is about 2-3 TECU (<http://swaciweb.dlr.de>). It is difficult to detect rapid ionospheric variations, e.g., MSTID with the TEC maps.

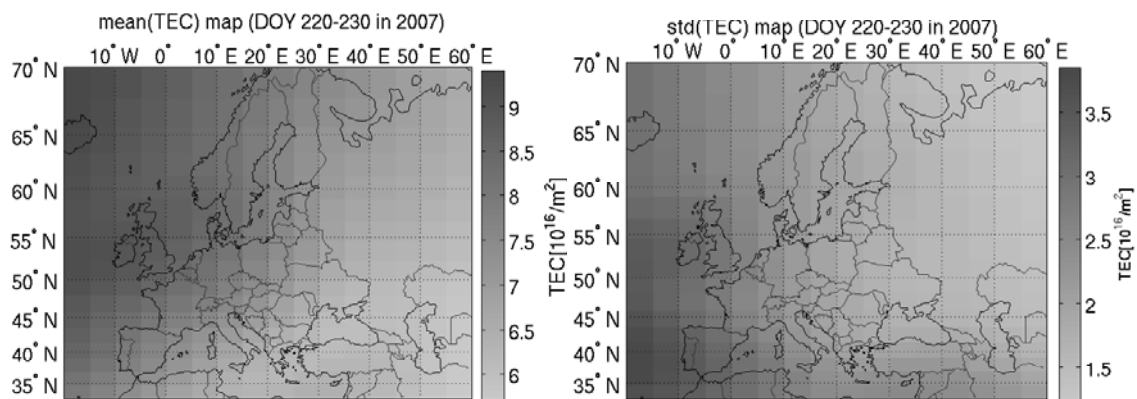


Figure 5.26: The mean (left panel) and standard deviation (right panel) of VTEC over Europe during the 11 days.

For each assumed SF station the distribution of its reference stations is different, i.e., the configuration of the reference stations as well as the mean distance from the reference stations to the assumed SF station differs. **Figure 5.27** shows the RMS of the ZTD differences between SF and DF stations versus the mean distance, which is approximately proportional to the ZTD RMS. The results are consistent with the densification test in Chapter 4. In the simulation study the mean distance to the reference stations ranges from about 20 km to 60 km, and the ZTD RMS could be fitted to a trend line. The standard deviation of the post-fit residuals is 0.77 mm; the offset and slope are 1.54 mm and 0.018 mm/km, respectively (**Figure 5.27**). To check the significance of the two polynomial coefficients the t-test (Koch, 2004) is applied. The t-test values of the two polynomial coefficients are 6.8 and 3.9. Given 256 degrees of freedom and for significance level of 95% the t-source equals 1.6, thus both polynomial

coefficients are significant. Since in the test network about 30 different types of the receivers and antennas are used, hardware inhomogeneities and inaccurate PCV models can have a negative impact on the ZTD estimation. However, since most of the assumed SF stations have about 10 reference stations, the effect of hardware inhomogeneity and the inaccurate PCV model cannot be easily separated from other effects.

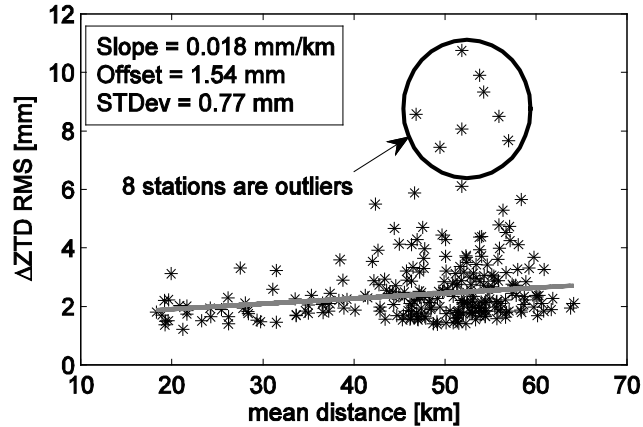


Figure 5.27: RMS of the ZTD differences between SF and DF stations versus the mean distance from the test station to the reference stations.

The comparison of the ZTD between SF and DF results shows that the ionospheric correction of the SEID model would be sufficient for the ZTD estimation within a densified SAPOS.

STD Validation

Large numbers of STDs provide spatially resolved information about the atmospheric state and have a considerable potential in future applications like GPS tomography. In zenith direction the STD is ~ 2.5 m, for lower elevations the STD increases up to ~ 25 m at 5° elevation. Therefore, absolute differences can only be compared if the elevation is identical. In addition, to the absolute STD difference the relative STD difference is defined by:

$$\Delta\text{STD}_{rel} = \frac{\Delta\text{STD}}{\text{STD}_{DF}}. \quad (5.3)$$

About 10 million STDs from assumed SF and DF receivers were compared. **Figure 5.28** (left panel) shows the bias and the standard deviation between SF and DF STDs versus the elevation angle. Each bias and standard deviation was computed from about 330,000 STD differences. For all elevation angles the bias is significantly smaller than the standard deviation, i.e., differences between DF and SF STDs are random and not systematic. Close to the zenith the bias and the standard deviations are 0.3 mm and 4.5 mm, respectively. The bias and the standard deviation are increasing with decreasing elevation angles and reach 0.6 mm and 24 mm, respectively, at an elevation angle of 7° .

For most applications the STD deviation per unit length or the relative deviation is much more important. The right panel of **Figure 5.28** shows the relative bias and standard deviation between SF and DF STDs versus the elevation angle. The relative standard deviation is almost constant for all elevation angles and equals $\sim 0.18\%$, i.e., the relative accuracy of SF STDs, when compared to DF STDs, is not degrading with

decreasing elevation angles.

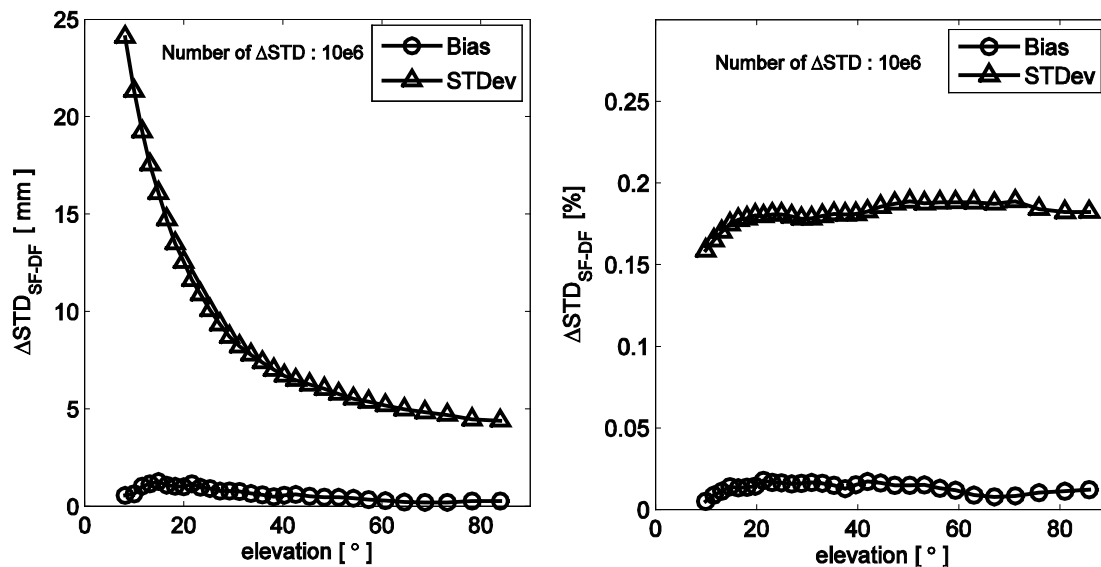


Figure 5.28: The bias and the standard deviation between SF and DF STDs versus the elevation angle (left panel); the relative bias and standard deviation between SF and DF STDs versus the elevation angle (right panel) for DOY 220-230 in 2007.

Note that the standard deviation between SF and DF ZTDs ($\sigma = 2.9$ mm or ~ 0.13 %) is somewhat smaller than the standard deviation between SF and DF STDs close to the zenith. An explanation is that one ZTD is modeled by several STDs of one station for a short period of time (from several minutes to hours) using a mapping function. Therefore the ZTDs have smaller noise than the STDs.

Comparing STDs from DF data processed like hypothetical SF data with STDs from real DF observations shows mainly the impact of an imperfect ionosphere modeling on the processed tropospheric products. Real SF data will show some more deficiencies like increased receiver noise, inferior antenna quality, increased multipath effects, etc. (see Chapter 5.1.3). The errors estimated here can therefore only be a lower bound for the errors to be expected from real SF observations. However, observations with real SF receivers showed very promising results with errors comparable to the errors found in this analysis (Deng et al., 2009). In a future densification of the complete SAPOS GPS network the SF receivers will be placed between the DF stations leading to considerably smaller distances to nearby DF receivers and better ionosphere corrections. No SF receivers will be installed near the network boundaries or at other unfavorable positions.

5.2.2 Validation with the ECMWF model using ray-tracing

Ray-tracing

In order to compare STDs with their model equivalents, ray-tracing through the ECMWF analyses ($0.5^\circ \times 0.5^\circ$ horizontal resolution; 91 vertical levels) were performed. The ray-tracing software was developed at GFZ (Zus et al., 2008). The ray-trajectory in the ECMWF refractivity field is determined through Fermat's principle: the path taken by a ray between two points, i.e., the ground-based receiver and the GPS satellite, minimizes the signal travelling time. From calculus of variations a system of ordinary

differential equations is derived and solved by a fully implicit finite difference scheme. Once the ray-trajectory is determined, the STD can be computed according to Eq. (2.10). For better efficiency the ray-tracing is restricted to the plane defined by the ground-based receiver, the GPS satellite and the center of the Earth. The Earth is assumed to be a perfect sphere with a mean radius being equal to the local curvature radius of the reference ellipsoid at the center point of the ECMWF model domain.

In essence, the uncertainty of ray-traced STDs due to simplifying assumptions was estimated to be ~ 1 mm in the zenith and ~ 1 cm at an elevation angle of 5° . The ECMWF meteorological variables themselves (pressure, temperature and humidity), the refractivity field and subsequently the STDs are uncertain. Järvinen et al., (2007) made an attempt to quantify the uncertainty of simulated STDs due to the uncertainty of (typical) numerical weather model refractivity fields. They estimated the uncertainty of the STD simulation to be ~ 8 mm in the zenith and ~ 8.4 cm at an elevation angle of 5° .

Inter-comparison

The ECMWF analyses are available for 0:00, 6:00, 12:00 and 18:00 UTC. For the 11 days regarded here STDs retrieved from GPS data were compared with their model equivalents. Data within a time window of ± 2 h enter the statistical inter-comparison. The discrepancy between STDs retrieved from GPS data and their model equivalents is measured in terms of absolute and relative differences:

$$\begin{aligned} \Delta\text{STD} &= \text{STD}_{\text{ECMWF}} - \text{STD}_{\text{GPS}}, \\ \Delta\text{STD}_{\text{rel}} &= \frac{\Delta\text{STD}}{\text{STD}_{\text{ECMWF}}}. \end{aligned} \quad (5.4)$$

According to **Figure 5.28** the statistical inter-comparison from simulated SF and observed DF data indicates a good agreement over the entire elevation range. While the magnitude of absolute differences increases with decreasing elevation angles in case of SF and DF data, the relative differences are almost constant. The bias of the relative differences is $\sim 0.2\%$ in case of both SF and DF data (in the zenith this corresponds to $2.5 \text{ m} \cdot 0.2\% \approx 5 \text{ mm}$). The standard deviation of the relative differences is $\sim 0.55\%$ for both SF and DF (in the zenith this corresponds to $2.5 \text{ m} \cdot 0.55\% \approx 14.7 \text{ mm}$). This finding is consistent with results obtained from comparable studies (Eresmaa et al., 2008; Pany et al., 2001).

The bias and the standard deviation for individual stations are shown in **Figure 5.29** and **Figure 5.31**. The biases are larger at stations located in northeast and southwest Germany while the standard deviations are enhanced at stations located in northwest Germany. The colors of the two stations SAL2 (E 11.17° , N 52.84°) and HOMM (E 7.14° , N 48.74°) are light blue and magenta in **Figure 5.29**, which indicates that the retrieved STDs from both stations do not agree well with their model equivalents. After checking the stacking maps of the two stations, significant multipath effects could be observed (**Figure 5.30**). At low elevations the station HOMM has a positive multipath effect, while the station SAL2 has a negative multipath effect. However for most stations the differences for assumed SF and observed DF data are not significant, i.e., STDs for both processing options show similar characteristics relative to their model equivalents for individual stations.

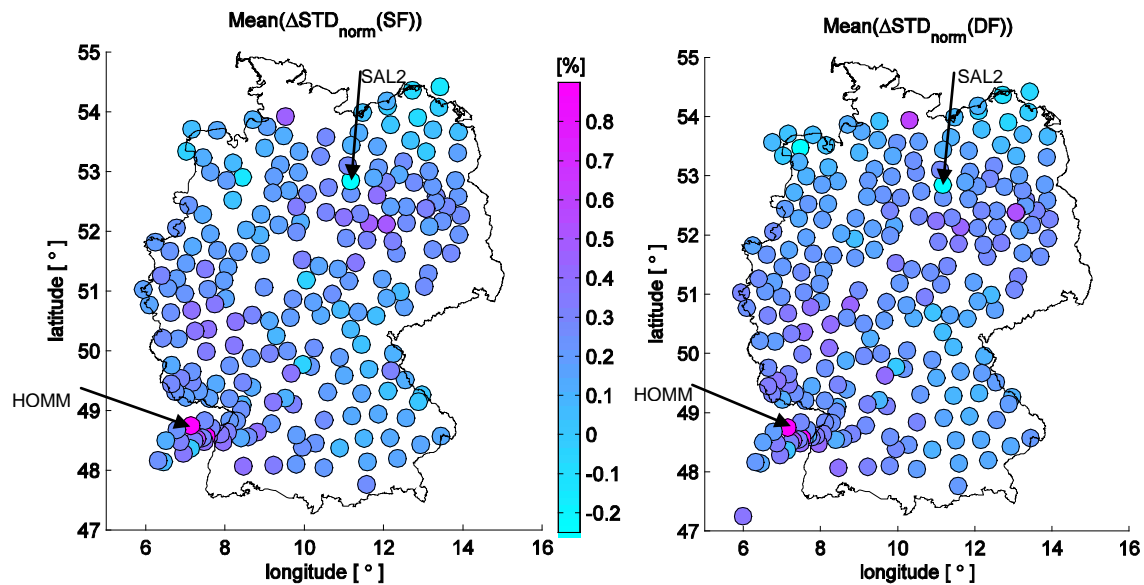


Figure 5.29: The relative bias between GPS retrieved STDs (using SF and DF data) and STDs derived from the ECMWF analysis for each station. The left (right) panel corresponds to SF (DF) comparison for DOY 220–230 in 2007.

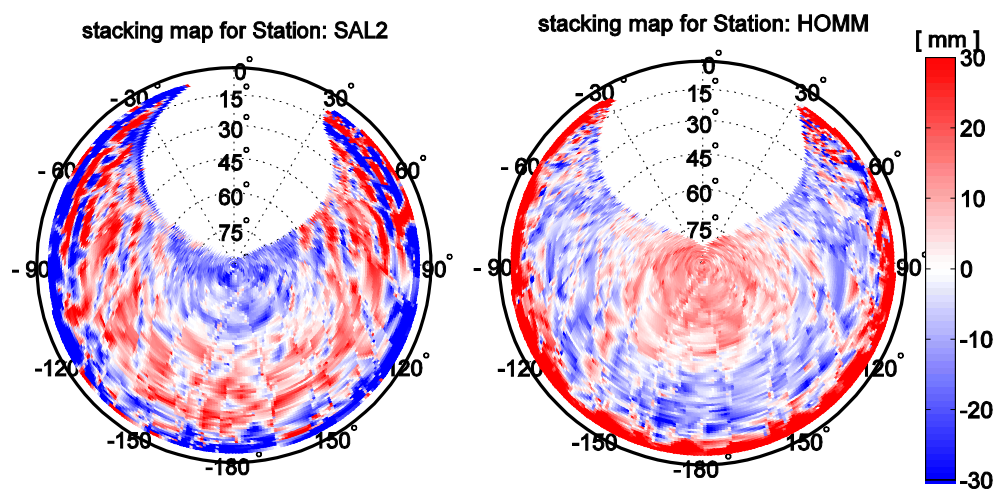


Figure 5.30: The stacking maps for two stations SAL2 and HOMM for DOY 220–230 in 2007, both show severe multipath effects at low elevations.

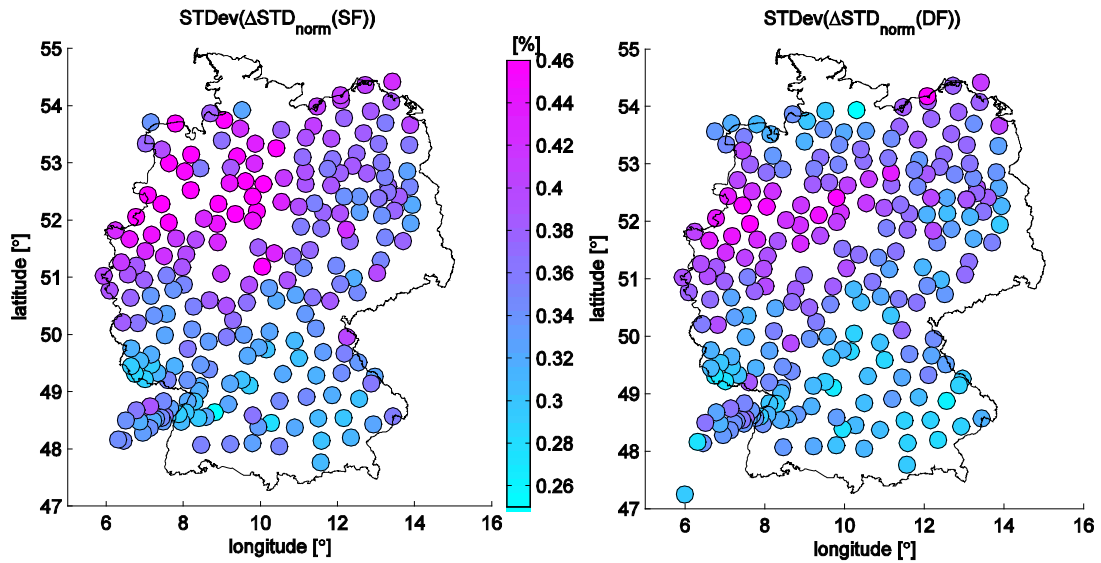


Figure 5.31: The relative standard deviation between GPS retrieved STDs (using SF and DF data) and STDs derived from the ECMWF analysis for each station. The left (right) panel corresponds to SF (DF) comparison for DOY 220–230 in 2007.

5.2.3 Slant integrated water vapor from GPS and water vapor radiometers

Water Vapor Radiometers (WVR) can provide highly accurate observations of the integrated water vapor (SWV) along any given line of sight. These observations can be used to validate GPS STDs after separating the dry and wet contribution to the STD. The method described in Chapter 2 was applied to both STD data sets to derive SWV data suitable for GPS-WVR comparisons. In zenith direction the SWV is almost identical to the IWV and varies usually between 5 and 50 $\text{kg}\cdot\text{m}^{-2}$ at mid-latitudes. In many validation studies (Braun et al., 2003; Ware et al., 1997) the IWV error was estimated to $\sim 1.3 \text{ kg}\cdot\text{m}^{-2}$ which is almost constant and independent of the total amount of water vapor in the atmosphere. Therefore, the relative error is rather large at dry days ($> 20\%$) and decreases considerably for very wet situations ($< 2\%$). As in case of the STD the SWV increases considerably with decreasing elevations.

The radiometer observations available for this study were taken within the framework of the COPS which took place in 2007 in Southwestern Germany / Eastern France. The hemisphere-scanning Humidity and Temperature Profiler HATPRO (Rose et al., 2005) of the University of Cologne was deployed on the roof of the US Atmospheric Radiation Measurement Program (ARM) Mobile Facility (AMF) in the Murg Valley, which is located in the Northeastern part of the Black Forest, Germany (48.32°N , 8.23°E , 511 m above sea level). The site was located in the north-south oriented Murg Valley which is roughly 1 km wide. The WVR was placed 2 meter higher than the antenna of a collocated GPS station GFZ0. The WVR operated in full hemisphere scan mode between October and December 2007.

The HATPRO is a 14-channel microwave radiometer observing atmospheric emission in two bands using seven channels between 22.235 and 31.4 GHz along the wing of the 22.235 GHz rotational water vapor line to derive the SWV via multi-linear regression

yielding accuracies better than $0.7 \text{ kg}\cdot\text{m}^{-2}$. The WVR observed at 36 azimuth angles every 10° , and at 8 elevation angles ranging from 14.4° to 90° leading to a total number of 288 observations per scan cycle distributed over the whole hemisphere. The elevations below 14.4° are not taken into account to avoid environmental influences. A whole hemisphere scan requires approximately 11 minutes. Since only a few WVR observations were performed exactly at the same time and in the same direction as the GPS observations, the SWVs were interpolated from the closest three WVR scans to the direction of the GPS observation. Using a linear interpolation the WVR-SWV values as well as tracking times was interpolated on the GPS observations.

In the Black Forest region the atmosphere between October and December 2007 was relatively dry with the zenith IWVs varying from 10 to $20 \text{ kg}\cdot\text{m}^{-2}$. At DOY 283 (Oct. 10, 2007) the IWV decreased from $17 \text{ kg}\cdot\text{m}^{-2}$ in the morning down to $10 \text{ kg}\cdot\text{m}^{-2}$ at midnight, and changed more intensely than the observed IWV at most other days. Assuming an IWV error of $1 \text{ kg}\cdot\text{m}^{-2}$ the relative IWV error at this day should be between 6 and 10 %. For this day the SWVs derived from GPS STDs and the WVR were validated. In total 4349 (4168) SWVs from DF (SF) receivers were available and the WVR observations could be successfully interpolated for 3104 (3167) of these observations. As in the previous studies the absolute

$$\Delta SWV = SWV_{WVR} - SWV_{GPS}, \quad (5.5)$$

and relative differences were investigated:

$$\Delta SWV_{rel} = \frac{\Delta SWV}{SWV_{WVR}}. \quad (5.6)$$

The absolute differences computed from all observations and all elevations show a very small bias of $0.2 \text{ kg}\cdot\text{m}^{-2}$ (DF) and $0.5 \text{ kg}\cdot\text{m}^{-2}$ (SF). The standard deviations of $1.7 \text{ kg}\cdot\text{m}^{-2} = 6.8 \%$ (DF) and $1.6 \text{ kg}\cdot\text{m}^{-2} = 6.1 \%$ (SF) provide no indication that the GPS SWV error should be much larger than the IWV error. The elevation-dependent differences (**Figure 5.32** and **Figure 5.33**) show a comparable agreement between GPS and WVR; for both cases and all elevations the bias is well below $1 \text{ kg}\cdot\text{m}^{-2}$ or 5 %. The standard deviation increases almost linearly from $1.3 \text{ kg}\cdot\text{m}^{-2}$ near the zenith to about $\sigma = 2 \text{ kg}\cdot\text{m}^{-2}$ at an elevation of 20° . The relative differences decreases from 6 to 5 %. Even if the GPS-WVR differences were caused by the GPS SWV error alone this would be below the estimated IWV error. The elevation-dependent statistical quantities were computed using a running window with 100 observations. The increasing bias at elevations below $\sim 30^\circ$ is most presumably caused by the WVR data interpolation. As the radiometer is located down in the Murg Valley some mountains block the view in certain directions and only a limited number of observations can be interpolated to the GPS satellite direction. The most important result of this study is that there is no significant difference between the retrieved tropospheric products from DF and assumed SF data. The ΔSWV_{SF} data are even slightly smaller than the DF differences.

This good result is very encouraging as several approximations had to be made on the GPS side to estimate the SWV: The SHD had to be estimated from the surface pressure at the GPS station to obtain the SWD and the surface temperature was required to estimate the conversion factor Π (Eq. (2.22)), which finally leads to the SWV. In case of the SF data the ionosphere correction is an additional potential uncertainty. Furthermore, the WVR did not point to the GPS satellites and the hemisphere scans had to be interpolated in order to get a sufficiently large WVR data set.

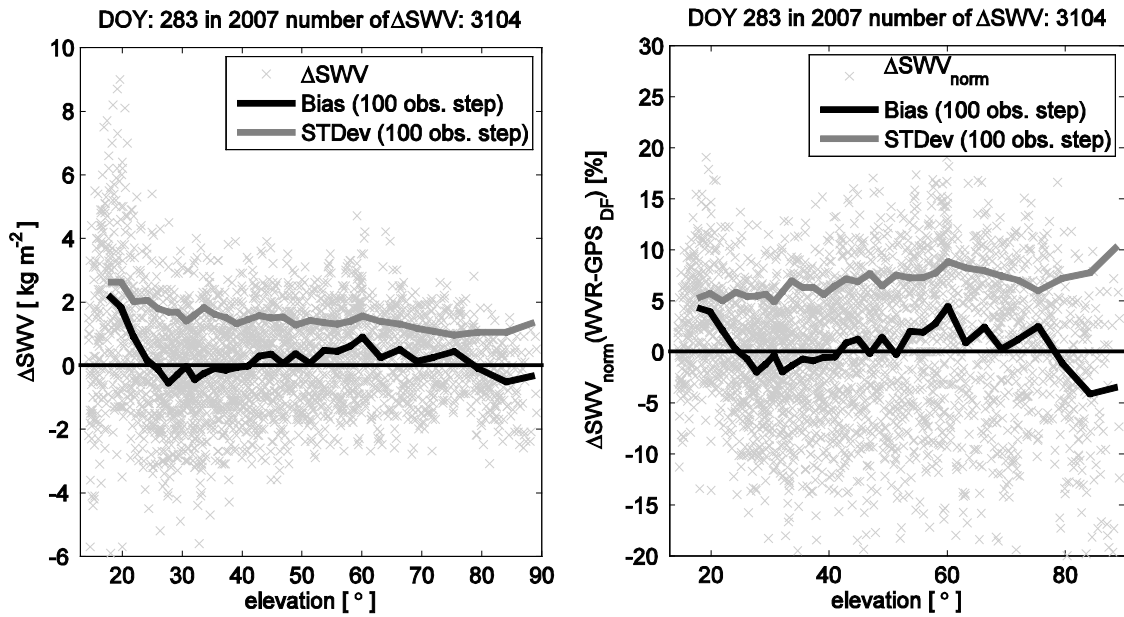


Figure 5.32: Left panel: The bias and the standard deviation between GPS DF retrieved SWVs and SWVs obtained from a WVR versus the elevation angle. Right panel: The relative bias and standard deviation between GPS DF retrieved SWVs and SWVs obtained from a WVR versus the elevation angle.

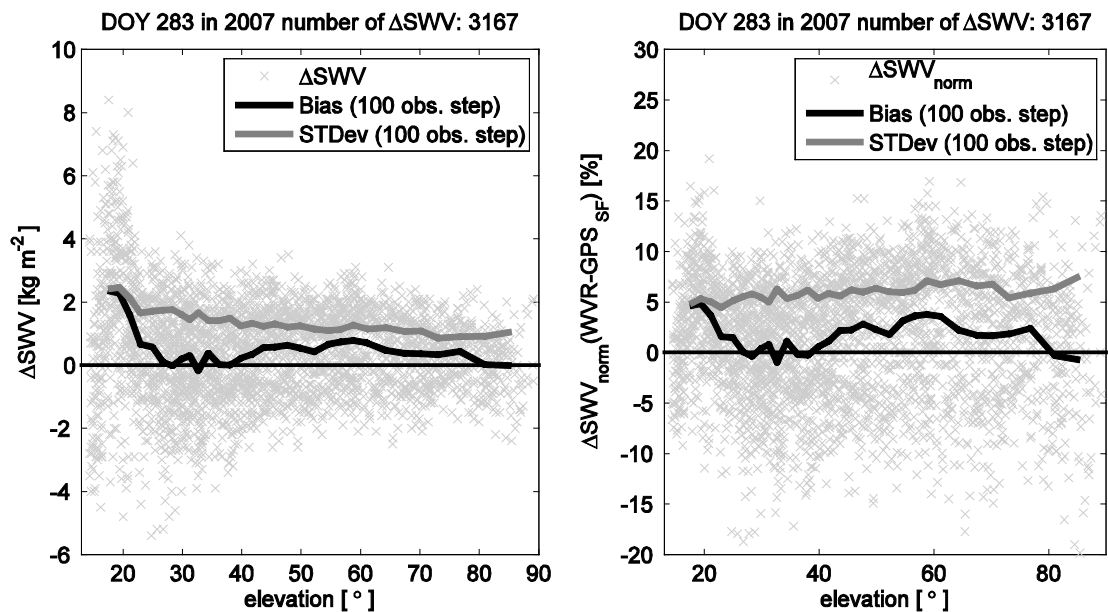


Figure 5.33: Left panel: The bias and the standard deviation between GPS SF retrieved SWVs and SWVs obtained from a WVR versus the elevation angle. Right panel: The relative bias and standard deviation between GPS SF retrieved SWVs and SWVs obtained from a WVR versus the elevation angle.

Validation summary

In order to estimate the potential of the existing DF network densification with SF receivers three different validation studies have been carried out. Each of them provides information of a different type. Analyzing the SF and DF GPS data sets provides mainly information on the ionosphere correction. ZTD and STD data could easily be compared

and the quality of single stations could be observed as well as the network performance. This is also true for the validation with a numerical weather model. The model STDs could be estimated for a large number of stations but only at ECMWF analysis times, i. e., every 6 hours. In contrast to the first study the STD difference represents the observation errors of the GPS and model data and not only some differences in the processing strategy. In case of the radiometer validation the data of only one GPS station near the radiometer and only for one day could be analyzed. However, the radiometer was taking data continuously and provides observations with high-quality. As the radiometer provides the SWV instead of STDs the GPS STDs had to be converted to the SWV and additional errors were introduced. The results from the previous paragraphs are summarized in **Table 5.4**. To provide comparable quantities STD differences are obtained by multiplying fractional STD differences with a nominal ZTD value of 2.5 m. The SWD differences are obtained by multiplying SWV differences with the inverse conversion factor $\Pi^{-1} = 6.45$ (see Eq. (2.21)).

Validation	No. Stations	No. Data	μ [mm]	σ [mm]	RMS [mm]
ZTD _(SF-DF)	258	$2.4 \cdot 10^5$	0.1	2.9	2.9
STD _(SF-DF)	258	$1.0 \cdot 10^7$	0.3	4.5	4.5
STD _(ECMWF-DF)	239	$7.9 \cdot 10^6$	5.2	13.0	14.0
STD _(ECMWF-SF)	232	$7.4 \cdot 10^6$	5.2	13.7	14.7
SWD _(WVR-DF)	1	$3.104 \cdot 10^3$	1.3	11.0	11.1
SWD _(WVR-SF)	1	$3.167 \cdot 10^3$	3.2	10.3	10.8

Table 5.4: Summarizing the bias μ , the standard deviation σ , and the RMS for ZTD, STD and SWV comparisons for DOY 220–230 in 2007.

6 Conclusions and outlook

GPS observations are widely used in meteorological applications because of their high sensitivity to atmospheric humidity. As a very promising technology the ground-based GPS meteorology can improve the performance of numerical weather prediction significantly. In Germany, a GPS network with an inter-station spacing of about 50 km is used to retrieve the ZTDs with an accuracy of 6 to 13 mm. The ZTD products are generated every hour with a delay of only 40 minutes. In Europe several meteorological institutes assimilate the ZTDs operationally for numerical weather prediction.

However, due to the high spatiotemporal variability of water vapor ZTDs of higher spatial resolution are required especially for regional and short-term forecasts. Consequently, the existing GPS network must be densified, ideally aiming at an inter-station distance below 20 km. Currently, only DF GPS receivers are used for atmospheric remote sensing. To reduce the cost of the densification SF receivers can be applied, which are significantly less expensive than DF receivers. To eliminate the ionospheric delay of the SF data, a new correction method, called SEID (Satellite specific Epoch-differenced Ionospheric Delay) was developed in this thesis. In the SEID model, for each satellite at each epoch the parameters of a linear model for the spatial change of the epoch-differenced ionospheric delay are estimated using observations from the nearby reference stations equipped with DF receivers. With the estimated ionospheric model, SF data is converted to DF data, which can be processed by any existing GPS software without any modification. This may speed up the densification of existing ground GPS networks with SF receivers for retrieving tropospheric information of higher spatial resolution. The limitation of the SEID model is that the ambiguities of the converted \tilde{L}_2 observations cannot be fixed to an integer number, because of the unknown ionospheric delay at the first observation epoch of a satellite track. Another limitation is, that under rapid ionospheric variations, e.g., MSTID the ionospheric correction cannot be modeled precisely with a plane or low-order surface, cause an error up to 3 cm in the converted \tilde{L}_2 observations.

The SEID model was validated with data from the dense GPS network of the LUAMI campaign, which consisted of 13 SF GPS stations and 4 DF receivers. The ionospheric corrections were generated from 5 surrounding SAPOS stations within a radius of about 50 km around the SF stations. The SF GPS data were converted to DF data using the SEID model. Together with the DF stations the data of 60 days were processed using GFZ EPOS software in PPP mode. Compared to a DF station within a distance of 100 meters the agreement of ZTDs from 2 SF stations is better than 3 mm in RMS. The repeatability of the SF station coordinates is comparable to that of the DF stations. Tomographic reconstructions carried out with combined STD data from the LUAMI GPS network were compared to COSMO analyses and to radiosonde profiles, and were in general consistent. Regarding the GPS tomography the information provided by STDs of the SF receivers is of the same quality as those from DF receivers. The numerical weather model will benefit from tropospheric products from SF data.

In addition, the GPS data of about 2.5 years from a SF station was analyzed together with a collocated DF IGS station. The ZTDs and STDs retrieved from the SF station were compared with those from the DF station. The comparison showed that the accuracy of the ZTD products of the SF station is about 2.8 mm, which is almost

constant over the 2.5 years. The STDs has a bias and a standard deviation of 0.1 mm and 3.6 mm close to zenith, which increase to 0.4 mm and 21 mm at an elevation of 7°

A study was carried out to estimate the potential of future large networks of SF receivers embedded in DF receiver networks. The focus was on GPS atmosphere sounding but the results are also relevant for other applications. The SEID method which utilizes the L_2 signals of nearby DF receivers was applied to a network of more than 270 DF receivers. For simulating SF stations each station in turn was regarded as a SF station by replacing the observed L_2 signal with the \tilde{L}_2 signal provided by SEID. It turned out that this method can be applied to almost all stations within the network. A good quality of the \tilde{L}_2 signals was found for most stations except some stations near the network boundaries and near some stations with known quality issues.

The ZTD and STD observations obtained from the assumed SF data were compared to the corresponding DF data and to independent observations from a numerical weather model and a water vapor radiometer. The results of all three validation studies show that the ZTD and STD observations obtained from SF receivers are almost of the same quality as the DF observations. Comparing the DF data with the assumed SF data it could be shown that the \tilde{L}_2 signal estimated by SEID leads only to a small additional error of about 3 mm. The quality of the SF data is fully sufficient for atmosphere sounding and the advantage of having more observations with improved spatial resolution is much higher than the drawback of the slightly increased noise.

In the simulation study some problems that can potentially appear with real SF receivers could not be addressed. Increased receiver noise and multipath effects will reduce the quality of SF data and geodetic-grade SF receivers should be preferred. On the other hand the ionospheric corrections can be expected to become better if the SF receivers are placed between the existing DF receivers, thereby decreasing the distances between SF and DF stations.

In a next step, campaigns with an increasing number of SF receivers will be conducted to show the applicability of the SEID method in different surroundings and to validate the quality of the SF products with more independent observations. Future studies with a larger network and a more homogeneous receiver distribution are recommended. The impact of SF data will be estimated by assimilating such observations to numerical weather models and by reconstructing spatially resolved humidity fields using the GPS tomography.

References

- Alber, C., Ware, R., Rocken, C. and Braun, J. (2000), 'Obtaining single path delays from GPS double differences', *Geophys. Res. Lett.* **27**(7), 2661–2664.
- Pulkkinen, A., Lindahl, S., Viljanen, A. and Pirjola, R. (2005), 'Geomagnetic storm of 29-31 October 2003: Geomagnetically induced currents and their relation to problems in the Swedish high-voltage power transmission system', *Space Weather* **3**, S08C03.
- Arras, C. (2010), A global survey of sporadic e layers based on GPS radio occultations by CHAMP, GRACE and FORMOSAT-3 / COSMIC, PhD thesis, Deutsches GeoForschungsZentrum GFZ, Germany.
- Bender, M., Dick, G., Ge, M., Deng, Z., Wickert, J., Kahle, H.-G., Raabe, A. and Tetzlaff, G. (2010), 'Development of a GNSS water vapor tomography system using algebraic reconstruction techniques', *Adv. Space Res.* **47**(10), 1704 – 1720.
- Bender, M., Dick, G., Wickert, J., Ramatschi, M., Ge, M., Gendt, G., Rothacher, M., Raabe, A. and Tetzlaff, G. (2009), 'Estimates of the information provided by GPS slant data observed in Germany regarding tomographic applications', *J. Geophys. Res.* **114**, D06303.
- Bern, T. (2008), Single frequency, single-receiver terrestrial spaceborne point positioning, PhD thesis, Department of Geodesy and Geomatics Engineering, University of New Brunswick.
- Bevis, M., Businger, S., Chiswell, S., Herring, T. A., Anthes, R. A., Rocken, C. and Ware, R. H. (1994), 'GPS meteorology: Mapping Zenith Wet Delays onto Precipitable Water', *J. Appl. Meteor.* **33**(3), 379–386.
- Bevis, M., Businger, S., Herring, T. A., Rocken, C., Anthes, R. A. and Ware, R. H. (1992), 'GPS meteorology: Remote sensing of atmospheric water vapor using the global positioning system', *J. Geophys. Res.* **97**(D14), 15787–15801.
- Blewitt, G. (1989), 'Carrier Phase Ambiguity Resolution for the Global Positioning System Applied to Geodetic Baselines up to 2000 km', *Geophys. Res. Lett.* **94**(b8), 10,187–10,203.
- Blewitt, G. (1990), 'An automatic editing algorithm for GPS data', *Geophys. Res. Lett.* **17**(3), 199–202.
- Boehm, J., Niell, A., Tregoning, P. and Schuh, H. (2006), 'Global Mapping Function (GMF): A new empirical mapping function based on numerical weather model data', *Geophys. Res. Lett.* **33**, L07304.
- Braschak, M., Brown, H., Jr., Carberry, J., Grant, T., Hatten, G., Patocka, R. and Watts, E. (2010), 'GPS IIF Satellite Overview', *Proceedings of the 23rd International Technical Meeting of The Satellite Division of the Institute of Navigation (ION GNSS 2010)* pp. 753–770.
- Braun, J. J. (2004), Remote Sensing of Atmospheric Water Vapor with the Global Positioning System, PhD thesis, University of Colorado, Department of Aerospace Engineering Sciences.

- Braun, J., Rocken, C. and Liljegren, J. (2003), 'Comparisons of line-of-sight water vapor observations using the global positioning system and a pointing microwave radiometer', *J. Atmos. Oceanic Technol.* **20**(5), 606–612.
- Braun, J., Rocken, C., Meertens, C. and Ware, R. (1999), Development of a water vapor tomography system using low cost L1 GPS receivers, Ninth Annual ARM Science Team Meeting Proceedings, San Antonio, Texas, U.S.
- Braun, J., Rocken, C. and Ware, R. (2001), 'Validation of line-of-sight water vapor measurements with GPS', *Radio Sci.* **36**(3), 459–472.
- Brunner, F. K. and Gu, M. (1991), 'An improved model for the dual frequency ionospheric correction of GPS observations', *Manuscripta Geodaetica* **16**, 205–214.
- Cess, R. D. (2005), 'Water vapor feedback in climate models', *Science* **310**(5749), 795–796.
- Dach, R., Hugentobler, U., Fridez, P. and Meindl, M. (2005), Bernese GPS software version 5.0, Technical report, Astronomical Institute, Berne University, Switzerland.
- Davies, K. (1990), *Ionospheric radio*, IEE electromagnetic waves series, Peregrinus on behalf of the Institution of Electrical Engineers.
- Davis, J., Herring, T., Shapiro, I., Rogers, A. and Elgered, G. (1985), 'Geodesy by radio interferometry: Effects of atmospheric modeling errors on estimates of baseline length', *Radio Sci.* **20**(6), 1593–1607.
- Deng, Z. (2008), Preprocessing of high rate GPS data for real-time applications, masters thesis, Universität Stuttgart, Geodätisches Institut. <http://elib.uni-stuttgart.de/opus/volltexte/2008/3559/>
- Deng, Z., Bender, M., Dick, G., Ge, M., Wickert, J., Ramatschi, M. and Zou, X. (2009), 'Retrieving tropospheric delays from GPS networks densified with single frequency receivers', *Geophys. Res. Lett.* **36**, L19802.
- Deng, Z., Bender, M., Zusc, F., Ge, M., Dick, G., Ramatschi, M., Wickert, J., Löhnert, U. and Schön, S. (2011), 'Validation of tropospheric slant path delays derived from single and dual frequency GPS receivers', *Radio Sci.* **46**, RS6007.
- Dick, G., Gendt, G. and Reigber, C. (2000), Operational water vapor estimation in a dense german network, in K. Gowey, R. Neilan and A. Moore, eds, '1999 Technical Reports', IGS Central Bureau, Jet Propulsion Laboratory, Pasadena, pp. 375–384.
- Eresmaa, R., Healy, S., Järvinen, H. and Salonen, K. (2008), 'Implementation of a ray-tracing operator for ground-based GPS slant delay observation modeling', *J. Geophys. Res.* **113**, D11114.
- Fuhrmann, T., Knöpfler, A., Luo, X. and Maye, M. (2010), Zum Stacking von Phasenresiduen aus GNSS-Auswertungen mittels Precise Point Positioning, in K. Zippelt, ed., 'Vernetzt und ausgeglichen : Festschrift zur Verabschiedung von Prof. Dr.-Ing. habil. Dr.-Ing. e.h. Günter Schmitt.', Schriftenreihe des Studiengangs Geodäsie und Geoinformatik / Karlsruher Institut für Technologie, Studiengang Geodäsie und Geoinformatik ; 2010,3.
- Gendt, G., Dick, G., Reigber, C., Tomassini, M., Liu, Y. and Ramatschi, M. (2004), 'Near real time GPS water vapor monitoring for numerical weather prediction in Germany', *J. Meteor. Soc. Japan* **82**(1B), 361–370.
- Gendt, G., Dick, G. and Söhne, W. (1999), GFZ analysis center of IGS – annual report 1998, in K. Gowey, R. Neilan and A. Moore, eds, '1998 Technical Reports',

- Pasadena, pp. 79–87.
- Gendt, G., Reigber, C. and Dick, G. (2001), ‘Near real-time water vapor estimation in a German GPS network - first results from the ground program of the HGF GASP project’, *Phys. Chem. Earth (A)* **26**(6-8), 413–416.
- Geng, J., Teferle, F. N., Meng, X. and Dodson, A. H. (2010), ‘Towards PPP-RTK: Ambiguity resolution in real-time precise point positioning’, *Adv. Space Res.* **47**(10), 1664–1673.
- Geng, J., Teferle, F., Shi, C., Meng, X., Dodson, A. and Liu, J. (2009), ‘Ambiguity resolution in precise point positioning with hourly data’, *GPS Solutions* **13**, 263–270.
- Glabsch, J., Heunecke, O. and Schuhbäck, S. (2009), ‘Monitoring the Hornbergl landslide using a recently developed low cost GNSS sensor network’, *Journal of Applied Geodesy* **3**(3), 179–192.
- Gregorius, T. L. H. and Blewitt, G. (1998), ‘The effect of weather fronts on GPS measurements’, *GPS World* **9**, 52–60.
- Gutman, S. I., Sahn, S., Benjamin, S. G., Schwartz, B. E., Holub, K., Stewart, J. Q. and Smith, T. L. (2004), ‘Rapid retrieval and assimilation of ground based GPS precipitable water observations at the NOAA forecast systems laboratory: Impact on weather forecasts’, *J. Meteor. Soc. Japan* **82**(1B), 351–360.
- Haase, J., Ge, M., Vedel, H. and Calais, E. (2003), ‘Accuracy and variability of GPS tropospheric delay measurements of water vapor in the western mediterranean’, *J. Appl. Meteor.* **42**(11), 1547–1568.
- Han, S. (1997), Carrier Phase-Based Long-Range GPS Kinematic Positioning, PhD thesis, The University of New South Wales, Sydney, Australia.
- Héroux, P. and Kouba, J. (2001), ‘GPS precise point positioning using IGS orbit products’, *Phys. Chem. Earth (A)* **26**(6-8), 573–578.
- Hidore, J. (1972), *A geography of the atmosphere*, Brown foundations of geography series, W. C. Brown Co.
- Hocke, K. and Schlegel, K. (1996), ‘A review of atmospheric gravity waves and travelling ionospheric disturbances: 1982-1995’, *Ann. Geophys.* (9), 917–940.
- Hofmann-Wellenhof, B., Lichtenegger, H. and Collins, J. (2001), *GPS: Theory and Practice*, Springer Press.
- ICD (2000), Interface Control Document - Navstar GPS space segment / navigation user interfaces, ICD-GPS-200C., Technical report.
- Janssen, V. and Rizos, C. (2002), ‘A mixed-mode GPS network processing approach for deformation monitoring applications’, *Survey Review* **37**, 2–19.
- Janssen, V. and Rizos, C. (2005), Mixed-mode GPS deformation monitoring - a cost-effective and accurate alternative?, in F. Sansó and F. Sansó, eds, ‘A Window on the Future of Geodesy’, Vol. 128 of *International Association of Geodesy Symposia*, Springer Berlin Heidelberg, pp. 533–537. 10.1007/3-540-27432-4_90.
- Järvinen, H., Eresmaa, R., Vedel, H., Salonen, K., Niemelä, S. and de Vries, J. (2007), ‘A variational data assimilation system for ground-based GPS slant delays’, *Q. J. R. Meteorol. Soc.* **133**, 969–980.
- Kedar, S., Hajj, G. A., Wilson, B. D. and Heflin, M. B. (2003), ‘The effect of the second

- order GPS ionospheric correction on receiver positions', *Geophys. Res. Lett.* **30**, 1829.
- Khattatov, B., Murphy, M., Gnedin, M., Cruickshank, B., Boisvert, J., Sheffel, J., Jayaraman, V. and Fuller-Rowell, T. (2004), 'An ionospheric forecasting system', *Proceedings of the 17th International Technical Meeting of the Satellite Division of The Institute of Navigation (ION GNSS 2004)* pp. 408–419.
- King, R. (2003), Documentation for the GAMIT GPS software analysis, release 10.1, Technical report, Scripps Institution of Oceanography.
- Klobuchar, J. A. (1987), 'Ionospheric time-delay algorithm for single frequency GPS users', *IEEE Transactions on Aerospace and Electronic Systems* **AES-23**(3), 325–331.
- Koch, K.-R. (2004), *Parameterschätzung und Hypothesentests in linearen Modellen*, Ehemals Ferd. Dümmlers Verlag, Bonn.
- Kouba, J. (2009), 'Testing of global pressure/temperature (GPT) model and global mapping function (GMF) in GPS analyses', *J. Geodesy* **83**(3-4), 199–208.
- Kursinski, E. R. and Hajj, G. A. (2001), 'A comparison of water vapor derived from GPS occultations and global weather analyses', *J. Geophys. Res.* **106**(D1), 1113–1138.
- Kursinski, E. R., Hajj, G. A., Bertiger, W. I., Leroy, S. S., Meehan, T. K., Romans, L. J., Schofield, J. T., McCleese, D. J., Melbourne, W. G., Thornton, C. L., Yunck, T. P., Eyre, J. R. and Nagatani, R. N. (1996), 'Initial results of radio occultation observations of earth's atmosphere using the global positioning system', *Science* **271**, 1107–1110.
- Kursinski, E. R., Hajj, G., Schofield, J., Linfield, R. and Hardy, K. (1997), 'Observing Earth's atmosphere with radio occultation measurements using the Global Positioning System', *J. Geophys. Res.* **102**(D19), 23429–23465.
- Landau, H., Vollath, U. and Chen, X. (2002), 'Virtual reference station systems', *Journal of Global Positioning Systems* **1**, 137–143.
- Memarzadeh, Y. (2009), Ionospheric Modeling for Precise GNSS Applications, PhD thesis, Technische Universiteit Delft, Netherlands.
- Mendes, V. B. (1999), Modeling the neutral-atmosphere propagation delay in radiometric space techniques, PhD thesis, University of New Brunswick, Fredericton, New Brunswick, Canada, Department of Geodesy and Geomatics Engineering. Technical Report No. 199.
- Mervart, L., Lukes, Z., Rocken, C. and Iwabuchi, T. (2008), 'Precise Point Positioning with Ambiguity Resolution in Real-time', *Proceedings of the 21th International Technical Meeting of the Satellite Division of The Institute of Navigation (ION GNSS 2008)* pp. 397–405.
- Niell, A. E. (1996), 'Global mapping functions for the atmosphere delay at radio wavelengths', *J. Geophys. Res.* **101**(B2), 3227–3246.
- Odiijk, D. (2002), Fast precise GPS positioning in the presence of ionospheric delays, PhD thesis, Faculty of Civil Engineering and Geosciences, Delft University of Technology, NL.
- Pacione, R., Sciarretta, C., Faccani, C., Ferretti, R. and Vespe, F. (2001), 'GPS PW assimilation into MM5 with the nudging technique', *Phys. Chem. Earth (A)* **26**(6-

8), 481–485.

- Pany, T., Pesec, P. and Stangl, G. (2001), 'Atmospheric GPS slant path delays and ray tracing through numerical weather models, a comparison', *Phys. Chem. Earth (A)* **26**(3), 183–188. DOI: 10.1016/S1464-1895(01)00044-8.
- Rizos, C., Han, S., Ge, L., Chen, H., Hatanaka, Y. and Abe, K. (2000), 'Low-cost densification of permanent GPS networks for natural hazard mitigation: First tests on GSI's Geonet network', *Earth, Planets & Space* **52**, 867–871.
- Rocken, C., Johnson, M. and Braun, J. (2000), 'Improving GPS surveying with modeled ionospheric corrections', *Geophys. Res. Lett.* **27**(23), 3821–3824.
- Rocken, C., Kuo, Y., Schreiner, W. S., Hunt, D., Sokolovski, S. and McCormick, C. (2000), 'COSMIC system description', *Terr. Atmos. Oceanic Sci.* **11**(1), 21–52.
- Rocken, C., Ware, R. H., Hove, T. V., Solheim, F., Alber, C., Johnson, J., Bevis, M. and Businger, S. (1993), 'Sensing Atmospheric Water Vapor with the Global Positioning System', *Geophys. Res. Lett.* **20**(23), 2631–2634.
- Rose, T., Crewell, S., Löhnert, U. and Simmer, C. (2005), 'A network suitable microwave radiometer for operational monitoring of the cloudy atmosphere', *Atmos. Res.* **75**, 183–200.
- Saastamoinen, J. (1972), 'Atmospheric correction for the troposphere and stratosphere in radio ranging of satellites', *The use of artificial satellites for geodesy, Geophys. Monogr.* **15**, 247–251.
- Schaer, S. (1999), Mapping and Predicting the Earth's Ionosphere using the GPS, PhD thesis, Univ. Berne Switzerland.
- Schmid, R., Steigenberger, P., Gendt, G., Ge, M. and Rothacher, M. (2007), 'Generation of a consistent absolute phase-center correction model for GPS receiver and satellite antennas', *Journal of Geodesy* **81**(12), 781–798.
- Seeber, G. (2003), *Satellite geodesy*, Walter de Gruyter.
- Seidel, D. J. (2002), *Water Vapor: Distribution and Trends*, Vol. 1, John Wiley & Sons.
- Sekido, M., Kondo, T., Kawai, E. and Imae, M. (2003), 'Evaluation of GPS-based ionospheric TEC map by comparing with VLBI data', *Radio Sci* **38**, 1069, 22.
- Teunissen, P. J. G. and Kleusberg, A., eds (1998), *GPS for Geodesy*, 2. edn, Springer.
- Tsugawa, T., Otsuka, Y., Coster, A. J. and Saito, A. (2007), 'Medium-scale traveling ionospheric disturbances detected with dense and wide TEC maps over North America', *Geophys. Res. Lett.* **34**(22), L22101.
- Wanninger, L. (1995), 'Enhancing differential GPS using regional ionospheric error models', *Bull. Geod.* **69**, 283–291.
- Wanninger, L. (2006), 'Introduction to Network RTK'. <http://www.wasoft.de/e/iagwg451/intro/introduction.html>
- Ware, R., Alber, C., Rocken, C. and Solheim, F. (1997), 'Sensing integrated water vapor along GPS ray paths', *Geophys. Res. Lett.* **24**(4), 417–420. doi: 10.1029/97GL00080.
- Ware, R., Rocken, C., Solheim, F., Exner, M., Schreiner, W., Anthes, R., Feng, D., Herman, B., Gorbunov, M., Sokolovskiy, S., Hardy, K., Kuo, Y., Zou, X., Trenberth, K., Meehan, T., Melbourne, W. and Businger, S. (1996), 'GPS Sounding of the

- Atmosphere from Low Earth Orbit: Preliminary result', *Bull. Amer. Meteor. Soc.* **77**(1), 19–40.
- Wickert, J. (2002), Das CHAMP-Radiokkultationsexperiment: Algorithmen, Prozessierungssystem und erste Ergebnisse, PhD thesis, Karl-Franzens-Universität, Graz.
- Wickert, J., Reigber, C., Beyerle, G., König, R., Marquardt, C., Schmidt, T., Grunwaldt, L., Galas, R., Meehan, T. K., Melbourne, W. G. and Hocke, K. (2001), 'Atmosphere sounding by GPS radio occultation: First results from CHAMP', *Geophys. Res. Lett.* **28**, 3263–3266.
- Wu, J. T., Wu, S. C., Hajj, G. A., Bertiger, W. I. and Lichten, S. M. (1993), 'Effects of antenna orientation on GPS carrier phase', *Manuscripta Geodaetica* **18**, 91–98.
- Wübbena, G., Bagge, A. and Schmitz, M. (2001), 'RTK Networks based on Geo++ GNSMART - Concepts, Implementation, Results', *Proceedings of the 14th International Technical Meeting of the Satellite Division of The Institute of Navigation (ION GPS 2001)* pp. 368–378.
- Wübbena, G., Schmitz, M. and Bagge, A. (2005), 'PPP-RTK: precise point positioning using state-space representation in RTK networks', *Proceedings of the 18th International Technical Meeting of the Satellite Division of The Institute of Navigation (ION GPS 2005)* pp. 2584–2594.
- Wübbena, G., Schmitz, M., Menge, F., Böder, V. and Seeber, G. (2000), 'RTK Networks based on Geo++ GNSMART - Concepts, Implementation, Results', *Proceedings of the 14th International Technical Meeting of the Satellite Division of The Institute of Navigation (ION GPS 2000)* pp. 2512 – 2522.
- Wulfmeyer, V., Behrendt, A., Bauer, H.-S., Kottmeier, C., Corsmeier, U., Blyth, A., Craig, G., Schumann, U., Hagen, M., Crewell, S., Girolamo, P. D., Flamant, C., Miller, M., Montani, A., Mobbs, S., Richard, E., Rotach, M., Arpagaus, M., Russchenberg, H., Schlüssel, P., König, M., Gätner, V., Steinacker, R., Dorninger, M., Turner, D., Weckwerth, T., Hense, A. and Simmer, C. (2008), 'The convective and orographically-induced precipitation study: A research and development project of the World Weather Research program for improving quantitative precipitation forecasting in low-mountain regions', *Bull. Amer. Meteor. Soc.* **89**(10), 1477–1486.
- Yan, X., Ducrocq, V., Poli, P., Hakam, M., Jaubert, G. and Walpersdorf, A. (2009), 'Impact of GPS zenith delay assimilation on convective-scale prediction of Mediterranean heavy rainfall', *J. Geophys. Res.* **114**, D03104.
- Zou, X., Deng, Z., Ge, M., Dick, G., Jiang, W. and Liu, J. (2010), 'GPS data processing of networks with mixed single- and dual-frequency receivers for deformation monitoring', *Adv. Space Res.* **46**(2), 130 – 135.
- Zumberge, J. F., Heflin, M. B., Jefferson, D. C., Watkins, M. M. and Webb, F. H. (1997), 'Precise point positioning for the efficient and robust analysis of GPS data from large networks', *J. Geophys. Res.* **102**(B3), 5005–5018.
- Zus, F., Grzeschik, M., Bauer, H.-S., Wulfmeyer, V., Dick, G. and Bender, M. (2008), 'Development and optimization of the IPM MM5 GPS slant path 4DVAR system', *Meteorol. Z.* **17**(6), 867–885.

Acknowledgements

First of all I would like to express my profound respect and gratitude to Prof. Dr.-Ing, Steffen Schön, Institut für Erdmessung, Leibniz Universität Hannover, for supervising this thesis, for his continuous support, guidance and encouragement of my studies and research.

I would like to thank Dr. Jens Wickert for giving me the opportunity to work at GFZ on this challenging research topic. Thank you for continuous and extensive support throughout the last years.

Also many thanks to Dr. Maorong Ge for the time he spent on my thesis and helpful discussions. I wish to thank Dr. Michael Bender for thoughtful questions and valuable suggestions to improve this thesis, and for providing the tomography solution. I thank Dr. Galina Dick for the continuous support. I thank Dr. Florian Zus for providing me the Ray-tracing software and helpful discussions. Markus Ramatschi and Carsten Falck were responsible for the single frequency GPS station hardware. Their work was greatly appreciated. I would like to thank Dr. D. Engelbart, his colleagues from the Lindenberg Meteorological Observatory (German Weather Service) and Martin König and Roland Winter from GFZ for supporting the setup of the GPS network within the LUAMI campaign.

Thank Thomas Nischan, for unselfish sharing all the necessary knowledge and tools for the GPS data processing. Thanks to Maik Uhlemann, Xingxing Li, Maximilian Semmling, Dr.-Ing. Markus Vennebusch for all the great jobs and the exchanging of ideas in writing articles. Thank you so much for putting ideas together.

SAPOS is thanked for providing German GPS data. The organizers and participants of the COPS campaign are also thanked for kindly providing access to their radiometer and GPS data. GEO++ is thanked for providing the PCV corrections of the single frequency antenna.

The work was supported by the Deutsche Forschungsgemeinschaft, grants GE 1604/2-3 and WI 2634/7-1, within the priority programme 1167 QPV (Quantitative Precipitation Forecast). I'm thankful for the financial support during my PhD time in Potsdam.

I would like to thank my wife Yan, my brother and my parents for their continuing support.

Personal Data:

Date of Birth	1978, 7th, October
Ort of Birth	Xinjiang, China
Nationality	Chinese
Gender	male

Education:

06/2008 – 11/2012	PhD student (GNSS/GALILEO Technik) at GeoForschungsZentrum in Potsdam Germany
10/2001 - 05/2008	Diplom in Geodesy & Geoinformatics University Stuttgart, Germany
09/1997 - 09/2001	Bachelor in Surveying Engineering Tongji University, Shanghai, China
09/1994 – 09/1997	High School Changji High School No.2, Xinjiang, China

